Atmospheric Freeze Drying of Food in Fluidized Beds - Practical aspects and CFD simulation

POLITECNICO DI TORINO

SCUOLA DI DOTTORATO

PhD course in Chemical Engineering – XXVI Cycle

PhD Thesis

Atmospheric Freeze Drying of Food in Fluidized Beds

Practical aspects and CFD simulation

Mauricio Miguel COLETTO

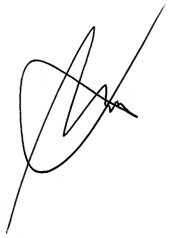

Tutors:
Antonello A. BARRESI
Daniele L. MARCHISIO

January 2015

A mi madre y a mi padre, quienenes tantas puertas me enseñaron a abrir; y a esa personita que está en camino, a quien ahora me tocará enseñarle.

Contents

Chapter 1

Introduction

Atmospheric freeze drying (AFD) is the lyophilization of a product at atmospheric pressure conditions and temperatures ranging generally between -15 and -5 °C (avoiding, thereby, ice melting). As the quality of the obtained dried products is quite similar to the quality of products dried by vacuum freeze drying (VFD), but without the need of generating vacuum, maintaining temperatures around -50 °Cin the condenser, or defrosting it, this technique is gaining a special attention by numerous investigators and the food industry.

There are several ways to carry out AFD, such as the use of a fluidized bed or a tunnel conveyor. Nevertheless, AFD involves considerably longer drying times than VFD, and the process must be modified in some way in order to shorten them without loss of product quality at the same time. One way of accomplishment of this is the fluidization of the product in a fluidized bed and removal of air moisture by means of a heat pump. However, additional energy supply is required by the heat pump compressor.

The use of an adsorbent material compatible with the food product (i.e., not toxic for human consumption), could constitute an alternative for using a heat pump or other extra energy supplies. In particular, wheat bran is an interesting material to be applied as adsorbent in this process; this adsorbent is not only compatible with foodstuff, but also, since it is a by product of the cereal processing industry, it is cheap and can be easily discarded (and reused, for example, in compost) without recovering it by means of a thermal treatment.

Nevertheless, wheat bran is a pseudo-cohesive material (i.e., it behaves like a cohesive material in fluidization, but is a Geldart B type according to its diameter and density), forming channels and preferential air paths during fluidization. In addition, when two different materials are fluidized in a fluidized bed, the mixture may undergo segregation, causing a poor contact between the adsorbent and the food particles. Thus, instead of using a traditional fluidized bed, a spout-fluid bed (jet-spouted bed, an apparatus similar to the spouted bed, with lateral air injectors

beside the main jet) may be utilized, and thereby controlling the channel formation and enhancing mixing at the same time.

On the other hand, Computational Fluid Dynamics (CFD) is a technique which, by means of numerical methods and algorithms, allows the computational simulation of fluid flow of a given physical system in a numerical grid. Various investigators have been working on the application of CFD models for simulating AFD in fluidized bed. However, in general, they simulated a single piece of foodstuff, but not the complete system with air, food material, and adsorbent (when it is applied).

Some of the main potentials of the CFD simulation are the possibility of testing new equipments without resorting large experiments, detailed analysis of the flow field and mass and heat transfer, or better description of a multi-phase system (as in the case of AFD with adsorbent). Nonetheless, conveniently refined numerical grids should be used if accurate results are wanted, beside the implementation of specific models for certain mass and heat transfer processes (like exchange between air and foodstuff particles), or the simulation of the behaviour of a pseudo-cohesive solid (as wheat bran). Moreover, the computational times for the simulation of a two-phase system in an enough refined grid using a small time step are currently in the order of hours for each real-time second. Hence, since the duration of the atmospheric lyophilization of a food product extends for many hours, the CFD simulation of this process considering the whole fluidized bed becomes prohibitive unless a multi-scale approach (as the one applied by Rasetto *et al.* (2010) for VFD) is considered for.

The main scope of this doctorate work was to simulate atmospheric freeze drying (AFD) of food with use of adsorbent by applying computational fluid dynamics (CFD), and validate the CFD model with experiments.

Due to its previously mentioned characteristics, non-food wheat bran was proposed as adsorbent (instead of an inorganic adsorbent material like zeolites, or refined organic material as semolina), resulting in segregation. Consequently, part of this work was focused on the investigation of this phenomenon.

Main scopes

The general objectives of the present thesis are to determine the hydrodynamic conditions under which AFD in adsorbent fluidized bed is feasible, and to obtain a first approach to a CFD model of the process. To reach these scopes it is necessary to work in the experimental as well as in the theoretical fields. Thus, the particular objectives from the experimental point of view are the following:

- To obtain the physical properties of the food materials involved (such as density, geometric characteristics, etc).
- To study the hydrodynamics of the process in a fluidized bed as well as in

a spout-fluid bed. For this purpose, the conditions at the initial, intermediate, and final stages of the process will be physically simulated (employing fresh, partially lyophilized and completely lyophilized food), and the effect of different operating variables on mixing will be evaluated. More specifically, experiments of fluidization of binary mixtures (composed of wheat bran and foodstuff) at different air velocities, applying different product to adsorbent ratios, utilizing diversely shaped food particles will be carried out. In addition, in order to measure the mixing level quantitatively, segregation indexes will be applied.

On the other hand, the objectives from the theoretical point of view are:

- To assess the type of geometry to be used (2D/3D) in CFD simulations, and obtain a general rule of thumb allowing the generation of the different grids to be used for simulating different fluidized beds.

- To evaluate the possibility of simulation by means of a CFD code of the AFD process by immersion in adsorbent medium in a fluidized bed. For this objective, the evaluation of the available models for momentum, heat, and mass exchange, and the determination of those that show the best agreement with experimental results is intended as a first step.

Thus, the thesis will be structured in four main parts: I. Theory and fundamentals, II. Materials and methods, III. Results and discussions, and IV. General conclusions.

Part I will present general theoretical concepts and fundamentals for the whole work, whereas in the part II the procedure will be written separately in two chapters; one for description of experiments, and the other one for describing the computational aspects. In part III, however, the results will be divided in different chapters according to the aspects studied in each one, presenting a particular conclusion of the chapter at the end. Finally, the general conclusion of the thesis will be written in a more general way covering the entire work.

Part I

Theory and fundamentals

Chapter 2

The Freeze Drying

Lyophilization (or freeze-drying) is a process where previously frozen material is dried by means of ice sublimation at low temperature. Normally, it consists of a primary drying where frozen water is removed, and a secondary drying where remaining bounded water is evaporated. Basically, this process can be performed either at atmospheric pressure (atmospheric freeze drying, AFD), or under vacuum (vacuum freeze drying, VFD), and it might be combined with the application of microwaves (Eikevik *et al.*, 2012), ultrasound (Bantle and Eikevik, 2011), and other methods to enhance and/or accelerate drying. Figure 2.1 schematically represents some of the different types of freeze-drying technologies.

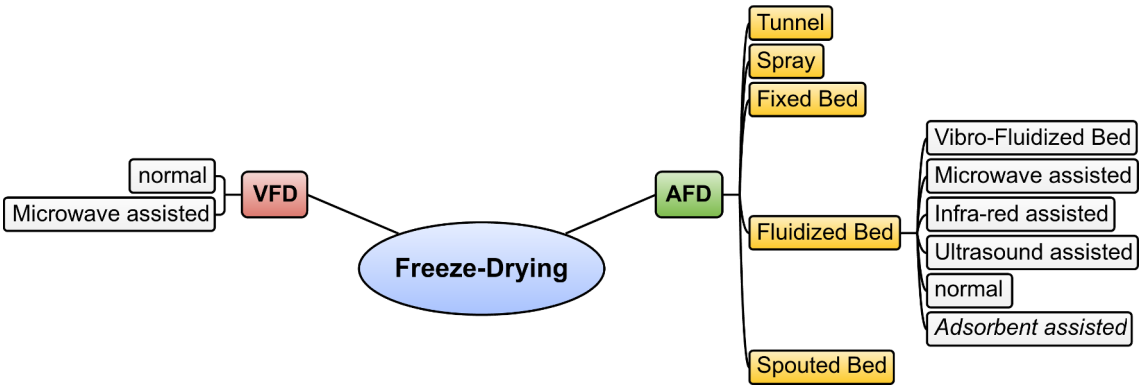

Figure 2.1: Some of freeze-drying technologies (*normal* means that no additional energy supply or process modification is applied).

The most widespread kind of freeze drying is vacuum freeze drying, generally carried out at low pressure (in the order of few pascals). However, due to its cost from the energetic point of view, it is profitable only for application to highly added value products such as pharmaceutical materials or fine foodstuffs.

Nonetheless, atmospheric freeze drying was getting importance in the last years

for industrial food applications, due its relatively reduced operative costs and good quality of obtained products. Many authors have been working on this process during the last three decades, investigating different factors affecting heat and mass transfer, improving them with some extra energy supply, and/or evaluating final product quality from the point of view of shape, colour, or rehydration capacity (Boeh-Ocansey, 1985; Donsì *et al.*, 2001; Bustos *et al.*, 2010; Reyes *et al.*, 2011). Moreover, as it can be seen in Figure 2.1, a notable diversity of techniques are known for carrying out the AFD process.

Additionally, in Table 2.1 a comparison among different freeze-drying technologies is reported in terms of their drying times, operation temperatures, and their main features. It can be noted that a reduction of about 90 % of water content and drying times comparable with VFD drying times were obtained in techniques involving AFD. Furthermore, reported quality of dried products with AFD is similar to quality of those obtained by freeze-drying with VFD. Nevertheless, AFD has to be combined in all the cases with some other technique, allowing to remove water vapour from air, and/or enhancing the drying rate by applying an extra energy supply.

Among the AFD technologies, the tunnel freeze-drying, fixed bed, spouted bed and fluidized bed can be mentioned. In the first case, the apparatus consists of two main parts. In the first one, the air is dehumidified and cooled, whereas in the other subunit, the food product is transported by a conveyor belt or in trays and dried. This technology allows a straightforward implementation of a continuous process, but depending on the product characteristics, large equipment may be required due to long drying times. Claussen *et al.* (2007a) worked on modelling and simulation of this technology and the estimation of processing times in good agreement with experimental results.

A fixed bed for AFD, like the one utilized by Eikevik *et al.* (2012), consists of a chamber, which is filled with the product, covered by a perforated plate for air inlet and outlet at the bottom and the top, respectively. In addition, the equipment used by the authors posses a microwave emitter on its sides for performing experiments applying MW technology. Similarly, an infra-red lamp can be applied instead of the MW emitter, as it was employed by Bustos *et al.* (2010) and Reyes *et al.* (2011) in a fluidized bed.

If liquid products are considered, a spouted bed for freeze drying seems to be an interesting possibility. In this case, the product is previously frozen by spraying it through a ultrasonic nozzle in countercurrent to cold air. Then it is freeze dried in a spouted bed (the sublimation chamber), significantly improving heat and mass transfer due to the active hydrodynamic conditions. Menshutina *et al.* (2005) used experimental data obtained with this apparatus for validating their mathematical model. Despite they used manitol, an excipient used in the pharmaceutical industry, the process may be applied in food industry for freeze drying fruit juices or soups.

In AFD assisted by an adsorbent material in fluidized bed, the process may be carried out either by immersing the food product in the adsorbent (LIAM, *Lyophilization by Immersing in an Adsorbent Medium*), or by circulating the humid air through a fixed bed of adsorbent placed after or before the fluidized bed outlet or inlet. Another possibility for removing moisture from the air is the application of a heat pump. In this case, air is treated in a refrigeration circuit where, after cooling it in an evaporator, the resulting condensed water is drained. Then, air is reheated to the operative drying temperature (further description can be found in (Strømmen *et al.*, 2005) and (Alves-Filho and Goncharova-Alves, 2012)).

In particular, various researchers have been investigating the main variables influencing the AFD in fluidized beds. However, since this process is usually carried out with air at temperatures between -15 and -5 °C, it can saturate rapidly. This situation leads to a reduction of the gradient of water concentration between air and product surface, and consequently, a diminution of the mass transfer rate. In order to preserve low water partial pressures in the air along all the bed LIAM is presented as a good alternative. At the same time, the use of the adsorbent medium presents two additional advantages: the first, as the heat of adsorption of water vapour is of the same order of magnitude than sublimation heat of ice, no additional energy supply is necessary; second, it acts as adsorbent medium for generated water vapour, allowing air recirculation, which means an additional reduction of operative costs.

Donsì *et al.* (2003) investigated the influence of many factors such as freeze drying temperature, fluidization velocity, nature of adsorbent material, size of adsorbent particles, and product/adsorbent weight ratio on drying rate employing different materials as adsorbent, and potato discs as product. The experiments were performed in a 8 cm ID by 45 cm height fluidized bed, and the authors found that fluidization velocity has no important effects on drying rates, and at low product concentrations the process is accelerated, whereas at high product concentration the product segregates leading to poor contact with the adsorbent.

Wolff and Gibert (1990) developed a model for the simulation of atmospheric freeze drying process, under certain assumptions. They carried out some experimental runs in a fluidized bed that reflected the influence of parameters such as temperature, water content, product to adsorbent mass ratio, shape and size of the product to be dehydrated, and temperature for adsorbent regeneration. They used potato slices as the product and starch as the adsorbent. Nevertheless, the authors did not mentioned whether segregation phenomena or channels formation were present or not.

Due to its compatibility with food products and very low price, since it is a by-product of wheat processing, non-food wheat bran seems to be a promising material to be applied in AFD.

Focusing on energy requirements, Donsì *et al.* (2001) obtained two curves of energy requirements in function of the initial water content considering the sensible

heat of refrigeration and freezing, heat of sublimation, heat of condensation, energy consumption of the vacuum pump, and energy for defrosting for vacuum freeze drying (VFD), and the sensible heat of refrigeration and of freezing, the energy for bed cooling, regeneration of adsorbent, and energy consumption of the blower for the case of AFD. They found that for initial product absolute humidity greater than about 0.8 kg_w/kg_d, the energy demand for freeze-drying considering the VFD considerably increases compared with AFD.

Moreover, in an extensive paper review about freeze-drying, Ratti (2001) reported that the AFD process is about 34 % less energy demanding than the VFD process. Nevertheless, the time required for lyophilizing a product increases 1-3 times. In addition, special care should be taken in operative conditions because of an increment of the risk of product collapse. For microwave-assisted VFD process, the author found that despite a reduction of about 60-70 % of drying times were reported, a reduction of process costs is not always guaranteed.

On the other hand, Claussen *et al.* (2007b) in their paper review highlighted that some authors reported that in the heat-pump assisted AFD the SMER (Specific Moisture Extraction Rate) decreases between 73 and 93 % with respect to the conventional VFD.

Table 2.1 Drying times, operating temperatures, and salient characteristics of the optimum findings reported by different authors in freeze-drying.

Technology	Product	t_{drying} (h)	T_{op} (°C)	Moisture reduction (%)	Salient characteristics	Notes	Reference
combined AFD FB IR ADS-no-mix *and* HAD	murtilla berry	7 AFD + 6 HAD	-5 AFD + 15 HAD	92 (50 with AFD)	- Similar sensory attributes than products in VFD. - Products obtained with application of IR have greater resistance to fracture.	optimal conditions	Bustos *et al.* (2010)
AFD FB ADS-no-mix *and* HAD	murtilla berry	7 AFD + 6 HAD	-5 AFD + 15 HAD	89 (45 with AFD)			
VFD	murtilla berry	13		97			
AFD FB MW	"loco" (mollusc)	12	-5	62			Pérez *et al.* (2011)
VFD MW	"loco" (mollusc)	6.5		97	- Drying times are significantly reduced (almost halved) by applying MW. - Porosity is augmented allowing a good rehidratation.		
combined AFD LIAM *and* VFD	cereal food paste	4.5 to 5	-10 AFD + 0 to 15 VFD + -10 AFD	90	- Using three drying periods combining atmospheric and low pressure, and different temperatures, improves the drying rates in LIAM without excessive quality loss.	- optimal conditions, three periods. - VFD at 54.7 kPa.	Lombraña and Villarán (1997)
combined VTD-AFD LIAM-VTD	shrimps	32	-10 (AFD), 28 (VTD)	98	- Drying time of the some order than vacuum freeze drying. - Quality (rehydration capability, porosity, and texture) comparable with VFD.	- optimal conditions: three stages, VTD-AFD LIAM-VTD. - adsorbent: semolina.	Donsì *et al.* (2001)
AFD FiB MW	green peas	≈ 5	-3	≈ 70	- Drying times applying a MW radiation of 280 W halved with respect AFD without MW. - No significant differences with FB. - Best product quality.	- optimal conditions.	Eikevik *et al.* (2012)

continued on next page

Technology	**Product**	**t_{drying} (h)**	**T_{op} (°C)**	**Moisture reduction (%)**	**Salient characteristics**	**Notes**	**Reference**
combined AFD FB IR ADS-no-mix *and* HAD	apple	10 AFD + 6 HAD	-5 AFD, 25 HAD	95	- Different pretreatment processes were also tested: Low freezing increases drying rates which are enhanced by the application of the IR. - No differences in sensory attributes were found between products processed by AFD and VFD.	- Optimal conditions.	Reyes *et al.* (2011)
combined AFD HeP + HD	apple cubes	40	increasing from -16 to 16	98	- Optimal drying trajectories with low oxidative activity and lowest shrinkage.	- optimal conditions.	Witrowa-Rajchert *et al.* (2007)
AFD Tunnel	apple	76	-5	98		- Optimal conditions.	Claussen *et al.* (2007a)
	turnip cabbage	45	-5	98			
	cod	20	-5	93			
LIAM FB	potato slices	30	-6	97	- AFD reduces plant and energetic costs. - The drying process is improved by using an adsorbent. - The gaseous environment enhances the external mass and heat transfer coefficients. - Optimum mass	- With semolina, called bran in the article, as adsorbent. - Potato slices diameter 6 mm.	Donsì *et al.* (2003)
LIAM FB	potato slices	7.5	-5	98	- Best results obtained using thiny-sliced products. In particular, they should not exceed 5 mm thick. - The URIF model was proposed, with good agreement with experimental data.	- With starch as adsorbent. - Potato slices diameter 2 mm.	Wolff and Gibert (1990)

—
HAD: Hot Air Drying; MW: Microwave; IR: Infra-red; HeP: Heat Pump; VTD: Vacuum Thermal Drying (at 28 °C); FiB: Fixed Bed; FB: Fluidized Bed
ADS-no-mix: Adsorbent placed in an independent fixed bed.
optimal conditions: When only the optimal conditions found by the authors are reported.

2.1 Mathematical modelling of AFD

Since the AFD in Fluidized Bed (AFD FB) is the most widespread technique for freeze-drying under atmospheric conditions, special emphasis will be put in analysing the available mathematical models in literature. First of all, as a system to be considered it can be defined the entire fluidized bed. That is, the equipment itself (with its geometrical characteristics), air, and fluidized particles inside of it. Consequently, this system is composed of: incoming air (at a given temperature, moisture content, and velocity), food particles drying inside (whose water content, velocity, and temperature are changing in time), and adsorbent particles (in case of using it) or incoming energy (like MW or IR).

According to these definitions, it could be said that practically all the mathematical models found in literature do not consider the system as a whole, but only some of its components. Most models found, like URIF (Uniform Retreading Ice Front), take into account the heat and mass exchange between particles, and are able to predict the change of particle temperature and water content in time. Nonetheless, the majority of the models are limited only for predictions of the evolution of product particles water content with time for specific cases.

As it was previously mentioned, the model proposed by Wolff and Gibert (1990) was the URIF which is a one-dimensional model based on the following assumptions:

- The drying product is separated in two parts: the frozen core and the dried layer.
- Water vapour and ice are in equilibrium in the interface between ice and the dried layer. Sublimation takes place in the ice front, leading to its uniformly retreat.
- Quasy-steady state is considered. The variation on mass and heat resistances is considered by the variation of the dried layer thickness.
- All the arriving energy is employed for sublimating ice (i.e., air does not withdraw energy).
- Shrinkage is negligible, and the product is considered homogeneous and isotropic. There is perfect mixing is between adsorbent and product.

The heat and mass transport equations are, respectively,

$$m_{Pw0}\frac{d\left(1-x_w^*\right)}{dt} = \frac{A}{\Delta\hat{H}_{sv}}\frac{1}{\frac{1}{h_{ex}}+\frac{e_s}{k_s}}\left(T_{ai}-T_{fr}\right) \tag{2.1}$$

$$m_{Pw0}\frac{d\left(1-x_w^*\right)}{dt} = A\frac{1}{\frac{1}{\beta_{ex}}+\frac{RTe_s}{D_w M_w}}\left(P_{w,fr}-P_{w,ai}\right) \tag{2.2}$$

Lombraña and Villarán (1997) adapted the URIF to spheric shaped particles, and applied it together to other correlation to experimental data determining model

parameters. They considered cases of AFD LIAM and VFD LIAM obtaining reliable values for these parameters.

Assuming the quasy-steady state during AFD LIAM in FB, Donsì *et al.* (2003) obtained relationships for heat and mass transfer between cylindrical potato particles and the surrounding mixture (composed of adsorbent and air). These equations relate the driving force (temperature difference or water partial pressure difference) between the frozen front and the emulsion, allowing to obtain product and process properties such as the effective water vapour diffusivity or heat exchange coefficient. Nevertheless, it does not constitutes a model for AFD simulation.

Stawczyk *et al.* (2007) simulated with CFD the AFD of an apple cube in 2D by applying a film sublimation model and the URIF model by subdividing the cube in four zones: a pure ice plate (the frozen front), an interface, a porous zone (the dry front), and a gaseous phase. The ice front was assumed as a wall from which ice sublimates, and the sublimation rate was calculated by means of an user-defined function. Thus, the effect of the generated water vapour on the species distribution of the gaseous phase was introduced into the flow computations through a source term applied to the adjacent walls. In addition, the authors assumed the dried layer as a porous media simulating the flow through it by applying the corresponding model included in the CFD software, and reproduced the retreating ice front by using 13 separate meshes for different ice front positions. Despite the authors obtained a reasonable agreement with the experimental results, they only simulated the process of a piece of product but not the entire AFD process.

Similarly to the previous case the Nam and Song's sublimation-condensation model (Nam and Song, 2007) considers an unsaturated porous medium for describing the food product composed of a solid matrix, spaces partially occupied by ice, and empty spaces. This model, initially proposed for VFD, was adapted for AFD and applied for simulating the AFD of carrot slices by Quijada *et al.* (2009). They solved the differential transport equations by finite differences (considering mass and heat transport in one direction, 1D) and evaluated different aspects from the mathematical point of view of the method (like the influence of the time step) as well as from the point of view of the results (such as the progress of the retreading ice front). In addition, they extended their model to a bidimensional particle (Bubnovich *et al.*, 2012), analysed the effects on energy and mass transport in terms of the particle geometric ratio (thickness to width ratio), and compared them with the 1D case. In the 2D case, the ice front is not flat, and the URIF assumption does not hold. Comparing the 2D and 1D simulations, their results showed differences for geometric ratios greater than 0.125. Anyway, they did not consider the whole fluidized bed, but only a piece of food material assuming dry air around the food particle.

Also Alves-Filho (2010) applied a model for AFD FB considering the particle as a porous medium, but in this case they used practically spherical particles of

protein material from fish muscle. They solved the mass transport equation for a single particle by means of a sweep method.

The AFD FB of "murtilla" berry (a Chilean berry food) was simulated by Bustos *et al.* (2010), using the URIF model for the primary drying and the Page empirical model,

$$\frac{X}{X_0^*} = exp(-kt^n), \tag{2.3}$$

for the secondary drying stage. The URIF was adapted for semi-spherical particles for the primary drying, whereas the parameters n and k of the Page model were obtained by fitting experimental data. Despite this last model well describes the drying times, it is obviously valid for only the presented specific case, and does not deals with the mass and heat transfer kinetics. Although the authors use IR radiation in some of their experiments, they applied the URIF (a model which does not consider energy radiations) for predicting the first stage of drying, appreciably agreeing with part of their experimental results. This situation may be attributed to a slight S-estimation of the modelled drying times rather than to a good experimental-model agreement.

Reyes *et al.* (2011) in their investigation evaluated the parameters of the Simplified Constant Diffusivity Model (SCDM, Equation 2.4) and the Page model for the first and second drying periods of apple slices. Since the SCDM and the Page models are empirical, they allow the prediction of drying times and moisture content for the specific products where they were applied. However, the effective diffusivity values obtained with the SCSM model can be utilized in other AFD models.

For a parallelepiped of dimensions of 2L×2H×2W, the SCDM master equation is,

$$\frac{X}{X_0} = \phi_x\phi_y\phi_z = exp\left(-\frac{\pi^2}{4L^2}D_{eff}t\right) exp\left(-\frac{\pi^2}{4H^2}D_{eff}t\right) exp\left(-\frac{\pi^2}{4W^2}D_{eff}t\right) \tag{2.4}$$

Kolsaker *et al.* (2011) and Eikevik *et al.* (2012) used a modified Weibull model (Equation 2.5) for describing the drying behaviour of the AFD FB and the AFD FB MW, respectively. This model takes into account the physical dimensions of the product particle (L, length or characteristic length), a calculated diffusivity, and considers a (mathematical) shape factor (β). Similarly to the Page and the SCDM models, by fitting the equation to experimental data it is possible not only to evaluate the time evolution of the drying process, but also the diffusivity.

$$\frac{Z - Z_{eq}}{Z_0 - Z_{eq}} = exp\left(-\left(\frac{D_{calc}t}{L^2}\right)^{\beta}\right) \tag{2.5}$$

An URIF based model was applied by Pérez *et al.* (2011) for simulating AFD FB and VFD of "loco" cubes and slabs with and without MW. Besides, they adjusted their experimental results with two Fick's law based models; the previously mentioned SCDM and the VDM (Variable Diffusivity Model), applying the latter as follows:

$$\frac{X}{X_0} \approx exp\left(-\lambda_1^2 Fo\left(1+\frac{b}{2}Fo\right)\right) \tag{2.6}$$

(where λ_1 and b are parameters of the model, and Fo is the Fourier number, $Fo = D_0 t/a^2$, with D_0 as the diffusivity at $t = 0$)

They obtained the URIF model best fit for slabs under AFD without MW. Regarding to the Fick's law based models, they found the best adjustment with the VDM (particularly in VFD cases without MW).

Summarizing, as it can be seen there are many modes of simulating the AFD process, either for specific cases or applicable for more than one case. Notwithstanding, none of these works considers the whole fluidized bed and the possible interactions between food product and adsorbent when AFD LIAM FB is applied. Since in this process two different solids of different sizes and densities are fluidized, segregation may take place, leading to a poor contact between adsorbent and foodstuff. Thus, the drying times may be increased as shown by Donsì *et al.* (2003). If a model is wanted for equipment design and/or process optimization, this possibility should be also contemplated.

An interesting approach for considering the whole fluidized bed is the one applied by Di Matteo (2002) in her PhD thesis. She extended the model of Kunii and Levenspiel for fluidized bed reactors (Kunii and Levenspiel, 1991) to AFD LIAM FB. The original model considers three phases; bubble (gas), cloud (surrounding the bubble), and emulsion, and the mass transfer exchange takes place between the bubble and the cloud, and the cloud and the emulsion. In the extended model, four phases were considered; bubble (gas), emulsion, adsorbent phase (solid), and product phase (solid). In addition, two S-models were considered for the solid phases: the sorption isotherms were considered for the adsorbent, while the URIF adapted to cylindrical particles was applied for the product freeze-drying.

Another possibility for simulating the AFD LIAM FB taking into account the whole system, as it was defined at the beginning of this section, may be by means of Computational Fluid Dynamics. With this tool, not only the mass and heat transfer could be simulated, but also the entire velocity field of each phase and their interactions. Moreover, variables which present difficulties to be experimentally tracked such as phase velocities, local exchange coefficients, or temperature gradients, might be theoretically followed. This would allow to develop and theoretically test new equipments and techniques without performing experiments. Nevertheless,

suitable models for simulating these systems should be developed first, adapting the submodels for adsorption and foodstuff drying into CFD methods, and/or finding mathematical models for simulating the behaviour of cohesive/pseudo-cohesive solids (for some adsorbent like starch or wheat bran).

Chapter 3

Fluidization

3.1 Fluidized beds, fluidization regimes, and powders classification

When a fluid is passed upward through a bed of particles (supported on a perforated or porous plate), at a velocity such that the drag force produced is enough to counterbalance particles weight, fluidization occurs. Depending on the kind of solid involved, fluid utilized and air velocity, the behaviour exhibited by the fluidized bed may be minimum fluidization, bubbling fluidization, slugging, turbulent fluidization, channelling, or fast fluidization with pneumatic transport. According to how a powder behaves in a gas fluidized bed, Geldart (1973) proposed a classification in four main categories as a function of the difference between particle and fluid density, and mean particle diameter. This classification was extended by other authors establishing intermediate regimes or adapting it for cases in which high pressure and temperature are used.

The main categories in Geldart's classification are: A, aeratable (small mean particle density and low density), notable bed expansion before bubbles appear, and small bubbles when they are formed at high air velocities; B, sandlike (size between 40 µm and 500 µm, and densities between 1400 and 4000 kg/m^3), well fluidized and vigorous bubbling; D, spoutable (high densities and/or large particle size), severe channelling and large bubbles exploding, or spouting behaviour; C, cohesive (fine particles), very difficult normal fluidization due to interparticle forces grater than drag forces, leading to formation of channels, cracks, or discrete solid plugs.

3.2 Pressure drop oscillations in fluidized beds

One of the most important indicators of the dynamics of a fluidized bed are the pressure drop oscillations. They depend on particle properties, bed characteristics, and air velocity, and might be related with bubbling, slugging, or turbulent fluidization. Bi (2007) published an extensive paper review about the pressure fluctuation phenomenon addressing it from the point of view of the measurement methods, causes, modelling, and so on. In the literature he found six main sources of oscillations. The first one, bubbles passing by the pressure measurement probe. In second place, pressure drop oscillations caused by bubble eruptions at the upper bed surface which is associated with bubble size. The third source is the mechanical vibration of the fluidized particle bed. The fourth origin of pressure drop oscillations is the gas plenum chamber beneath the distributor due to the compressibility of gas in the chamber. Finally, in fifth and sixth places are the pressure drop fluctuations caused by bubble coalescence and splitting, and bubble formation.

3.3 Cohesive solids

As it was previously said, in cohesive powders (Geldart C) the interparticle forces are considerably greater than the hydrodynamic forces, and cannot be overcome by the gas. Consequently, the particles are not separated by the fluid, and it escapes by forming channels giving an unsatisfactory fluidization. In the framework of a project for locating the Geldart A/C borderline, Geldart *et al.* (1984) studied the fluidization behaviour of various Geldart A and Geldart C powders with densities ranging between 350 and 2800 kg/m^3 and particle diameters lying between 5 µm and 125 µm. For cohesive solids, in first place, they found that it was practically impossible to measure the pressure drop due to its continuously variation in time, probably caused by the creation, collapse, and re-formation of channels. In addition, they observed that these channels or cracks were generated numerously in horizontal or sloped directions, and a bed expansion without true bubbles formation. Only some small bubbles were reported "wiping out" the cracks which regenerate with different inclination and length.

Furthermore, Visser (1989) analysed different factors affecting the cohesiveness of powders (Geldart A, and particularly Geldart C) such as van der Waals forces, geometrical factors, and capillary forces. They stated that the main cohesive forces between particles in a powder are van der Waals forces. However, depending on the particle density, porosity and surface roughness these forces are perceived only by very small particles (few microns or less). Thus, only Geldart C particles can be influenced by cohesive forces. Furthermore, particle geometry, presence of fines, particle size distribution, and/or adsorbed molecules affect the magnitude of these

forces as well.

Sundaresan (2003) published an exhaustive literature review about fluidization organizing the knowledge of the origin and hierarchy of organized flow structures in fluidized beds, differentiation between bubbling and no bubbling systems, and stages of bubble evolution. Focusing on cohesive systems, they analysed their behaviour in terms of concepts such as compressive yield strength, particle-phase normal stress along the vertical direction, tensile stress (as a measure of cohesion between particles in a assembly), and pressure-drop overshoot. It is recommended reading this article if a more specific study on cohesive solids and their modelling is intended. However, it is beyond the scopes of the present work and it will not be longer treated here.

3.4 Spouted and fluid-spouted beds

Spouted bed is gas-solid contactor in which the gas is introduced through a single orifice from the centre, resulting in a systematic cyclic pattern of solid movement inside the bed. A spouted bed has three different regions: the annulus, the spout, and the fountain. At stable spouting process, a spout appears at the centre of the bed, a fountain appears above the bed surface and an annulus forms between the spout and wall. On the other hand the annulus region is more like a packed bed. At partial spouting case, there are two distinct regions, an internal spout which is similar to a fluidized bed and the surrounding packed particle region similar to a packed bed (Sahoo and Sahoo, 2013).

On the other hand, Malek *et al.* (1965) differentiated three fluidization regions as air velocity is increased:

1. **Packed bed:** At low air velocity. The gas passes through the bed without disturbing solid particles. The pressure drop practically depends linearly on the air flow rate.
2. **Transition bed:** At a certain air velocity a cavity is formed at the bed bottom, lifting solid particles upward from the air injector. As air velocity is further augmented, some particles start spinning rapidly inside the cavity around the internal spout. Then, an arch of non uniform thickness is formed. Pressure drop continues growing with the increase of air velocity and reaches a maximum coinciding with a maximum of the bed expansion. Further increasing of air flow rate increases the height of the internal spout, the bed expands, and pressure drop above the internal spout also augments.
3. **Spouted bed:** Increasing air velocity up to a certaing point, the fountain is formed, and particles are dragged by the central spout. The pressure drop decreases abruptly and remains constant almost independently of air flow rate. The bed behaves as previously described.

In order to improve the material circulation and solid mixing, some modifications might be made to the spouted bed. Based on the modifications applied by various authors, Sutanto (1981) utilized a special spouted bed possessing, adding to the central air supply, auxiliary air injectors located in the lower section of the bed. This modified apparatus was called "spout-fluid bed", and presented better solids mixing and annular solid-fluid contact than standard spouted beds, and better performance when cohesive solids were used. He studied different aspects of the fluidization in this kind of apparatus such as regime maps, minimum fluid flowrate for spouting with aeration and spout-fluidization, and annulus gas velocity profile. Thus, he established four types of flow regimes for different central flow/auxiliary flow combinations: packed bed, spouting with aeration, spout-fluidization and jet in fluidized bed. Moreover, he observed that fountain height decreased as the proportion of auxiliary flow augmented, and its solids concentration increased.

In recent years many works were published aiming the study of spout-fluid beds, their hydrodynamics (Zhong *et al.*, 2006a), fluidization regimes (Link *et al.*, 2005) (Zhang and Tang, 2006), correlations for predicting fountain height, numerical simulations (Zhong *et al.*, 2006b; Wang *et al.*, 2014), etc. However, as only the mixing capabilities of this kind of bed are of interest to the present work, no longer discussion about those papers will be dedicated.

3.5 Mixing and segregation of binary mixtures in fluidized beds

In general terms, when solids of the same size but different density are mixed in a fluidized bed, rapid segregation takes place with the denser material forming a relatively pure bottom layer, and sparse but uniformly distributed amount of denser material in the top layers. On the other hand, when solids of the same density but different size are fluidized, segregation occurs more difficulty, and it is expected an increment of this phenomenon when size distribution increases. All solids are carried up with bubble wakes, but only the larger/denser particles preferentially move down the bed as the bubble ascends (Kunii and Levenspiel, 1991).

In particular, from experiments utilizing six binary mixtures combining materials with different properties (density, size, and minimum fluidization velocity) in a two-dimensional fluidized bed, Rowe *et al.* (1972b) concluded that density differences are the main causes of segregation in gas fluidized beds, whereas size differences have slight influence when the mixure is made up of particles of equal density and different size. In addition, they introduced the concepts of *jetsam*, component tending to sink to the bed bottom, and *flotsam*, component tending to float to the bed top. Moreover, the authors found four main segregation mechanisms:

1. Lifting of particles enclosed in rising bubble wakes: a bubble originated near the bed bottom carries up closer material.
2. Falling through bubbles: gas velocity is not enough to support large and dense particles, and they fall through the free space of a bubble.
3. Inter-particle percolation: small and denser particles through large and light ones in a region recently disturbed by a passing bubble. It never takes place against ascending air.
4. Quasy-hydrostatic effect: does not cause segregation, but preserves it. Light particles "float" on a bed of denser particles.

Furthermore, according to Rowe *et al.* (1972a), segregation presents a great dependence on air superficial velocity, and even strongly segregating systems can be mixed or separated by adjusting air superficial velocity. On the other hand, the main effect of size was to modify the mixture minimum fluidization velocity (u_{mfM}). In addition, they found that the u_{mfM} is notably reduced by adding a small quantity of a fine powder, whereas the opposite (i.e. the addition of a coarse particles to a fine powder) has a very reduced effect on u_{mfM}. In their experiments the authors used binary mixtures composed of fine and coarse materials with the scope of measuring the segregation in function of particle properties (size, density, and gas flow rate).

Qiaoquna *et al.* (2005) studied the effect of particle properties and processing variables such as air velocity or mass fraction on segregation phenomenon employing two different binary mixtures containing a biomass material, rice husk, and other solid material, sand or silica. Their results were in accordance with the previously mentioned works; they observed that when increasing superficial gas velocity, the mixing between rice husk and sand particles becomes stronger, since sand particles are transported by bubbles from the bottom to the top, whereas rice husk is carried from the top to the bottom by particles circulation. They found, however, that an increment on mixture mean diameter, by means of either augmenting rice husk averaged mass fraction or using silica particles with greater diameter, increases the mixture minimum fluidization velocity, which is traduced as a reduction of air excess velocity (U-U_{mf}). Consequently, the segregation of the particulate system is reinforced.

Regarding to fluization time, according to Wu and Baeyens (1998), the minimum elapsed time required to reach segregation equilibrium depends on the excess velocity used (U-U_{mf}) and the larger to smaller particle diameter ratio. For excess air velocities greater than 0.16 m/s, 20 minutes are enough to achieve mixing equilibrium. Moreover, the same fluidization time is sufficient for diameter ratios up to 4.8. In addition, the air excess velocity needed to reach good mixing is strongly dependent on the diameter ratio. For diameter ratios between 1 and 2, mixing is quickly reached at very low values of excess air velocity. However, for greater diameter ratios the needed (U-U_{mf}) grows rapidly.

As it was previously stated, one of the main mixing factors in non-cohesive systems are bubbles, which carry particles in their wakes. The number and size of bubbles might depend on air velocity, and particle size distribution (PSD). Chew and Hrenya (2011) have investigated the influence of the PSD width (standard deviation to Sauter mean diameter ratio) of polydisperse mixtures on segregation patterns using different normal and log-normal sand distributions. They found that a bubbleless layer at the bottom of the bed was observed in those experiments exhibiting the greatest segregation behaviour, and the larger this layer, the greater the segregation.

Nevertheless, most of the previously mentioned works and other papers found in literature were carried out using non-cohesive powders forming binary mixtures whose components had diameters not greater than one or two millimetres. Besides, in most of the cases spherical or nearly spherical particles were utilized in the mixtures. Therefore, there is a lack of information about the behaviour of fluidization of binary mixtures of a cohesive or pseudo-cohesive solid and not spherical particles with equivalent diameters in the order of centimetres.

Concerning to mathematical models for segregating fluidized beds, Gibilaro and Rowe (1974) proposed a general model based on the fact that bubbles are the main mixing (or segregating) agents, transporting solids in their wakes. They considered two phases, bulk and wake, and four physical mechanisms for describing three ways of mixing and one of segregation, as follows:

- Mixing mechanisms:
  - Overall particle circulation: Particles are transported by the bubbles wakes from the bed bottom to the top. (in other words, *Lifting of particles enclosed in rising bubbles wakes* as described by Rowe *et al.* (1972b))
  - Exchange: Solids exchange between bulk and wake phases.
  - Axial mixing: Bubbles may produce some axial mixing, which was described by means of a pseudo-diffusivity.
- Segregation: Supposed that the quantity of segregating solid at any point of the bed is proportional to the concentration of jetsam at that point.

They applied the model to three main cases of strongly segregating systems: without considering exchange and axial mixing mechanisms, considering only the effect of phases exchange, and considering all mixing effects. In sum, they not only obtained an accurate model for describing mixing and segregation of a fluidized bed, but also found that phase exchange can be neglected, and axial spreading is important only at high velocities.

3.5.1 Segregation indexes

In order to quantify and characterize somehow the mixing or segregation of a binary mixture, a considerable number of indexes were developed along the years. Most of them were proposed for analysing the quality of mixtures in mixers (in terms of perfectly ordered, randomly mixed, or totally segregated mixture), and/or the performance of these equipments. Fan *et al.* (1970) reviewed the literature about mixing and reported more than 20 existing indexes published up to then. A wide quantity of these indexes were formulated for mixing processes in mixers and based on statistics. In this line, Cooke and Bridgewater (1977) proposed a distribution index considering the probability of a particle falling in a given division of a sample tray for evaluating the mixture quality. From the experimental point of view, the application of this index allows to use different sample size for evaluating the apparatus, and in terms of its results it permitted to identify random and totally segregated mixtures.

Poux *et al.* (1991) reviewed the definitions of mixture quality and different kind of segregation indexes for binary and multicomponent mixtures based on either statistical analysis, parameter definition, experimental work, or a combination of these methods. They did not test the performance of the indexes, but only presented them, suggesting that the index to be chosen depends on the characteristics of the case of study.

On the other hand, Barresi *et al.* (1996) applied autocorrelation methods and a variance based index for quantitatively evaluating the mixture structure of sintered ceramics. They characterized the current mixture by comparing the correlogram of an experimental mixture with the correlograms corresponding to random and ordered mixtures. In addition, they measured the intensity of segregation through an index proposed by an I.Chem.E. working group on mixing of powders, which involves the standard deviations of the current mixture, of a completely segregated mixture, and of a random mixture.

Nevertheless, the majority of these indexes have been defined for cases where the number of particles can be relatively easy counted, and only small samples from the whole case are analysed. A completely different situation is found for the case of a binary mixture composed of a food product and an adsorbent like non-food wheat bran in a fluidized bed. In first place, the entire bed is analysed dividing it in layers, and in second place, the size of adsorbent particles is significantly small (in the order of 600 µm) resulting impossible to count particle by particle. Even if the number of particles of bran and product could be indirectly obtained by dividing the mass by absolute density and volume of a single particle, and each layer were considered as a sample, a considerable error would be introduced in the estimation of the particle volume.

Therefore, many segregation or mixing indexes were developed particularly for

characterizing mixing and segregation in fluidized beds, being some of them based on similar statistical concepts than the previous mentioned methods. Among the most broadly used segregation indexes, there is the M mixing index proposed by Rowe *et al.* (1972a), based on jetsam fractions in the upper part (X_J) and the whole of the bed ($\overline{X}_J$):

$$M = \frac{X_J}{\overline{X}_J} \tag{3.1}$$

This index can be applied as long as the jetsam and flotsam are clearly identified, bottom segregation is preponderantly dominant, and jetsam concentration and particle size are such that eventually one layer whose concentration around 100 % may be produced. Thus, M = 1 corresponds to perfect mixing, whereas M = 0 means complete segregation.

In addition, Wu and Baeyens (1998) reviewed in literature predictive equations for this index, and for mixture minimum velocity calculation, and proposed a new equation for predicting M mixing index based on their experimental results. They performed experiments in gas fluidized beds with many sand binary mixtures of different size particles, investigating the influence of concentration, duration of fluidization, and bed aspect ratio on segregation. According to their findings there is no effect of concentration on mixing index (M).

On the other hand, Mellema *et al.* (2003) developed a segregation index for digital image analysis of segregation in fluidized beds, the "s" index, which takes into account the composition along all the bed of both components of a binary mixture, and scales it with a theoretical maximum degree of segregation of the mixture. The mathematical formulation of the index is the following:

$$s = \frac{S - 1}{S_{max} - 1} \tag{3.2}$$

where S is the ratio of an average particle height of small particles to the same quantity calculated for large particles,

$$S = \frac{\langle h_{small} \rangle}{\langle h_{large} \rangle} \tag{3.3}$$

and S_{max} represents the theoretical maximum degree of segregation,

$$S_{max} = \frac{2 - x_{small}}{1 - x_{small}} \tag{3.4}$$

Moreover, for their studies the authors used particles of two different sizes coloured according to their diameter. Therefore, after taking images during the fluidization and dividing the generated pictures in cells, they analysed the light intensity emitted by the coloured particles, and calculated the solid volume fractions

in each cell from the total area of pixels in each cell identified as particles. Thus, the numerator and denominator of Equation 3.3 were calculated as follows:

$$\langle h_{large} \rangle = \frac{\sum_k x_{large} \alpha_{large,k} h_k V_k}{\sum_k x_{large} \alpha_{large,k} V_k} \tag{3.5}$$

$$\langle h_{small} \rangle = \frac{\sum_k x_{small} \alpha_{small,k} h_k V_k}{\sum_k x_{small} \alpha_{small,k} V_k} \tag{3.6}$$

where $\alpha_{large,k}$ or $\alpha_{small,k}$ is the total particle volume fraction of small or large diameter (depending on the case), x_{small} and x_{large} are the overall mass fractions of small and large particles, and h_k and V_k represent, respectively, the centre of the cell k and the cell volume.

Therefore, a value of 1 for the "s" index corresponds to a completely segregated system, whereas s=0 means perfect mixing.

Despite several indexes were proposed by different authors in order to quantify the segregation level or mixing of a binary mixture in a fluidized bed, none of them is able to describe how a specific component of the mixture is distributed along the bed. In other words, sometimes is important not only to know how the binary system separates from the uniformity, but also the distribution of a certain component of interest. Nevertheless, none of the indexes found in the literature up to now allow this description.

On the other hand, those indexes may be influenced by the experimental procedure used for evaluating the mixture, such as the number of vacuumed layers, or layer thickness, since the solids distribution was measured in layers (or at most in cells) and not in a continuous way along the bed. Consequently, it might be difficult to compare experiments done with non-equal number of layers, fluidized beds of different size, or even more, the comparison between results presented by different authors.

3.6 Summary

Many works have been dedicated to the fluidization in bubbling fluidized beds as well as spouted beds (or its modifications), studying the behaviour of cohesive powders, and explaining and characterizing the segregation of binary mixtures. However, there is a lack of knowledge about how a pseudo-cohesive powder like non-food wheat bran works in a fluidized bed or a spout-fluid bed, its behaviour as component of binary mixture with particles until two orders of magnitude greater, and the link between channelling and mixing.

Therefore, a deeper study about the characteristics of this very cheap material and its hydrodynamic interactions with food particles should be performed before investigating the AFD of food applying it as adsorbent.

On the other hand, a different approach to mixing/segregation indexes is needed allowing a more precise quantification of the segregation phenomenon and comparison between different beds.

Chapter 4

Computational Fluid Dynamics of multiphase fluidized beds

4.1 Finite Volume Method (FVM)

The references of this Section were taken form Ferziger and Perić (2002), Versteeg and Malalasekera (1995), Petrila and Trif (2005), and the ANSYS®Fluent 13 Theory Guide (2010).

Applied to transport phenomena, the finite-volume method evaluates and represents the partial differential equations governing the fluid flow, species transport, and heat exchange, in the form of algebraic equations. The solution domain is divided into a finite number of small control volumes (CVs) by a grid which defines the control volume boundaries, and the conservation equations are integrated in the cells.

Theoretically, as the number of computational cells is infinitely large and the time step size tends to zero (for transient problems), the results obtained with numerical methods should be indistinguishable from the exact solution of the transport equations, independently of the method applied. Nevertheless, in practical cases only a limited number of cells and small enough (but not zero) time step size can be used. Then, the numerical outcomes will be physically realistic when the discretization method posses certain fundamental properties: consistency, stability, convergence, conservation, boundedness, realizability, accuracy, and transportiveness.

4.1.1 Numerical grids

In a few words, the geometric domain where the problem will be solved is discretely represented in a numerical grid, dividing the solution domain into a finite quantity of subdomains (control volumes).

There are many kinds of grids and meshing methods, which are chosen according to the characteristics of the problem to be solved. Some of them are the structured grid, block-structured grid, and unstructured grid.

In the present work structured grids will be used (in both 2D and 3D cases). This grids type, consists of families of grid lines whose members do not intercept among them, but each member of a single family intercepts one member of the other families only once. The location of any control volume within the grid is clearly and uniquely identified by two or three coordinates, for 2D and 3D cases respectively.

Figure 4.1 shows a representation of a typical 2D grid section and the generally used notation. As it is remarked in the figure, in the following sections only the cells sharing faces with the central (or "considered") cell will be called *neighbour cells*.

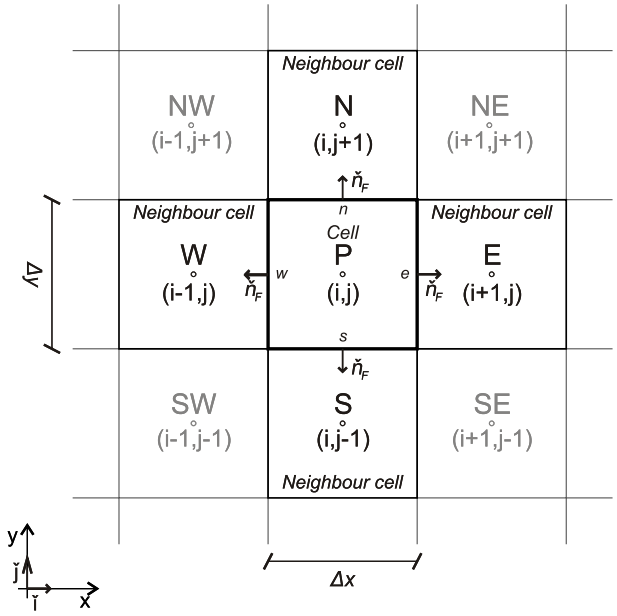

Figure 4.1: Representation of cells in FVM for a Cartesian 2D grid. For simplicity many authors denote the central CV (i, j) with P, whereas the surrounding CV are called E (east), N (north), W (west), and S (south). Moreover, the shared faces with the central CV are identified with e, n, w, and s. In 3D cases, similar scheme is followed, but adding a top cell ($(i, j, k + 1)$ or T) and a bottom cell ($(i, j, k - 1)$ or B).

4.1.2 Properties of numerical methods

Consistency

The difference between the results obtained by solving an equation by numerical methods and the exact solution is known as *truncation error*. It is normally estimated by a Taylor series expansion about a single nodal point in the discrete approximation, recovering, thereby, the original differential equation plus a remainder.

Therefore, a method is considered *consistent* if the truncation error tends to zero when the cell and/or time step size tend to zero ($\Delta x \to 0$, $\Delta t \to 0$). This error is normally proportional to $(\Delta x)^n$ and/or $(\Delta t)^n$, and the method is called as nth-order approximation; $n > 0$ is required for consistency.

In some methods, the truncation error is proportional to a ratio between cell and time step sizes. In these cases, the Δt and Δx must be reduced in an appropriate way permitting this ratio approximate to zero.

Stability

A numerical scheme is considered *stable* if it does not amplify the errors appearing as the numerical solution process progresses. In non-stationary problems, stability guarantees that the method has a bounded solution as long as the exact result of the equation is bounded. For example, time step smaller than a certain limit is needed by many solution methods.

Convergence

A discretization scheme is considered *convergent* if the numerical solution of the differential equations tend to the exact solution as the mesh spacing tends to zero. Convergence is normally checked by means of numerical tests, solving the equations on a series of consecutively refined grids and time steps. If the numerical method is stable and all utilized approximations are consistent, commonly it is possible to arrive to a *grid-independent-solution*. If during this numerical experiment a refined enough grid is reached, it will be noted that the rate of convergence is determined by the order of the main truncation error component.

Conservation

A numerical method is said *conservative* if the conservation equations are respected in both local and global basis. Using the strong conservation form of the transport equations, the FVM guarantees this condition for each individual control volume as well as for the whole solution domain.

Boundedness

Discretizing differential equations gives a set of algebraic equations by each nodal point in the discretized domain. These equations are generally solved by an iterative process until a convergence criteria is reached. However, not any result for the variables is valid (despite it can be mathematically correct), but it should lie within physically valid bounds. That is, in absence of sources the results for a given fluid property should be bounded by its own boundary values (*boundedness*). For example, density must be always positive, molar fraction of a specie must lie between 0 and 1, absolute temperature cannot be negative.

The requirements for guaranteeing boundedness are given in the construction of the coefficients matrix for solving the resulting algebraic equations. For example, one of them is that all the coefficients of the discretized equations should have the same sign.

Realizability

Specific models have to be applied for treating those phenomena which are complicated enough for being directly considered (such as turbulence or combustion). They must internally guarantee their *boundedness* and ability to give physically valid.

Accuracy

There are three types of errors in numerical methods: modelling errors, discretization errors, and iteration errors. All of them are the difference between exact solution of the equations and the obtained results by simulation, but referencing to different aspects of the applied model or method. Thus, the *modelling errors* are related with the actual flow and the modelled solution, the *discretization errors* refer to the exact solution of the conservation equations, and the *iteration errors* consider the distances between exact and iteratively obtained results.

Moreover, in some cases these errors may cancel each other in such a way giving better agreement with experimental results on solutions obtained using a coarser grid rather than in a finer one (which are expected to be more accurate). Therefore, this situation must be considered during grid analysis.

Transportiveness

Transportiveness is related with how a given property from one CV is transported to its neighbours. In a pure diffusive case, a transported fluid property trends to span equally in all directions, whereas in a pure convective case, the fluid property is only transported to the upstream cell. In other words, in the former situation, all

the neighbouring nodes are affected by the value of the property in the considered CV, while in the latter case, only the upstream cells are influenced.

4.1.3 Spatial discretization

Considering a generic transported fluid property ϕ, the conservative transport equation is written as,

$$\underbrace{\frac{\partial \rho\phi}{\partial t}}_{LT} + \underbrace{\nabla \cdot (\rho\phi\vec{u})}_{CT} = \underbrace{\nabla \cdot (\Gamma \nabla\phi)}_{DT} + \underbrace{S_\phi}_{ST} \tag{4.1}$$

where LT is the local term, i.e, the rate of increase of ϕ in the fluid element; CT is the convective term, i.e., the net rate of flow of ϕ out of the fluid element; DT is the diffusive term, i.e., the rate of increase of ϕ due to diffusion; and S is the source term, i.e, the rate of increase of ϕ due to other sources.

Thus, by evaluating ϕ equal to 1, $\vec{u}$, and $\hat{i}$ (or T, or $\hat{H}$) and choosing the appropriate values for the diffusion coefficients, and the source terms the mass, momentum, and energy transport equations can be respectively obtained. Even more, species and other properties transport equations can be formulated applying the same procedure.

In the FVM, transport equations are integrated in the control volume as follows:

$$\underbrace{\frac{\partial}{\partial t}\int_{CV} \rho\phi \, dV}_{LT} + \underbrace{\int_{CV} \nabla \cdot (\rho\phi\vec{u}) \, dV}_{CT} = \underbrace{\int_{CV} \nabla \cdot (\Gamma\nabla\phi) \, dV}_{DT} + \underbrace{\int_{CV} S_\phi \, dV}_{ST} \tag{4.2}$$

Applying the Gauss' theorem to the convective and diffusive terms, it is obtained

$$\frac{\partial}{\partial t}\int_{CV} \rho\phi \, dV + \int_{A} (\rho\phi\vec{u}) \cdot \check{n} \, dA = \int_{A} (\Gamma\nabla\phi) \cdot \check{n} \, dA + \int_{CV} S_\phi \, dV \tag{4.3}$$

Therefore, the first term in this equation means *the rate of change* of the total amount of fluid property ϕ. The products $(\rho\phi\vec{u}) \cdot \check{n}$ and $\check{n} \cdot \Gamma\nabla\phi$ are the normal components to the CV faces of the convective and diffusive fluxes, respectively. The former is the net rate of *decrease* of fluid property ϕ of the fluid element due to convection, whereas the latter, can be considered as a positive flux in the direction of the inward normal unitary vector $-\check{n}$, i.e., into the fluid element. Thence, the DT represents the net rate of *increase* of fluid property ϕ of the fluid element due to diffusion.

Regarding the surface integrals, the net flux through the CV boundary can be obtained as the sum of integrals over all the faces of the CV, that is,

$$\int_A \Phi_n \, dA = \sum_F \int_{A_F} \Phi_F \, dA \tag{4.4}$$

where Φ_n is the component of the total flow vector in the direction normal to the CV face,

$$\Phi_n = (\rho\phi\vec{u} - \Gamma\nabla\phi) \cdot \check{n} \tag{4.5}$$

and Φ_F is the normal component to face F of the total flow vector through this face,

$$\Phi_F = (\rho\phi\vec{u} - \Gamma\nabla\phi)_F \cdot \check{n_F} \tag{4.6}$$

In order to evaluate the surface integrals exactly, the integrand in each point of the surface A_F should be known for all CV faces. As this information is not available, it must be estimated in some way. To do this, Φ_F can be approximated either in terms of variable values at one or more points on the cell face, or in terms of CV centres.

One of the best approximations for the surface integrals is by applying the mid-point rule:

$$\Phi_F = \int_{A_F} \Phi_F \, dA = \overline{\Phi}_F A_F \approx \Phi_F A_F \tag{4.7}$$

This approximation requires that Φ_F at the center of the face F is known. Since this information is not available, it has to be estimated by interpolation.

Furthermore, the volume integrals may be estimated by replacing them by the product of the volume mean value of the integrand and the CV volume and approximate the former as the value at the cell center:

$$\int_{CV} Q \, dV = \langle Q \rangle V_{cell} \approx Q_{cc} V_{cell} \tag{4.8}$$

Therefore, introducing all the mentioned rearrangements and approximations in Equation 4.3, and considering a constant cell volume in time, the transport equation for the generic fluid property ϕ yields,

$$\frac{d}{dt}(\rho\phi)_{cc} + \frac{1}{V_{cell}} \sum_F \Phi_F A_F = S_{\phi,cc} \tag{4.9}$$

where the values at cell center are used for the volume integral approximations (indicated by the subscript cc).

4.1.4 Values at faces: the upwind differencing scheme (UDS)

As it was previously said, the approximations to the integrals involved in Equation 4.9 need the values of Φ_F. Assuming that the velocity field, ρ and Γ are known at all cell locations, to obtain the total flux of the transported fluid property ϕ, its value and gradient normal to cell face at one or more locations (depending on the approximation method applied) are required. One of the most widely used scheme is the *upwind differencing scheme (UDS)* which approximates the value of the variable at the cell face center taking into account the flow direction.

First-Order Upwind (FOU)

When applying the FOU estimation for ϕ_F, the transported value of ϕ is considered to be equal to the value at the upstream node. Mathematically,

$$\phi_F = \begin{cases} \phi_{cc} & \text{if} \quad (\vec{u} \cdot \check{n})_F > 0 \\ \\ \phi_{cc-1} & \text{if} \quad (\vec{u} \cdot \check{n})_F < 0 \end{cases} \tag{4.10}$$

where the subscript $cc-1$ refers to the cell center of the neighbouring cell sharing face F.

Since this scheme uses consistent expressions to estimate fluxes through cell faces, it is conservative. In addition, it satisfies the boundedness conditions avoiding the possibility of oscillatory solutions (particularly in stationary problems). Nevertheless, as this scheme is based on the backward differencing formula, its accuracy is only first order (based on the Taylor truncation error). Consequently, its major disadvantage is that it produces erroneous results when the flow is not aligned with the grid lines, resulting in a truncation error resembling a diffusive flux. Peaks or abrupt variations in the variables will be spread out and, as error diminishes with a rate of only first order, very fine grids are needed to achieve accurate solutions.

Second-Order Upwind (SOU) and higher order schemes

When the SOU is applied to approximate the value of ϕ_F, not only its value at the cell centroid (ϕ_{cc}) is considered, but also its gradient in the upstream cell ($\nabla\phi$),

$$\phi_F = \phi_{cc} + (\nabla\phi)_{cc} \cdot \vec{r} \tag{4.11}$$

where $\vec{r}$ is the displacement vector from the upstream cell centroid to the face centroid.

In this case, the gradient may be calculated in several ways (such as by applying the Green-Gauss theorem, or by least squares). The Green-Gauss Cell-Based method

approximates the gradient by means of the Green-Gauss theorem in the discrete form,

$$(\nabla\phi)_{cc} = \frac{1}{V_{cell}} \sum_{F} \overline{\phi}_F A_F \check{n} \tag{4.12}$$

and the value of the fluid property at the face is computed as,

$$\overline{\phi}_F = \frac{\phi_{cc} + \phi_{cc-1}}{2} \tag{4.13}$$

The SOU is less diffusive than the FOU since the truncation error corresponds to the third order in a Taylor expansion. In fact, the diffusive term in the Taylor expansion is absent, and the error decreases with the square of the cell size.

Higher order accurate interpolation schemes, like third-order upwind, Quadratic Upwind Interpolation for Convective Kinematics (QUICK), or Power Law are also available which can minimize the false diffusion errors. Though, using them makes sense only if the surface integrals are approximated using higher-order formulas. In addition, these schemes are less computationally stable, which can be seen as small over- and undershoots in the solution of some problems leading to physical unrealistic behaviours.

4.1.5 Time discretization

Similar to spatial discretization, in temporal discretization every term is integrated over a time step.

For simplicity, for a given cell in the grid, and considering zero the source term, the Equation 4.9 is rewritten as,

$$\frac{d}{dt}(\rho\phi)_{cc} = F\left(\vec{\phi}, t\right) \tag{4.14}$$

where $\vec{\phi}$ is a vector involving the value of ϕ at the center of all the cells sharing faces with the current cell, and at the current cell center.

The integration over the time step $\Delta t = t_{n+1} - t_n$ yields,

$$(\rho\phi)_{cc/n+1} - (\rho\phi)_{cc/n} = \int_{n}^{n+1} F\left(\vec{\phi}, t\right)\, dt \tag{4.15}$$

The right hand side of this equation can be integrated utilizing either the values of $F\left(\vec{\phi}, t\right)$ at the time step n, $n+1$, or a combination of both values. Generalizing,

$$(\rho\phi)_{cc/n+1} - (\rho\phi)_{cc/n} = \left[\theta F\left(\vec{\phi}, t_{n+1}\right) + (1-\theta)\, F\left(\vec{\phi}, t_n\right)\right] \Delta t \tag{4.16}$$

where θ is a weighting factor varying between 0 and 1.

Thus, if θ is 0, the explicit time discretization is obtained, whereas if it is 1, the integration results in the Euler implicit scheme. In addition, if $\theta = \frac{1}{2}$ the Crank-Nicolson scheme is derived.

As a small example for a 1D system, after working out the Equation 4.1 with all the considerations and simplifications previously mentioned, a first order upwind for spatial discretization and a fully implicit scheme (θ=1) for time, an equation (or set of equations) like the following can be obtained for each node,

$$a_i\phi_{i/n+1} + a_{i-1}\phi_{i-1/n+1} + a_{i+1/n+1} = S_{\phi/n}\Delta x + \rho\phi_{i/n}\frac{\Delta x}{\Delta t} \tag{4.17}$$

where the subscripts i, $i+1$, and $i-1$ refers to the cell node indices, n and $n+1$ to the current and next time step, respectively, a are the coefficients of the matrix for solving the equations system, and the right hand side of the equation is the independent term.

4.2 Multi-fluid hydrodynamic model

In the present work the Euler-Euler approach was applied for describing the hydrodynamics of multi-phase flow in the fluidized bed. In this approach the different phases are treated mathematically as interpenetrating continuum in the same control volume, sharing the same pressure. As a phase cannot occupy the same volume than another one, it is applied the concept of phase volumetric fraction (considering it continuous in space and time), and conservation equations are derived for each phase. Moreover, the interaction betweens phases are coupled through interphase exchange coefficients and the pressure, and properties of solid phases and interactions between them are obtained by means of the Kinetic Theory of Granular Flow (KTGF).

4.2.1 Conservation equations

Continuity

For a given phase i the conservation of mass is

$$\frac{\partial}{\partial t}\left(\alpha_i\rho_i\right) + \nabla\cdot\left(\alpha_i\rho_i\vec{u}_i\right) = \sum_{j=1}^{n_{ph}}\left(\dot{m}_{ji} - \dot{m}_{ij}\right) + S_i \tag{4.18}$$

where $\dot{m}_{ji}$ and $\dot{m}_{ij}$ are the mass transfer between phases, and S_i is a source term.

Momentum

For a given fluid phase f the momentum balance yields

$$\begin{aligned}\frac{\partial}{\partial t}\left(\alpha_f \rho_f \vec{u}_f\right) + \nabla \cdot \left(\alpha_f \rho_f \vec{u}_f \vec{u}_f\right) = \\ -\alpha_f \nabla P + \nabla \cdot \bar{\bar{\tau}}_f + \alpha_f \rho_f \vec{g} + \\ \sum_{j=1}^{n_{ph}} \left(\vec{R}_{jf} + \dot{m}_{jf}\vec{u}_{jf} - \dot{m}_{fj}\vec{u}_{fj}\right) + \\ \left(\vec{F}_f + \vec{F}_{lift,f} + \vec{F}_{vm,f}\right)\end{aligned} \tag{4.19}$$

where P is the pressure shared by all phases, $\bar{\bar{\tau}}_f$ is the phase stress-strain tensor (calculated as indicated in ANSYS Fluent 13 Theory Guide 2010), $\vec{F}_f$, $\vec{F}_{lift,f}$, and $\vec{F}_{vm,f}$ are, respectively, the external body force, lift force, and virtual-mass force (usually neglected in fluidized bed since they are insignificant compared with drag forces), and $\vec{R}_{jf}$ is the momentum exchange between phases,

$$\vec{R}_{jf} = K_{jf}\left(\vec{u}_j - \vec{u}_f\right) \tag{4.20}$$

here $\vec{R}_{jf} = -\vec{R}_{fj}$, and the momentum exchange coefficient $K_{jf} = K_{fj}$

In addition, $\vec{u}_{fj}$ is the interphase velocity whose value depends upon the mass transfer between phases. That is., if $\dot{m}_{fj} > 0$, $\vec{u}_{fj} = \vec{u}_f$, and if $\dot{m}_{fj} < 0$, then $\vec{u}_{fj} = \vec{u}_j$.

On the other hand, for a given solid phase p the momentum balance is as follows

$$\begin{aligned}\frac{\partial}{\partial t}\left(\alpha_p \rho_p \vec{u}_p\right) + \nabla \cdot \left(\alpha_p \rho_p \vec{u}_p \vec{u}_p\right) = \\ -\alpha_p \nabla P - \nabla P_p + \nabla \cdot \bar{\bar{\tau}}_p + \alpha_p \rho_p \vec{g} + \\ \sum_{j=1}^{n_{ph}} \left(\vec{R}_{jp} + \dot{m}_{jp}\vec{u}_{jp} - \dot{m}_{pj}\vec{u}_{pj}\right) + \\ \left(\vec{F}_p + \vec{F}_{lift,p} + \vec{F}_{vm,p}\right)\end{aligned} \tag{4.21}$$

4.2.2 Definition of Reynolds numbers

In the following sections and subsections different Reynolds numbers will be used, depending on whether they are based on superficial velocity magnitude or relative velocity between phases, or employing either a generic, spheric, volumetric, or

Sauter's diameter. Therefore, it is better to define in this subsection the utilized nomenclature for Reynolds definition. In general terms, the Reynolds number is

$$Re_{dd_{sup}} = \frac{\rho_f \| velocity \| d_{dd}}{\mu_f} \tag{4.22}$$

Where one or two subscripts may be used. When *sup* appears, the superficial velocity magnitude is employed, whereas if it is omitted, the magnitude of the relative velocity between phases ($\|\vec{u}_f - \vec{u}_p\|$) is applied. Regarding to *dd*, it varies according to the type of diameter used:
- V: diameter of a sphere having the same volume than the particle.
- SV: Sauter's diameter.
- P: diameter of a sphere, when the equation is valid only for spheres.
- p: generic diameter of the disperse phase.

It is more than obvious that the same nomenclature is valid for denoting particle diameter even if this variable is used in other equation than Reynolds number.

Moreover, the subscript *mf* can be used instead of *sup* for denoting the magnitude of the superficial minimum fluidization velocity.

4.2.3 Ergun's equation and minimum fluidization velocity

The Ergun's equation (Ergun, 1952) is used not only for calculating the minimum fluidization velocity, but also constitutes the basis of some drag models hereafter described. This empirical correlation was developed in order to calculate the unrecoverable pressure drop through packed beds of identical particles. In 1900 O. Reynolds proposed a formulation for the resistance offered by a fluid flowing through a packed bed as the sum of two terms; one proportional to superficial velocity, and the other one proportional to the fluid density and the squared velocity. Working out this equation in the limits of zero and infinite velocity, and comparing these expressions with the Darcy's law, Ergun obtained that the linear term in the Reynolds' formulation is proportional to fluid viscosity. Also, based on other works he included fluid volumetric fraction (called void fraction) and particle Sauter's diameter (using specific superficial area, particle area/volume) in the two terms of the original formulation, obtaining thus, a viscous term and a kinetic term. That is:

$$\frac{\Delta P}{L} = k_1 \frac{(1-\alpha_f)^2}{\alpha_f^3} \frac{\mu_f u_{sup}}{d_{SV}^2} + k_2 \frac{(1-\alpha_f)}{\alpha_f^3} \frac{\rho_f u_{sup}^2}{d_{SV}} \tag{4.23}$$

rearranging, and grouping,

$$\frac{\Delta P}{L} \frac{d_{SV}^2}{\mu_f u_{sup}} \frac{\alpha_f^3}{(1-\alpha_f)^2} = k_1 + k_2 \frac{Re_{SV_{sup}}}{(1-\alpha_f)} \tag{4.24}$$

Therefore correlating the left side of Equation 4.24 with $Re_{SV_{sup}}/(1-\alpha_f)$ for 640 experimental points, Ergun obtained a straight line, and then could estimate k_1 and k_2. Thus, he obtained:

$$\frac{\Delta P}{L} = 150\frac{(1-\alpha_f)^2}{\alpha_f^3}\frac{\mu_f u_{sup}}{d_{SV}^2} + 1.75\frac{(1-\alpha_f)}{\alpha_f^3}\frac{\rho_f u_{sup}^2}{d_{SV}} \tag{4.25}$$

On the other hand, the minimum fluidization velocity can be calculated evaluating this equation at the onset of fluidization. Under this condition, the bed is still packed but the pressure drop multiplied by bed superficial area is equal to the weight of contained material and fluid. In other words,

$$\frac{\Delta P}{L} = (1-\alpha_{f_{mf}})(\rho_p - \rho_f)g \tag{4.26}$$

Then, combining it with Equation 4.25, replacing d_{SV} with ψd_V (being *psi* the particle shape factor), and working out the resulting expression, it possible to obtain

$$\frac{(\rho_p - \rho_f)\rho_f g d_V^3}{\mu_f^2} = 150\frac{(1-\alpha_{f_{mf}})}{\alpha_{f_{mf}}^3}\frac{1}{\psi^2}\frac{\rho_f u_{mf} d_V}{\mu_f} + 1.75\frac{1}{\alpha^3}\frac{1}{\psi}\left(\frac{\rho_f u_{mf} d_V}{\mu_f}\right)^2 \tag{4.27}$$

4.2.4 Drag models

Many authors have tested different drag models evaluating their prediction capabilities comparing pressure drop, solids profiles after a certain simulation time, or bed expansion, with experimental results. Loha *et al.* (2012) studied the effect of different drag models (Syamlal-O'Brien, Gidaspow, EMMS, and McKeen) on the hydrodynamic behaviour of a bubbling fluidized bed, using 530 µm diameter particles. This effect was analysed evaluating the vertical and horizontal time-averaged solid profiles (in particular the ability of forming a core-annulus horizontal profile), and the time-averaged velocity profiles of solid phase. They found that velocity and solid profiles could be quite accurately predicted applying Gidaspow drag model. In addition, acceptable predictions of the core-annulus behaviour could be obtained when Gidaspow as well as Syaamlal drag models were utilized.

Compared with experimental information, they found that very accurate velocity profile and quite good solid profiles where predicted when Gidaspow drag model was applied, and the core-annulus behaviour could be accurately predicted by applying Gidaspow as well as Syaamlal drag models.

On the other hand, Vejahati *et al.* (2009) performed 2D simulations of fluidized beds containing particles of diameters between 230 µm and 300 µm, and 2500 kg/m^3 of density. They compared different drag models (Wen and Yu, Gidaspow, Di Felice, Syamlal and O'Brien, and other three) with experimental information in terms of

the prediction of bed expansion and pressure drop when each model was applied. Moreover, they adjusted the Di Felice and the Syamlal and O'Brien models with a method based on minimum fluidization velocity. In general, the authors did not find significant differences among simulations done with different drag models for predicting pressure drop at low air velocities (less than $7u_{mf}$). Nevertheless, except when the adjusted models were applied, the bed expansion was under-estimated in every simulated cases. Esmaili and Mahinpey (2011) extended the mentioned work to a 3D grid, finding that the best bed expansion was predicted by the adjusted Di Felice drag model. Furthermore, they concluded that although 3D simulation is more computational-time expensive and requires more calculus power, their results are more accurate.

In the present work the performance of three drag models was tested by means of determining the minimum fluidization velocity of powders by means of simulation. Gidaspow, Wen and Yu, and Mazzei and Lettieri models were examined: the first two models are included among the models in ANSYS(R) Fluent, whereas the third one was implemented through User Defined Funtion. In the following paragraphs the tested models and their fundamentals will be described.

Wen and Yu's drag model

Wen and Yu (1966) proposed a model based on the premise that in a multiparticle system the drag forces acting on the particles are affected by the fluid volumetric fraction within the bed. In this model the drag force acting on a constituent particle of a suspension is calculated as the drag force acting on an isolated particle multiplied by a correction factor, the voidage function.

Thus, in the equilibrium, the Newton's second law applied to a particle in a suspension gives

$$F_D + F_E - \rho_p V_P g = 0 \tag{4.28}$$

defining the voidage function as

$$f(\alpha_f) = \frac{F_D}{F_{Ds}} \tag{4.29}$$

combining and rearranging

$$f(\alpha_f) F_{Ds} = (\rho_p - \rho_f) g V_P \tag{4.30}$$

Considering the definition of drag force as

$$F_{Ds} = C_{Ds} \frac{1}{2} A_{pu} \rho_f u_{sup}^2 \tag{4.31}$$

using the drag correlation for a single particle of Schiller and Naumann (taken by the authors for its validity in all flow regimes),

$$C_{Ds} = \begin{cases} \dfrac{24}{Re_{P_{sup}}}\left(1 + 0.15Re_{P_{sup}}^{0.687}\right) & Re_{P_{sup}} \leq 1000 \\ \\ 0.44 & Re_{P_{sup}} > 1000 \end{cases} \tag{4.32}$$

and solving for a sphere for $Re_{P_{sup}} \leq 1000$, it is obtained

$$F_{Ds} = \pi d_P^2 \rho_f u_{sup}^2 (3Re_{P_{sup}}^{-1} + 0.45Re_{P_{sup}}^{-0.313}) \tag{4.33}$$

then, substituting Equation 4.33 into 4.30, multiplying both sides by $6\rho_f/\mu_f^2$, and rearranging it is possible to obtain the following expression

$$f(\alpha_f) = \frac{Ar}{18Re_{P_{sup}} + 2.7Re_{P_{sup}}^{1.687}} \tag{4.34}$$

where

$$Ar_P = \frac{(\rho_p - \rho_f)\rho_f g d_P^3}{\mu_f^2} \tag{4.35}$$

Plotting experimental data in terms of voidage function versus void fraction in log-log scale, Wen and Yu obtained a straight line whose slope is -4.7. Hence, they concluded that the voidage function has the following form:

$$f(\alpha_f) = \alpha_f^{-4.7} \tag{4.36}$$

and the drag force acting on a constituent particle of a homogeneous suspension can be expressed as

$$F_D = F_{Ds}\alpha_f^{-4.7} \tag{4.37}$$

therefore, the drag coefficient is

$$C_D = C_{Ds}\alpha_f^{-4.7} \tag{4.38}$$

On the other hand, by plotting $\alpha_f^{4.7} Ar_P$ as a function of Reynolds number, and comparing it with experimental data, the authors found a deviation of ± 10 % and a validity for a Reynolds number up to 1000. In addition, using a mean fluid volumetric fraction for spheres at the onset of fluidization ($\alpha_{f_{mf}}$=0.42) they arrived to

$$Ar_P = 1060Re_{P_{mf}} + 159Re_{P_{mf}}^{1.687} \tag{4.39}$$

In order to verify the validity of their correlation, Wen and Yu compared Equation 4.39 with the minimum fluidization velocity that can be calculated evaluating Ergun's equation at the onset of fluidization (Equation 4.27),

$$\underbrace{\frac{(\rho_p - \rho_f)\rho_f g d_V^3}{\mu_f^2}}_{Ar_V} = 150 \underbrace{\frac{(1-\alpha_{f_{mf}})}{\alpha_{f_{mf}}^3}\frac{1}{\psi^2}}_{A}\underbrace{\frac{\rho_f u_{mf} d_V}{\mu_f}}_{Re_{V_{mf}}} + 1.75 \underbrace{\frac{1}{\alpha^3}\frac{1}{\psi}}_{B}\underbrace{\left(\frac{\rho_f u_{mf} d_V}{\mu_f}\right)^2}_{Re_{V_{mf}}^2}$$

Correlating it with 134 experimental data, Wen and Yu obtained A=11 and B=14, and a new expression for calculating the minimum fluidization velocity based on Ergn's equation:

$$Ar_V = 1650 Re_{V_{mf}} + 24.5 Re_{V_{mf}}^2 \tag{4.40}$$

Then, the authors found a standard deviation of 34 % and mean deviation of ± 25 % based on 234 data points, covering a $Re_{V_{mf}}$ between 0.001 and 4000. Moreover, they verified that the values of the coefficients of both terms in Equation 4.40 are similar to those present in Equation 4.39 when applied only to spheres.

Momentum exchange coefficient based on Wen and Yu's equations

Considering a homogeneous suspension and a fixed observer on the particles (i.e, not moving with respect to them), the following relationships can be applied:

$$\vec{u}_f = \frac{\vec{u}_{sup}}{\alpha_f} \quad \vec{u}_p = \vec{0} \quad \|\vec{u}_f - \vec{u}_p\| = \frac{u_{sup}}{\alpha_f}$$

then

$$u_{sup} = \alpha_f \|\vec{u}_f - \vec{u}_p\| \tag{4.41}$$

The Reynolds number based on superficial velocity for a given diameter of the disperse phase "p" is redefined as follows

$$Re_{p_{sup}} = \frac{\rho_f d_p \alpha_f \|\vec{u}_f - \vec{u}_p\|}{\mu_f} \tag{4.42}$$

that is

$$Re_{p_{sup}} = \alpha_f Re_p \tag{4.43}$$

Summarizing, on the basis of the Schiller and Naumann drag correlation for a single particle in a suspension employed by Wen and Yu and their voidage function,

and replacing the Reynolds number with its previously mentioned redefinition, the following drag equation can be written for a spherical particle:

$$C_{Ds} = \frac{3}{Re_P \alpha_f}\left(1 + 0.15(Re_P \alpha_f)^{0.687}\right) \tag{4.44}$$

therefore, combining Equations 4.31, 4.37, and 4.41 the drag force acting on a constituent spherical particle of a multiparticle system is

$$F_D = \frac{\pi}{8} d_P^2 \rho_f \|\vec{u}_f - \vec{u}_p\|^2 C_{Ds} \alpha_f^{-2.7} \tag{4.45}$$

By multiplying by the number of particles in the phase per unit of total volume,

$$n_P = \frac{\alpha_p}{V_P} \tag{4.46}$$

this force can be extended to the entire disperse phase. In addition, rewriting F_D in the vectorial form, the drag force per unit of total volume is obtained. That is,

$$n_P \vec{F}_D = \frac{3}{4} \frac{\rho_f \alpha_p \|\vec{u}_f - \vec{u}_p\|}{d_P} C_{Ds} \alpha_f^{-2.7} (\vec{u}_f - \vec{u}_p) \tag{4.47}$$

then, if this drag force is multiplied by the fluid volumetric fraction in order to be consistent with the multi-fluid model, it can be compared with the drag exchange between fluid and disperse phases

$$\vec{R}_{fp} = K_{fp}(\vec{u}_f - \vec{u}_p) \tag{4.48}$$

hence, the momentum exchange coefficient using the Wen and Yu's voidage function is

$$K_{fp} = \frac{3}{4} \frac{\rho_f \alpha_f \alpha_p \|\vec{u}_f - \vec{u}_p\|}{d_P} C_{Ds} \alpha_f^{-2.7} \tag{4.49}$$

where C_{Ds} is calculated with Schiller and Naumann correlation (Equation 4.44).

ANSYS(R) Fluent implements the Wen and Yu based momentum exchange coefficient with a slight modification: instead of using Wen and Yu's voidage function, it applies the one found by Richardson and Zaki for terminal Reynolds number less than 0.2. Thence, momentum exchange coefficient based on the Wen and Yu's work is calculated by Fluent as follows:

$$K_{fp} = \frac{3}{4} \frac{\alpha_p \alpha_f \rho_f \|\vec{u}_f - \vec{u}_p\|}{d_P} C_{Ds} \alpha_f^{-2.65} \tag{4.50}$$

where

$$C_{Ds} = \frac{24}{\alpha_f Re_P}\left(1 + 0.15(\alpha_f Re_P)^{0.687}\right) \tag{4.51}$$

Gidaspow's momentum exchange coefficient

Gidaspow (1986) suggested the application of a momentum exchange coefficient as a combination of Ergun's equation and Wen and Yu based coefficient depending on the fluid volumetric fraction. Moreover, he adapted Ergun's equation in order to be applied in the hydrodynamic model employed by means of the following simple steps. By comparing the gas momentum balance (with no acceleration and negligible acceleration gravity),

$$0 = -\alpha_f \frac{\partial P}{\partial y} + K_{pf}(u_{p_y} - u_{f_y}) \tag{4.52}$$

and the Ergun's equation (Equation 4.25 in combination with Equation 4.41), it can be obtained a momentum exchange coefficient applicable for α_f less than 0.8. Summarizing, the Gidaspow's model for a sphere is the following:

$$K_{fp} = \begin{cases} 150\dfrac{\alpha_p^2}{\alpha_f}\dfrac{\mu_f}{d_P^2} + 1.75\dfrac{\alpha_p \|\vec{u}_f - \vec{u}_p\|\rho_f}{d_P} & \text{if } \alpha_f < 0.8 \\ \\ \dfrac{3}{4}\dfrac{\alpha_p \alpha_f \rho_f \|\vec{u}_f - \vec{u}_p\|}{d_P} C_{Ds}\alpha_f^{-2.65} & \text{if } \alpha_f \geq 0.8 \end{cases} \tag{4.53}$$

where C_{Ds} is calculated with Schiller and Naumann's correlation (Equation 4.44).

Mazzei and Lettieri's momentum exchange coefficient

Mazzei and Lettieri (2007) developed a momentum exchange coefficient for fluidized systems of uniformly dispersed spherical particles based on the empirical correlation of Richardson and Zaki for bed expansion,

$$\frac{u_t}{u_{sup}} = \alpha_f^{-n} \tag{4.54}$$

and Dallavalle's correlation for drag coefficient of a single particle. They found an expression consistent with Richardson and Zaki correlation and valid for all fluid dynamic regimes, and any value of fluid volumetric fraction.

$$K_{pf} = \frac{\alpha_f \rho_f \|\vec{u}_f - \vec{u}_p\| \alpha_p}{d_P} \frac{3}{4} C_{Ds} \phi_{ML} \tag{4.55}$$

where

$$\phi_{ML} = \frac{C_{Ds}^*}{C_{Ds}} \alpha_f^{2(1-n)} \tag{4.56}$$

being, respectively, C_{Ds} and C^*_{Ds}, the particle drag and terminal drag coefficient, calculated with Dallavalle's correlation

$$C_{Ds} = \left(0.63 + 4.8(\alpha_f Re_P)^{-0.5}\right)^2 \tag{4.57}$$

$$C^*_{Ds} = \left(0.63 + 4.8(Re^*_P)^{-0.5}\right)^2 \tag{4.58}$$

n the Richardson and Zaki exponent

$$n = \frac{4.8 + 0.42{Re^*_P}^{0.75}}{1 + 0.175{Re^*_P}^{0.75}} \tag{4.59}$$

and the Reynolds number redefined as

$$Re^*_P = \frac{Re_P}{\alpha_f^{n-1}} \tag{4.60}$$

It is worthy to point out that the works of Wen and Yu, and Mazzei and Lettieri are based on non-cohesive expansed fluidized beds, whereas the Ergun's work is based on packed beds. In other words, while the voidage function obtained by Wen and Yu is comparable with the Richardson and Zaki correlation (Equation 4.54), and Mazzei and Lettieri's corrective factor is consistent with this correlation, the Ergun's equation is based only on pressure drop through a packed bed.

4.2.5 Kinetic Theory of Granular Flow (KTGF)

In a few words, the KTGF is an adaptation of the classical theory of non-uniform dense gases to granular flows, by making an analogy between the random motion of particles and the thermal motion of molecules in a gas. Therefore, equations accounting for the energy associated with fluctuation motion of particles are used for depicting how the solid phase behaves.

In similar manner that thermodynamic temperature is associated with the kinetic energy of a gas (translational, rotational, or vibrational), the KTGF defines the granular temperature which accounts for the particle random motion. This model considers that the solid viscosity and stress are function of the granular temperature, which in turn is a function of time and space.

Thus, the transport equation derived from this theory is:

$$\frac{3}{2}\left[\frac{\partial}{\partial t}\left(\rho_p \alpha_p \Theta_p\right) + \nabla \cdot \left(\rho_p \alpha_p \vec{u}_p \Theta_p\right)\right] = \left(-P_p \overline{\overline{I}} + \overline{\overline{\tau}}_p\right) : \nabla \vec{u}_p + \nabla \cdot \left(k_{\Theta p} \nabla \Theta_p\right) - \gamma_\Theta + \phi_{fp} \tag{4.61}$$

where

Θ_p is the granular temperature, $\left(-P_p\overline{\overline{I}} + \overline{\overline{\tau}}_p\right) : \nabla\vec{u}_p$ is the generation of energy by the solid stress tensor; $\nabla \cdot (k_{\Theta p}\nabla\Theta_p)$ is the conduction due to gradient of granular temperature; ($k_{\Theta p}$ is the diffusion coefficient); γ_Θ is the collisional dissipation of energy, and ϕ_{fp} is the energy exchange between the f^{th} fluid (or solid) phase and the p^{th} solid phase.

In the calculation of the right hand terms are involved the restitution coefficient (which is the ratio of speeds of two particles after and before an impact) and the radial distribution function ($g_{0,pp}$). This function takes into in account the increment on the number of collisions when the solids volumetric fraction approximates to a maximum value ($\alpha_{p,max}$, the maximum packing limit) for an arrangement of spherical particles. Depending on the adopted model (for mixtures or single solid phase), these particles may be either with the same or different diameter.

Further information about the basis of the KGTF and its applications can be found in Gidaspow (1994), Gidaspow *et al.* (2004), Jiradilok *et al.* (2006), Jung *et al.* (2006), Patiño-Palacios *et al.* (2010), Asegehegn *et al.* (2012), and other related literature. In the present work the KGTF was applied as it was described in the ANSYS(R) Fluent 13 Theory Guide (2010).

Part II

Materials and Methods

Chapter 5

Experimental setup and determinations

5.1 Adsorbent characterization

5.1.1 Minimum fluidization velocity

Wheat bran purchased in the local market was fluidized in the L35b fluidized bed described in Section 5.3 in order to measure its minimum fluidization velocity. The air flow rate was varied from 25 to 100 m^3/h (0.05 to 0.28 m/s, after normalization), and pressure drops were measured.

5.1.2 Density and maximum water content

Bran absolute density was measured by means of a BET equipment in nitrogen picnometer modality (Micromeritics ASAP 2010). In this technique, after removing the air present in a test tube the volume occupied by nitrogen is measured. Then a small quantity of bran is poured in the tube, and dried under vacuum during one day. Once the adsorbent is completely dried, nitrogen is injected again and its volume is measured. Finally the adsorbent volume is calculated as the difference between the volumes occupied by nitrogen in the test tube without and with the material. Thus the weight of the material in the test tube, and its volume suffice for the determination of the adsorbent absolute density. In addition, the measurement precision is: 5×10^{-5} cm^3 for volume and 5×10^{-5} g for weight. Moreover, bran bulk density was determined by simply filling a 40 mL beaker with bran and weighting it.

On the other hand, the maximum water content of bran, defined as the maximum mass of water that the adsorbent can retain (considering the particle surface as well as internal pores) per unit of mass of dried material, was calculated saturating a

certain amount of bran in water and calculating the weight difference between wet material and dried material. That is, after weighting a volume of 40 mL (V_{beaker}) of bran inside of a beaker (m_A) first, it was filled with water up to fill the 40 mL of bran, and weighted again (m_{w+A}). Once the bran was completely wet and practically immersed under water (always paying particular attention to not exceed the 40 mL of volume), the remaining water was poured into another beaker, and the first beaker containing only wet solid was weighted (m_{A-hum}). Finally, the following equations were used to obtain the maximum water content and water weight fraction of wet solid (C_w and w_w, respectively):

$$m_w = m_{w+A} - m_A \tag{5.1}$$

$$\rho_b = \frac{m_A}{V_{beaker}} \tag{5.2}$$

$$C_w = \frac{m_{w-hum}}{m_A} \tag{5.3}$$

$$w_w = \frac{m_{A-hum} - m_A}{m_{A-hum}} \tag{5.4}$$

The previous procedure was repeated five times for statistical purposes, and confidence intervals (CI) were calculated with 95 % of confidence.

5.1.3 Particle size distribution and equivalent diameters

Particle size distribution:

Bran particle size distribution was obtained by means of shaking the samples in sieves for about 4 hours, using an ATSM sieves set. In order to check the reproducibility, two samples were sieved. With this method, only the mesh-diameter distribution was obtained (surface diameter). Since bran particles have planar shape, particle thickness was obtained by means of a photographic method. It consisted in placing the particles perpendicular to a piece of graph paper, holding them with forceps, and photographing them with a digital photo-camera. After that, the photos were analysed by means of a graphic software, measuring the length in pixels of one millimetre marked in the graph paper. Then, it was measured the thickness of bran particles in pixels, and finally, this last value was converted to millimetres.

In order to roughly estimate the particle distribution in terms of minimum fluidization velocity and Geldart's classification of each class, Sauter diameter, shape factor and volumetric diameter were calculated, assuming particles with circular shape and diameter equal to mesh-diameter. The minimum fluidization velocity was calculated applying Ergun's equation.

Equivalent diameter for fluidization (EDF)

For simulation purposes not only information about density is necessary, but also an estimation of an equivalent diameter for fluidization, as well as the maximum packaging limit. For calculating the EDF the Ergun's equation with Wen and Yu constants was adopted applying the constants proposed by Wen and Yu for shape and porosity.

Therefore, working out Equation 4.40 the following expression is obtained:

$$\rho_A = \frac{1650 u_{mf} \mu_{ai}}{g} \frac{1}{d_{eq}^2} + \frac{24.5 u_{mf}^2 \rho_{ai}}{g} \frac{1}{d_{eq}} + \rho_{ai} \ , \tag{5.5}$$

and solving this equation with bran bulk density, experimental minimum fluidization velocity, $\rho_{ai} = 1.225$ kg/m^3, and μ_{ai}=1.7894.10^{-5} Pa s, the EDF (d_{eq}) was obtained.

In addition, the bran maximum packing limit was determined as the relation between bulk density and absolute density. That is:

$$\alpha_{A,max} = \frac{\rho_b}{\rho_{abs}} \ . \tag{5.6}$$

5.2 Food materials characterization

Fresh food material was purchased in the local market, and cut in pieces as regular as possible when it was necessary, such as discs or slabs (dimensions are described in Table 8.3 together with results). Lyophilized material was obtained by vacuum freeze drying in a small-size industrial apparatus (*LyoBeta 25*^{TM} by Telstar, Terrassa, Spain), using the same conditions for every food material (Table 5.1). Furthermore, food particle geometrical characteristics, density, and maximum packaging limit were measured applying different methods. For further references the following codes for food material were assigned[1]:

- *CAf*: fresh carrot
- *CAa and CAb*: lyophilized carrot
- *POa and POd*: lyophilized potato
- *POb and POc*: fresh potato
- *PEa and PEc*: lyophilized pea
- *PEb*: partially-lyophilized pea
- *PEf*: fresh pea

[1]Different codes were assigned to materials with different dimensions or purchased in separated dates.

Particle volumes and superficial areas were calculated using the mean of their linear dimensions (diameter, thick, etc), and applying the corresponding formulas according to their shape. In addition, particle specific area, needed in simulation when heat and mass transfer processes are involved, was obtained by its definition, that is, the ratio particle area to its volume.

Equivalent sphere diameters and shape factors were calculated applying equations 5.7, 5.8, and 5.9. Sauter diameter and sphericity are of particular interest, since the former was used for drag coefficient calculations in CFD simulations, and the latter property was taken into account for analysis in segregation experiments.

$$d_S = \left(\frac{S_P}{\pi}\right)^{\frac{1}{2}} \tag{5.7}$$

$$d_V = \left(\frac{6V_P}{\pi}\right)^{\frac{1}{3}} \tag{5.8}$$

$$\psi = \left(\frac{d_V}{d_S}\right)^{2} \tag{5.9}$$

On the other hand, fresh product density was calculated by means of picnometric techniques whereas lyophilized material densities were obtained deducting the evaporated water from the fresh product values, assuming negligible shrinkage. That is,

$$\rho_{P_{lyo}} = \rho_{P_{fresh}} \frac{m_{P1}}{m_{P0}} \tag{5.10}$$

As it was previously said for bran, maximum packaging limit of food is required as well for simulation proposes. However, since food particles are appreciably greater than adsorbent ones, this property was estimated with a different method: a 40 mL beaker was filled with food particles, and weighted. Then, the maximum packaging limit was obtained as follows:

$$\alpha_{P,max} = \frac{m_P}{\rho_P V_{baker}} \tag{5.11}$$

Table 5.1: Cycle conditions used for food lyophilization.

Code	Material code	Freezing T (°C), t (h)	Press. P (Pa)	Primary drying T (°C), P (Pa), t (h)	Secundary drying T (°C), P (Pa), t (h)
LY01	CAb	-50,16	10	-5, 10, 15.0	25, 10, 24.0
LY02	PEc	-50,16	10	-5, 10, 13.8	25, 10, 30.3
				-5, 20, 18.2	

5.3 Experimental fluidized beds

According to the characteristics of each performed test, different fluidized beds were utilized. Experiments for the first simulation verifications were carried out in a small fluidized bed (L13b) allowing to run rapid simulations using small grids, whereas segregation experiments were done in a fluidized bed (L35b) as well as in a spout-fluid bed (L20spjet) recording them with a photographic camera set in video mode for later analysis. Moreover, an intermediate size fluidized bed (L20b) was used particularly in part of channelling description.

5.3.1 35 cm sided bubbling fluidized bed (L35b)

In this apparatus air is injected into the bed via a gas distributor consisting of a squared perforated plate of 35x35 cm (Figure 5.1). The air flow is measured with a graduated flow-meter, and converted into N m^3/h applying a calibration curve which considers atmospheric pressure, air temperature, and characteristics of the flow-meter. Moreover, pressure drop is measured by means of a water manometer opened to the atmosphere, whose lowest pressure transducer is placed 11.5 cm above the bed bottom.

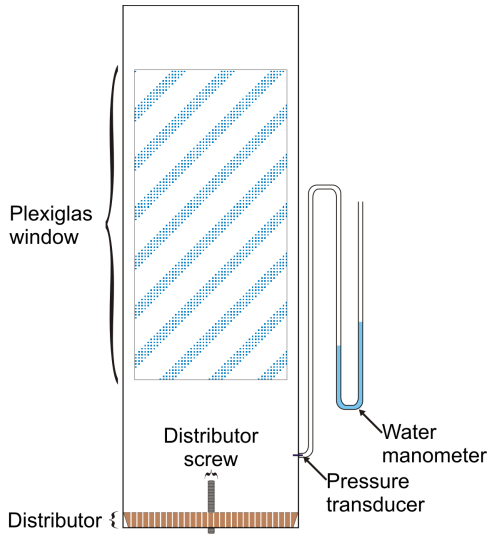

Figure 5.1: 35 cm sided fluidized bed.

5.3.2 13 cm sided bubbling fluidized bed (L13b)

In this apparatus air is injected into the bed via a gas distributor consisting of a squared perforated plate of 13x13 cm. In addition, it posses one wall completely

made of plexiglass, allowing to observe the material inside and its fluidization.

5.3.3 20 cm sized bubbling fluidized bed (L20b)

In this apparatus air is injected into the bed via a gas distributor consisting of a squared perforated plate of 20x20 cm (Figure 5.2). In addition, it posses one wall completely made of plexiglass, allowing to observe the material inside and its fluidization.

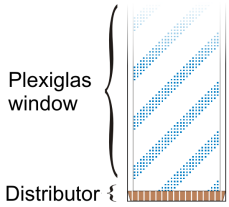

Figure 5.2: 20 cm sided fluidized bed.

5.3.4 Modified jet-spouted bed (L20spjet)(spout-fluid bed)

The hybrid spouted bed has (also called "spout-fluid bed"), in addition to its central air jet, lateral air injectors in the bed bottom (Figure 5.3). These injectors avoids the accumulation of bigger material in the bed bottom.

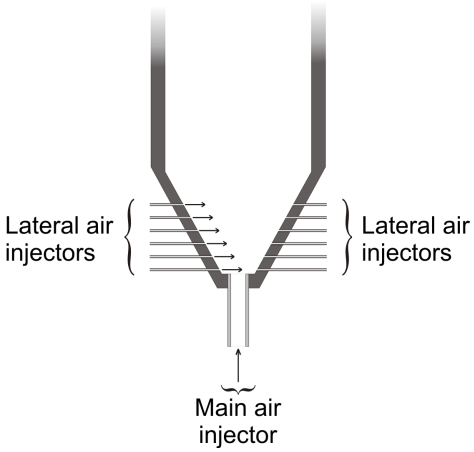

Figure 5.3: 20 cm hybrid spouted bed.

5.4 Further analysis on bran fluidization behaviour

5.4.1 Channeling analysis

Aiming to obtain a qualitative description and quantitative data about the behaviour of a binary mixture in the 35 cm sided fluidized bed, videos were taken while doing fluidization experiments, through a plexiglass window placed on the upper part of the bed. Then, these videos were analysed frame by frame and information about bed height, number of frontal channels, and variation of these variables during the fluidization at different velocities was taken.

To get the qualitative information, first of all, frontal bed height was measured every about 5 seconds, and mean frontal bed height was calculated. Then, an horizontal line for channels counting was defined at l_{mc}=0.88, where:

$$l_{mc} = \frac{h_{mc}}{\overline{h}_{bed}} \tag{5.12}$$

The number of frontal channels was counted at h_{mc}, assuming that what is happening at the front is in somehow a representation of what it is taking place in the rest of the fluidized bed. By visual inspection, this can be considered valid for velocities at least u>1.7u_{mfA}.

Another series of three experiments was performed in the L20b fluidized bed using a binary mixture of lyophilized carrots and bran. During the fluidization, videos were taken through bed plexiglass frontal wall for frame by frame analysis. These experiments were done at three air superficial velocities, 1.7 u/u_{mfA}, 2.2 u/u_{mfA}, and 2.6 u/u_{mfA}, with the scope of obtaining a general idea about the behaviour of channels formation and solid phases interaction. Although there would be some differences concerning to channels length, or their diameters between a 35 cm sided and 20 cm sided fluidized beds, the main idea was to better observe the channelling phenomenology already seen in the upper part of the 35 cm sided bed.

5.4.2 Pressure drop

Scoping to measure the pressure drop during channel generation and collapse of wheat bran in a fluidized bed, experiments in a small 6.5 cm diameter cylindrical bed were carried out (Figure 5.4, *L065b* for further references). For this purpose the bed was filled with 160 g of bran, air velocities ranging between 0.46 and 1.26 m/s were utilized, and pressure was measured using a water manometer. The small diameter of the fluidized bed was particularly chosen since it allows the formation of only one channel with the used wheat bran.

In order to obtain better information of the variations of the pressure drop during the channels formation and collapse, videos were taken during the experimentation,

for further frame by frame analysis.

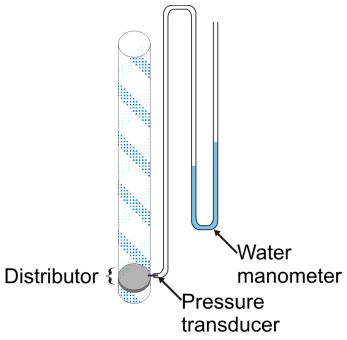

Figure 5.4: 6.5 cm diameter fluidized bed (L065b).

5.5 Mixing and segregation

5.5.1 A novel way for evaluating segregation: The Three Thirds Segregation Indexes Set

As it was previously mentioned in Section 3.5.1, the presented segregation indexes do not describe the shape of the segregation profile. In addition, according to the results of the tests described in Section 10.1 they sometimes give not completely accurate results in particular when central segregation is present or the number of experimental layers varies for exactly the same segregation pattern.

Therefore, instead of using only one quantity to evaluate segregation, it is proposed a new set of indexes, synthetically measuring the distribution of the material of interest along the bed and the segregation level. Thus, when getting a general idea by comparison of two or more experiments is intended, the first value to be considered is the segregation level, while if the intention is to observe the influence of certain variable on the segregation profile, the variation of the whole set of indexes should be taken into account.

Consequently, the Three Thirds Segregation Set of Indexes (TTSIS) is defined as:

$$TTSIS = [p_I, p_M, p_S]_{\aleph_2} \tag{5.13}$$

where p_I is the Bottom Third Indicator, p_M is the Middle Third Indicator, p_S is the Top Third Indicator, and $\aleph_2$ is the Segregation Level. Defining $F_q(h^*)$ as the accumulated mass of material of interest "q" in function of dimensionless bed height

from the bottom (h^*), these three indicators are calculated as follows:

$$p_I = \frac{F_q\left(\frac{1}{3}\right)}{m_{qT}} \tag{5.14}$$

$$p_M = \frac{F_q\left(\frac{2}{3}\right) - F_q\left(\frac{1}{3}\right)}{m_{qT}} \tag{5.15}$$

$$p_S = \frac{m_{qT} - F_q\left(\frac{2}{3}\right)}{m_{qT}} \tag{5.16}$$

and

$$\aleph_2 = max(p_I, p_M, p_S) - min(p_I, p_M, p_S) \tag{5.17}$$

thus, the extreme values and their meanings are described in Table 5.2. Naturally, rather than these extreme situations, in experimental work it is more usual finding intermediate distribution patterns. In Appendix A, Table A.1 shows the adopted criteria for classifying the intermediate cases, establishing the numerical bands for each indicator.

During the experimental work, this criteria was implemented by means of a computational code in Python and the classification of each experimental case was automatically obtained in the course of the results post-processing stage. The bands adopted for the classification of the different segregation types were arbitrary fixed on the basis of several experimental experiences. Therefore, if a rapid idea about the distribution of the product of interest along the bed and the segregation degree is wanted, knowing the Segregation Level ($\aleph_2$) and the Segregation Type is enough.

Table 5.2: TTSIS extreme values.

p_I	p_M	p_S	$\aleph_2$	Meaning
0.33	0.33	0.33	0.00	Pure Uniform distribution
0.00	0.00	1.00	1.00	Full Top Segregation
0.00	1.00	0.00	1.00	Full Central Segregation
1.00	0.00	0.00	1.00	Full Bottom Segregation
0.50	0.00	0.50	0.50	Pure V-Segregation

The most important advantages of the TTSIS are that it directly gives an intuitive idea about the segregation profile, it captures in somehow the shape of the distribution curve, and it is simple to be calculated. However, its main disadvantage is the fact that the volume occupied by the product of interest cannot be greater

than one third of the bed volume, or incoherent results would be obtained (like a TTSIS of the form [pI>0,pM>0,pS<1] for a full top segregation). Anyway, since a good contact between adsorbent and product should be guaranteed the volumetric fraction of the food material in AFD applications will be always less than 0.33, and the TTSIS can be applied.

5.5.2 General assumption for bed height estimation

In segregation experiments that will be described in Section 5.5.4, each layer of the fluidized bed was taken by vacuuming and its thickness was estimated as a fraction of the total bed height proportionally to the total mass in the layer. This calculus is valid as long as the solid phase bulk density of the layer is approximately equal to the solid phase bulk density of the entire bed. Mathematically that is,

$$m_{sT} = (\alpha_{AT}\rho_A + \alpha_{PT}\rho_P)h_{bed}A_{sup} \tag{5.18}$$

$$m_{si} = (\alpha_{Ai}\rho_A + \alpha_{Pi}\rho_P)\Delta h_i A_{sup} \tag{5.19}$$

then,

$$\frac{m_{si}}{m_{sT}} = \frac{(\alpha_{Ai}\rho_A + \alpha_{Pi}\rho_P)\Delta h_i}{(\alpha_{AT}\rho_A + \alpha_{PT}\rho_P)h_{bed}} \tag{5.20}$$

thus, if $\alpha_{AT}\rho_A + \alpha_{PT}\rho_P \cong \alpha_{Ai}\rho_A + \alpha_{Pi}\rho_P \ \forall i$,

$$\frac{m_{si}}{m_{sT}} = \frac{\Delta h_i}{h_{bed}} \tag{5.21}$$

The preceding assumption would no longer be valid if the void fraction along the bed were non-uniform, or the solids bulk density varied because of considerably differences in the mixture composition. Nevertheless, since during the vacuuming operation the bed is in settled state, it can be said that the differences in compaction of the adsorbent have quite reduced effect on bulk solids density. Furthermore, as the utilized foodstuff concentrations are very low, their influence in the solids bulk density is negligible. Therefore, the uniform distribution of solids bulk density can be assumed.

5.5.3 Theoretical test of segregation indexes

In order to investigate the influence on segregation indices of two experimental factors, the number of layers and the layer actual height, and the general assumption of constant solids density along all the bed (Section 5.5.2 and Equation 5.51), a

mathematical test was performed, considering an hypothetical fluidized bed containing a mixture of 12 kg of bran and 87.8 g of lyophilized carrot discs. Four kinds of segregation patterns were forced distributing the food material in different ways along the bed (Table 5.2), and all the other variables were calculated, considering not only the mass distribution of bran and carrots and their volumetric fractions, but also the space occupied by air (void fraction). Then, the number of layers, layer thickness, and solids density were varied, and mass balances were solved for each case in order to obtain a coherent mass distribution. For full top as well as full bottom segregation, it was imposed that all the food material concentrates in the upper and lower layers respectively, whereas for central segregation, it was set a concentration in the two middle layers. For V-segregation, it was assumed that one half of the mass of carrots concentrates in the top layer, and the other half in the bottom one. Regarding to the fluidized bed, it was assumed a volume of 0.0482 m^3 and a sectional area of 0.1225 m^2.

General equations

A mass distribution vector ($\vec{P}_{dis}$) of dimension n_{lyr} (n_{lyr}: number of layers), was defined in order to impose the product distribution along the bed. The value of each component of $\vec{P}_{dis}$ was varied between 0 and 1, according to the type of segregation supposed. Then, the mass of product in each layer is calculated with the following expression,

$$m_{Pi} = m_{PT} P_{dis,i} \tag{5.22}$$

Depending on the type of segregation profile evaluated, the elements of the mass distribution vector were fixed as shown in Table 5.3.

The overall bulk density of solid phase,

$$\alpha_{ST}\rho_{ST} = \alpha_{AT}\rho_A + \alpha_{PT}\rho_P \tag{5.23}$$

where,

$$\alpha_{AT} = \frac{m_{AT}}{\rho_A V_T} \quad and \quad \alpha_{PT} = \frac{m_{PT}}{\rho_P V_T} \tag{5.24}$$

Depending on the factor studied, the mass of adsorbent and volume of each layer were calculated applying different equations described in the following subsections.

Number of layers

The mathematical test was performed supposing 2, 6, 10 and 100 vacuumed layers. Despite the last value is not realistic, it was considered aiming to know what would happen in the limit.

Table 5.3: Imposed values of the elements of the product mass distribution vector according to the segregation pattern studied.

Segregation type	$P_{dis,i} =$
Full Bottom	$\begin{cases} 1 & i = 1 \\ 0 & i > 1 \end{cases}$
Full Top	$\begin{cases} 1 & i = n_{lyr} \\ 0 & i < n_{lyr} \end{cases}$
Full Central	$\begin{cases} 0.5 & i = \frac{n_{lyr}}{2} \\ 0.5 & i = \frac{n_{lyr}}{2} + 1 \\ 0 & \forall i \neq \frac{n_{lyr}}{2}\ AND\ i \neq \frac{n_{lyr}}{2} + 1 \end{cases}$
Pure V	$\begin{cases} 0.5 & i = 1 \\ 0.5 & i = n_{lyr} \\ 0 & 1 < i < n_{lyr} \end{cases}$
Uniform	$\begin{cases} \frac{1}{n_{lyr}} & \forall i \end{cases}$

When only the effect of the number of hypothetical vacuumed layers was evaluated, that is, ideal cases without variations in the solids bulk density along the bed and layers with equal thickness, the layer volume (V_i), and the total mass of solids and mass of adsorbent in each layer (m_{ST}), were calculated as follows:

$$V_i = \frac{V_T}{n_{lyr}} \tag{5.25}$$

$$m_{Ti} = \rho_{ST} \alpha_{ST} V_i \tag{5.26}$$

$$m_{Ai} = m_{Ti} - m_{Pi} \tag{5.27}$$

Non-uniform distribution of solids bulk density

In order to evaluate how segregation indexes are affected by different solids bulk densities along the bed, i.e. a no uniform solid density distribution, variations on solids bulk density of each layer with respect to the overall bed solids bulk density were applied. For this end, a variation factor, k_{co}, defined as the ratio between the

solids bulk density of a single layer (ρ_{Si}) to the *total* solids bulk density (ρ_{ST}). This factor was varied by means of two straight lines with positive and negative slope intercepting in a maximum value at the bed center, considering that if there was a variation of the solids bulk density, the maximum of compaction would be located in the central layers. This assumption was made on the basis of the observations made during the experimental work, which in some cases presented a top zone with less compacted material and a bottom zone with evidences of more expanded material with product displacement.

Moreover, the k_{co} maximum value was imposed for the test ($k_{co,max}$), whereas its minimum value was calculated as the reciprocal of this maximum.

Therefore, the solved equations were the following,

$$k_{co} = \frac{\alpha_{Si}\rho_{Si}}{\alpha_{ST}\rho_{ST}} \tag{5.28}$$

$$k_{co,min} = \frac{1}{k_{co,max}} \tag{5.29}$$

$$c_e = \lceil \frac{n_{lyr}}{2} \rceil + 1 \tag{5.30}$$

The slopes of the curves for density variations were obtained with

$$\gamma_1 = \frac{k_{co,max} - k_{co,min}}{c_e - 1} \tag{5.31}$$

$$\gamma_2 = \frac{k_{co,min} - k_{co,max}}{n_{lyr} - c_e} \tag{5.32}$$

Thus,

$$k_{co,i} = \begin{cases} \gamma_1(i-1) + k_{co,min} & i < c_e \\ k_{co,max} & i = c_e \\ \gamma_2(i - c_e) + k_{co,max} & i > c_e \end{cases} \tag{5.33}$$

Then, the overall solids bulk density is calculated applying Equation 5.23, the mass of product in each layer is determined by Equation 5.22, and the layer volume is given by Equation 5.25. Further, the variations in the solids bulk density in each layer were introduced through a two steps procedure. In the first step, the product and adsorbent volumetric fractions are estimated by the hereunder expressions, where α_{Ai} is derived by combining Equations 5.23 and 5.28.

$$\alpha_{Pi_0} = \frac{m_{Pi}}{\rho_P V_i} \tag{5.34}$$

$$\alpha_{Ai_0} = \frac{k_{co,i}\alpha_{ST}\rho_{ST} - \alpha_{Pi}\rho_P}{\rho_A} \tag{5.35}$$

The mass of adsorbent and the total mass of solids in each layer are given by:

$$m_{Ai_0} = \alpha_{Ai_0} \rho_A V_i \tag{5.36}$$

$$m_{Si_0} = m_{Ai_0} + m_{Pi} \tag{5.37}$$

Since $k_{co,i}$ is a discrete function of the layer number, the total mass of adsorbent in the bed obtained applying this factor might not be the total mass of adsorbent imposed in the beginning (12 kg). Consequently, the overall mass fraction of product may change, producing an alteration in the variables involved in those indexes involving mass fractions (M index and "s" index), and causing an invalidation of the comparisons between cases where constant solids density was supposed and the current cases. Therefore, as a second step in the calculation of the mass of adsorbent in each layer, the values previously obtained were verified and corrected as follows:

$$m_{ATc} = \sum_i m_{Ai_0} \tag{5.38}$$

$$m_{Aadd} = m_{AT} - m_{ATc} \tag{5.39}$$

$$\begin{aligned} &if\ m_{Aadd} > 0, then: \\ &\qquad m_{A(c_e-1)} = m_{A(c_e-1)_0} + 0.5 m_{Aadd} \\ &\qquad m_{A(c_e+1)} = m_{A(c_e+1)_0} + 0.5 m_{Aadd} \\ &if\ m_{Aadd} < 0, then: \\ &\qquad m_{A1} = m_{A1_0} + 0.5 m_{Aadd} \\ &\qquad m_{An_{lyr}} = m_{An_{lyr}} + 0.5 m_{Aadd} \end{aligned} \tag{5.40}$$

Thus, the final values of volumetric fractions of adsorbent, food product, and air are obtained as follows:

$$\alpha_{Pi} = \frac{m_{Pi}}{\rho_P V_i} \tag{5.41}$$

$$\alpha_{Ai} = \frac{m_{Ai}}{\rho_A V_i} \tag{5.42}$$

$$\alpha_{ai} = 1 - (\alpha_{Ai} + \alpha_{Pi}) \tag{5.43}$$

As in these cases all the layers were considered with the same thickness, it was calculated with the following equation:

$$\Delta h_i = \frac{h_{bed}}{n_{lyr}} \tag{5.44}$$

Then, the values applied for $k_{co,max}$ in the present test were 1.025 and 1.05, assuming that in an actual case, if there were differences in the solids bulk density along the bed, they should not be greater than 5 %. This assumption is based in experimental observations, where even at low air velocity the adsorbent on the middle layers is more or less expanded because of the air passing by.

Variation of layer thickness

Since the layer thickness and bed height are independent variables directly or indirectly utilized for evaluating the three tested segregation indexes (TTSIS, M and "s"), it is of special importance to consider what would be the effect on them if the layers had different thickness than h_{bed}/n_{lyr}. Therefore, the Top, Central, and Bottom layers thickness was varied in ±40 % with respect to the other ones, which were maintained with the same thickness. In order to do that, a primary thickness distribution vector ($\vec{h}_{dis0}$) was defined with n_{lyr} components equal to 1. Then, after changing one of the elements of the the primary vector depending on the layer set as different (Table 5.4), a thickness distribution vector ($\vec{h}_{dis}$) was defined normalizing the primary one. Finally, the layer thickness and volume were calculated multiplying each element of the thickness distribution vector by the total bed height and volume, respectively.

Table 5.4: Variations applied to layer thickness and values given to the different elements of the primary thickness distribution vector.

Modified layer	$\vec{h}_{dis0}$ component	Value
Top	n_{lyr}	1.4
Top	n_{lyr}	0.6
Central	$\lceil \frac{n_{lyr}}{2} \rceil$	1.4
Central	$\lceil \frac{n_{lyr}}{2} \rceil$	0.6
Bottom	1	1.4
Bottom	1	0.6

For the normalization of the primary distribution vector, the sum of its elements was calculated first,

$$S_u = \sum_i h_{dis0,i} \tag{5.45}$$

then, the thickness distribution vector was determined as

$$\vec{h}_{dis} = \frac{\vec{h}_{dis0}}{S_u} \tag{5.46}$$

Therefore, the layer thickness and volume were obtained with the following equations:

$$\Delta h_i = h_{dis,i} h_{bed} \tag{5.47}$$

$$V_i = h_{dis,i} V_T \tag{5.48}$$

Hence, the masses of adsorbent and product, and foodstuff and adsorbent volume fractions are calculated with the procedure previously described (with $k_{co,max} = 1$ if density variations were not considered).

Criteria applied for evaluating the M index

As in the considered binary mixtures in the present work the lighter component, the food product, is at the same time the larger one, it is not possible to stablish *a priori* whether it will tend to sink or float. Therefore, it is not possible to evaluate the M index in terms of *jetsam* as it was originally defined. However, since the component of interest expected to segregate is the food material and its overall mass fraction is quite low, the M index was not evaluated in terms of concentrations of the jetsam, but in terms of the mass fraction of foodstuff. Anyway, the meaning of the index remains the same. In addition, as "upper" part of the bed it was considered its upper 40 %.

Adaptation of the "s" index

Since the numerator and denominator of Equation 3.2 (assuming the solid phase bulk density along the bed is approximately constant) were originally formulated for cell analysis from a grid, they had to be adapted for layer analysis. Then, working out the original equations (3.5 and 3.6), it is obtained:

$$\langle h_{large} \rangle = \frac{\sum_i m_{Pi} h_i}{m_{PT}} \tag{5.49}$$

$$\langle h_{small} \rangle = \frac{\sum_i m_{Ai} h_i}{m_{AT}} \tag{5.50}$$

where h_i is the height from the distributor to the layer center i, m_{Pi} and m_{Ai} represent, respectively, the mass of food product and adsorbent in the layer i, and m_{PT} and m_{AT} mean the total mass of product and adsorbent in the bed.

5.5.4 Experiments

Different homogeneously mixed binary mixtures containing bran and lyophilized food materials were utilized to evaluate the effect of particle shape, concentration, fluidization time, food density and air velocity on segregation. With the scope of verifying the general validity of the applied methods for evaluating the effect of air superficial velocity on segregation, an experiment series was carried out with no homogeneously mixed mixtures,

In order to investigate the food particles displacement during the fluidization, part of food particles were marked as tracers in some experiments. Two kinds of tracers were differentiated with different colours: Top Tracers (initially in the upper third of the bed), and Bottom Tracers (initially in the lowest third of the bed). TTSIS was also calculated for tracer particles, allowing an easy and simple description of the foodstuff movement during the process.

Furthermore, based on the results of the previous experiments and the study of bran behaviour during fluidization at different velocities (Channel Generation and Collapse Cycle and Food Particles Transport Mechanisms), the spouted-jet bed (L20spjet) was applied in some experiments. However, for this kind of experiments it was needed to know first the maximum allowed air velocity avoiding the expulsion of bran by the bed top caused by the bed fountain. Therefore, only one concentration of food material was used (1/20 fresh product to bran mass ratio), the maximum allowed air velocity, and 20 minutes of fluidization time.

Fluidization time and layer vacuuming

Except for experiments starting with inhomogeneous mixtures or special tests for evaluating the effect of time on segregation, the applied fluidization time was 20 minutes for experiments performed in the fluidized bed (L35b) as well as in the spouted-jet bed (L20spjet). Once elapsed the fluidization time, the air supply was rapidly shut off, then the mixture was collected in six layers by means of a vacuum cleaner and sieved. Then, adsorbent and food material were weighted separately in order to know their concentration in each layer.

Although the thickness of each layer was roughly measured during the vacuum operation in order to obtain as regular as possible layers, some difficulties arose during the vacuuming procedure. Therefore, layer thickness was estimated with the following formula for results processing (assuming the solid phase bulk density along the bed is approximately constant):

$$\Delta h_i = \frac{m_{Ai} + m_{Pi}}{m_A + m_P} h_{bed} \tag{5.51}$$

Performed experiments and utilized nomenclature

Each experiment was identified with an alphanumeric code like *aaannnnRbbtee*, where: *aaa* is the food material code; *nnnn* is the theoretical u/u_{mfA} multiplied by 100; *bb* is the denominator of fresh product to adsorbent ratio corresponding to the lyophilized material-bran mixture; *ee* is the fluidization time in minutes. In Table 5.5 are listed all performed experiments in the L35b fluidized bed, their ID, lyophilized material concentration, velocity, and air flow, while in Table 5.6 are listed all experiments carried out in the L20spjet. In order to differentiate the latter from the former ones, the suffix "L20spjet" was added to their nomenclature.

On the other hand, for results analysis of experiments carried out in the L35b, since the difference between theoretical u/u_{mfA} and the actual one is negligible, the theoretical velocities ratio was considered.

Table 5.5: Conditions for lyophilized material-bran experiments performed in the L35b fluidized bed.

Experiment ID	Air flow (m^3/h)	Material	w_{PT}	u/u_{mfA}
POd0260R40t20	210	lyophilized potato	0.0046	2.75
POd0170R40t20	130	lyophilized potato	0.0046	1.70
POd0150R40t20	120	lyophilized potato	0.0046	1.54
POa0150R40t10	120	lyophilized potato	0.0035	1.47
POa0150R80t10	120	lyophilized potato	0.0016	1.47
POa0170R40t10	140	lyophilized potato	0.0036	1.82
POa0170R80t10	140	lyophilized potato	0.0017	1.71
PEb0260R20t20	200	partially lyophilized pea	0.0138	2.57
PEb0170R80t20	140	partially lyophilized pea	0.0039	1.75
PEa0260R20t20	200	lyophilized pea	0.0093	2.57
PEa0260R80t20	200	lyophilized pea	0.0023	2.56
PEc0230R20t20	175	lyophilized pea	0.0109	2.42
PEc0190R20t20	145	lyophilized pea	0.0109	1.93
PEa0150R20t20	120	lyophilized pea	0.0089	1.49
PEa0150R80t20	120	lyophilized pea	0.0024	1.49
CAa0260R20t20	200	lyophilized carrot	0.0069	2.60
CAa0260R40t20	200	lyophilized carrot	0.0033	2.60
CAa0260R80t20	200	lyophilized carrot	0.0012	2.59
CAb0190R20t20	145	lyophilized carrot	0.0053	1.85
CAa0170R20t20	140	lyophilized carrot	0.0060	1.75
CAa0170R40t20	140	lyophilized carrot	0.0032	1.76
CAa0170R80t20	140	lyophilized carrot	0.0014	1.76
CAa0150R20t20	120	lyophilized carrot	0.0067	1.50
CAa0150R40t20	120	lyophilized carrot	0.0034	1.49
CAa0150R80t20	120	lyophilized carrot	0.0013	1.50
CAb0150R20t40	120	lyophilized carrot	0.0053	1.57
CAb0170R20t40	130	lyophilized carrot	0.0053	1.66
CAb0260R20t40	200	lyophilized carrot	0.0053	2.69

Table 5.6: Conditions for lyophilized material-bran experiments performed in the L20spjet spouted-jet bed.

Experiment ID	Air flow (m^3/h)	Material	w_{PT}	u (m/s)
PEcR20L20spjet	37	lyophilized pea	0.0109	0.51
PEfR20L20spjet	37	fresh pea	0.0500	0.51
CAbR20L20spjet	37	lyophilized carrot	0.0053	0.51
CAdR20L20spjet	37	fresh carrot	0.0500	0.51

Chapter 6

Computational details

6.1 Preliminary simulations of sand fluidized beds

6.1.1 Preliminary coarse simulation

As a first preliminary test for comparing experimental bed behaviour and simulation results, sand fluidization was simulated. Then, its predictions were compared with sand fluidization experiments in the L13b.

The superficial velocity used in both simulations and experiments was 1.18 m/s, and simulations were carried out in a 2D grid with squared cells of Δx= 0.001 m. For granular temperature the algebric model (described in the ANSYS Fluent 13 Theory Guide (2010)) was used, whereas for the calculation of the momentum exchange the Gidaspow's model was applied. Gas properties and sand properties are described in Table 6.1.

Table 6.1: Gas and sand properties.

	solid (sand)	**gas (air)**
ρ (kg/m^3)	2550	1.23
μ_f (Pa.s)	-	1.79×10^{-5}
α_i	0.59	0.41
d_P (m)	1.8×10^{-3}	-
Shape	spheric	-

6.1.2 Grid independence, and 2D/3D equivalence

Grid independence was evaluated by performing simulations of fluidized bed refining successively the grid and the time intervals. Since it is a well-known material and

its fluidization is widely studied, sand was used for the present test (properties described in Table 6.1). The air superficial velocity was set equal to 1.274 m/s, the Gidaspow model was adopted for the drag force modelling, the First Order Upwind method was applied for spatial discretization, and First Order Implicit method was utilized for time integration. The refinement was carried out for 2D as well as 3D grid, and 2D/3D equivalence was assessed.

As fluidized bed size and real time simulated are concern, it was adopted a 0.2 m width by 0.8 m height bed for 2D simulations, and a 0.2 m sided square base by 0.8 m height bed for 3D cases, and the elapsed time was 7 seconds. Furthermore, the material height was 0.4 m for every case.

For further references it was adopted an alpha-numerical nomenclature *ddsggggTttt* being "gggg" the grid code, "ttt" the time step code, and "dd" the dimension code (2D or 3D). Cell size and time step interval, and reference codes for both refinement parameters are described in Tables 6.2 and 6.3 respectively.

Table 6.2: Cell size used for grid refinement.

Code	Cell type (2D / 3D)	Cell side (mm)	Number of cells (2D / 3D)
0150	square / -	1.5	71556 / -
0200	square / -	2.0	40000 / -
0250	square / cubic	2.5	25600 / 2048000
0500	square /cubic	5.0	6400 / 256000
1000	square / -	10.0	1600 / -

Table 6.3: Time step utilized for time step independence test.

Code	Time step (ms)
0100	1.00
075	0.75
050	0.50

The temporal evolution of pressure drop, bed height, volumetric solid fraction, phase and slip velocities were analysed. In addition, contour plots of solid volumetric fraction, and horizontal and vertical profiles of the temporal mean of solid volumetric fraction were also considered.

Since the solid phase velocity was found the most sensible variable to refinement effects, further analysis were carried out considering the Courant number of this

phase defined as:

$$Co = \frac{\langle \|\vec{v}_2\| \rangle \Delta t}{\Delta x} \tag{6.1}$$

where $\langle \|\vec{v}_2\| \rangle$ is the temporal mean of the volumetric mean of the magnitude of the the solid phase velocity, Δt is the time step size, and Δx is the cell side.

Grid Convergence Index (GCI)

The refinement error for the finest grids was estimated calculating the GCI for the variables of interest, by applying the method described by Roache (1997). The GCI is a method for uniform presenting grid-convergence studies, based on generalized Richardson Extrapolation involving comparison of discrete solutions at two different grid spacings. The GCI of a given variable for the finest grid is:

$$GCI_{21} = \gamma_s \frac{f_2 - f_1}{r_{21}^p - 1} \tag{6.2}$$

where γ_s is a safety factor, r_{21} is the refinement factor between coarse and fine grid, and f_1 and f_2 are the values of the variables for the finer and the coarser grids,

$$r_{21} = \frac{h_2}{h_1} \tag{6.3}$$

being h_i the cell size.

In the present work, it was used the safety factor suggested by Roache, with a value of 1.75.

6.2 Results of the preliminary tests

6.2.1 Grid and time step refinement

Figure 6.1 shows the convergence with time step and grid refinement of the main analysed variables. This convergence to unique values can be observed not only as the time step is refined, but also as the cell size is reduced.

Analysing time-averaged vertical profiles of solid volume fraction (Figures 6.2 and 6.3), it can be noted that whereas most cases present smooth profiles, cases s0150T100, s0250T100, s0150T075, and s0250T075 show rough curves, denoting numerical discontinuities. Even more, in these last cases the observed mean bed height is sensibly higher than in the other cases showing smooth volumetric fraction vertical profiles (about 0.75-0.85 m versus 0.50-0.55 m, respectively), and their pressure drop and solid phase velocity (Figures 6.1(a) and 6.1(d)) show a marked difference with respect to the mean values presented by the other cases. A clearer example of

numerical discontinuities in the entire domain of the solid phase is shown in Figure 6.5.

Another important conclusion emerging from the results is the fact that the solid phase is the most affected one by refinement, which is reflected in pressure drop, solid phase velocities, and solid vertical profiles. In slip velocities magnitude this situation is less evident since it is the magnitude of the difference between air and solid phases velocities, being the former greater in its magnitude and less sensible to refinement changes.

These discrepancies may be explained from the point of view of the mathematical method applied for obtaining the unsteady solution; even though it was used the Eulerean implicit first order method for time discretization and this method is unconditionally stable, using a fine grid with a relatively coarse time step may lead to spatial oscillatory solutions mainly attributed to dissipation errors. Whereas in explicit schemes for time discretization, the constrain of a Courant number less than one is required for obtaining a stable solution, this condition is not needed for implicit schemes, which are stable for any size of time step. However, when an accuracy of first order in time is applied, small time steps must be used for ensuring the accuracy of the results minimizing the numerical dissipation.

Therefore, the relation between cell size and time step should be taken into account anyway. From Courant values shown in Table 6.4, it can be said that for these kind of simulations numerical discontinuities can be avoided when Courant numbers of solid phase are less than about 0.095, which can be interpreted as a time step to cell size ratio less than about 0.4 s/m for *a priori* estimations.

Table 6.4: Courant numbers for solid phase in sand fluidised bed simulations.

	T050	T075	T100
s0150	0.088	0.190	0.313
s0200	0.064	0.094	0.225
s0250	0.053	0.098	0.174
s0500	0.024	-	0.046
s1000	0.012	-	0.024

Furthermore, pressure drop value obtained in the finest refinement is quite close to its theoretical value (5987 Pa and 5903 Pa, respectively). In addition, estimations of Grid Convergence Index, give acceptable values for refinement error. In Table 6.5 are shown values of main variables obtained with the finest grid and time step, and their respective errors estimated applying GCI analysis.

Regarding to s1000 cases (2Ds1000T050 and 2Ds1000T100), in Figure 6.1 it can be seen that the main variables remain quite close with a successive grid refinement,

Table 6.5: Main variables and their refinement error obtained by GCI analysis in 2D cases.

	ΔP (Pa)	$\langle\|\|\Delta\vec{v}_{21}\|\|\rangle$ (m/s)	$\langle\|\|\vec{v}_1\|\|\rangle$ (m/s)	$\langle\|\|\vec{v}_2\|\|\rangle$ (m/s)
value	5987	2.57	2.103	0.263
GCI ($\pm$)	453	0.0158	0.0817	5.60×10^{-4}

maintaining practically the same values with time step reduction. However, their time averaged volumetric mean solid profile (Figure 6.4) are mainly flat, without undulations. That means that the presence of bubbles is not accurately predicted. Moreover, the fact that main variables values are close to converging values (and Co < 0.095 in Table 6.4) may be attributed to the cancellation of discretization errors between them rather than a greater accuracy in the simulations (as mentioned in Section 4.1.2).

Therefore, considering figures where the convergence of the most important analysed variables is shown and the analyses in previous paragraphs, it is possible to say that grid and time step independence for 2D simulations of a fluidized bed of sand is reached with Δx = Δy = 0.0015 m and a Δt = 0.0005 s.

Focusing on the 2D/3D equivalence, Table 6.6 shows pressure drop, and phase and slip velocities for two 3D simulations performed at different time steps and the same cell size. Since considerable long times are required for simulation of 3D cases (as it will be discussed hereafter), only two time step refinements were done without performing grid refinement simulations. Only one simulation with a finer grid was lunched, but it did not reach the numerical steady state (about 3 seconds of real time) since for simulating one second of real time it is necessary about one month of computational time. Nevertheless, the difference in the main analysed variables between the 3D case and its analogue 2D case for the finest time step is not greater than 8 %. Thus, 2D simulations might be initially accepted as first approach for the simulation of a fluidized bed.

Table 6.6: Time averaged values of the main variables analysed from 3D simulations carried out in the 3Ds0500 grid.

Case	ΔP (Pa)	$\langle\|\|\Delta\vec{v}_{21}\|\|\rangle$ (m/s)	$\langle\|\|\vec{v}_1\|\|\rangle$ (m/s)	$\langle\|\|\vec{v}_2\|\|\rangle$ (m/s)
3Ds0500T050	5792	2.42	2.08	0.23
3Ds0500T100	5065	2.34	2.15	0.35

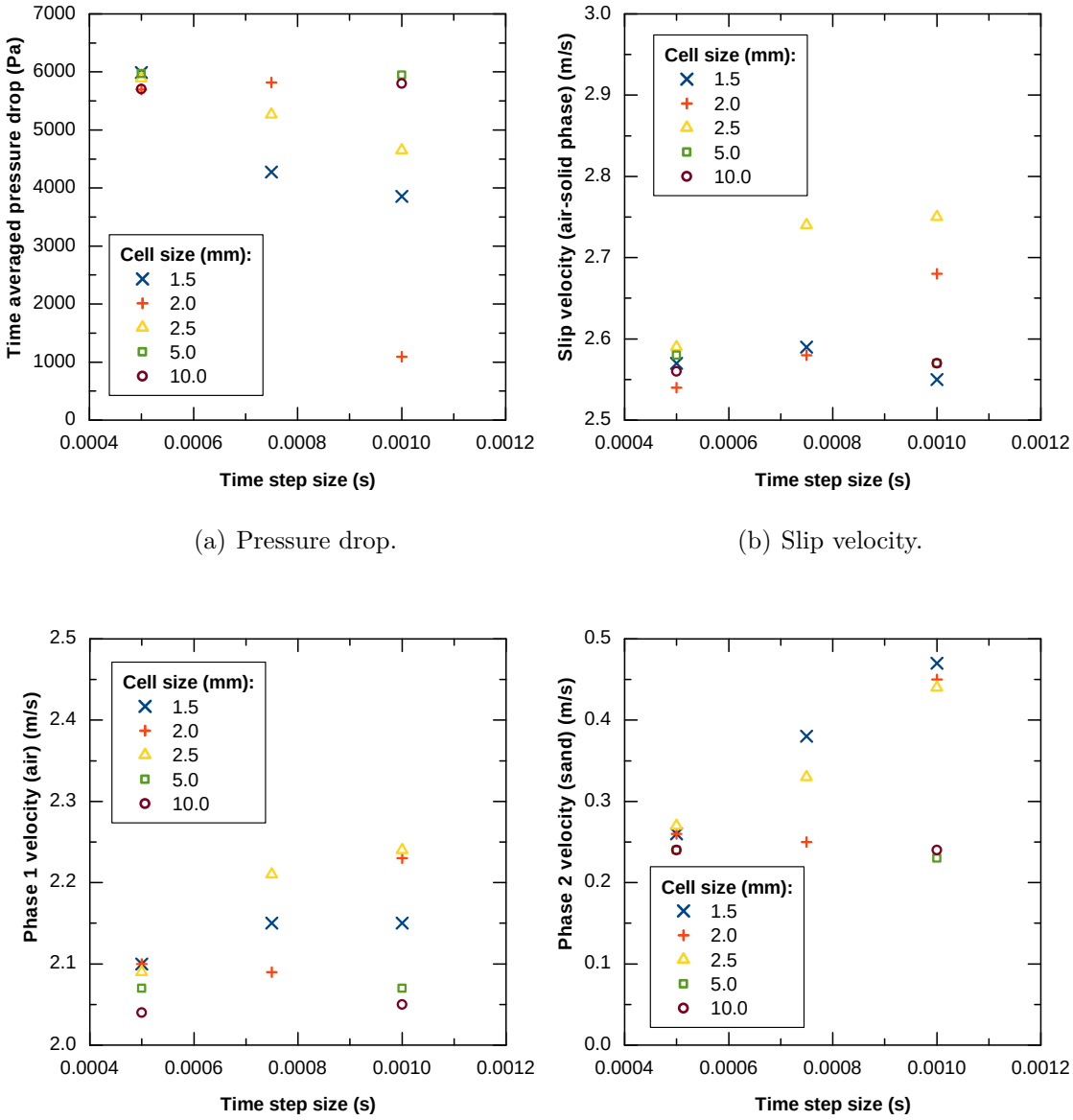

(a) Pressure drop.

(b) Slip velocity.

(c) Air phase velocity.

(d) Solid phase velocity.

Figure 6.1: Convergence with grid and time step refinement of main variables (time averaged volumetric means, 2D cases).

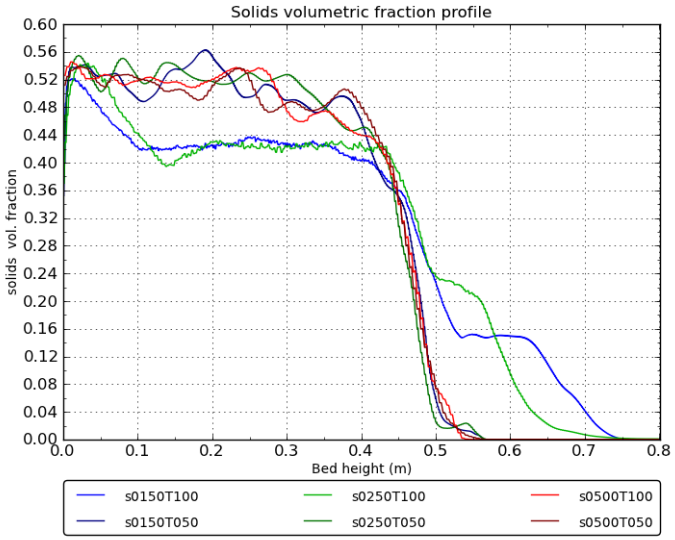

Figure 6.2: Time average of solid volumetric fraction profiles for different 2D simulations. Coarsest and finest grid and time step refinements (except 2Ds1000 cases).

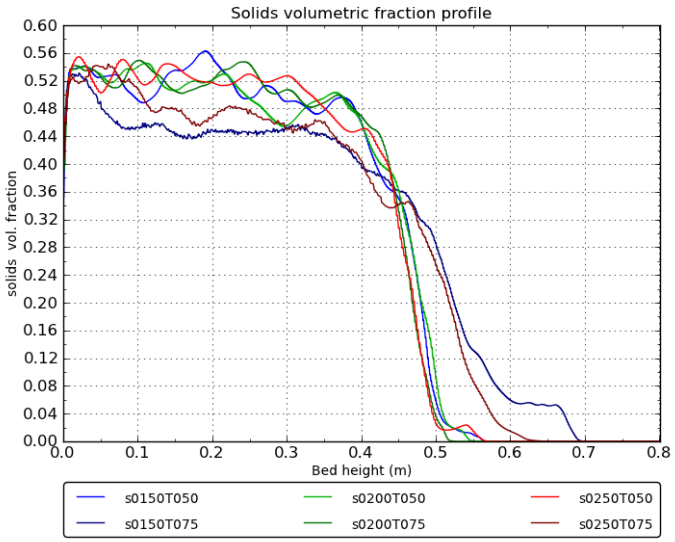

Figure 6.3: Time average of solid volumetric fraction profile for different 2D simulations. Intermediate grid and time step refinements.

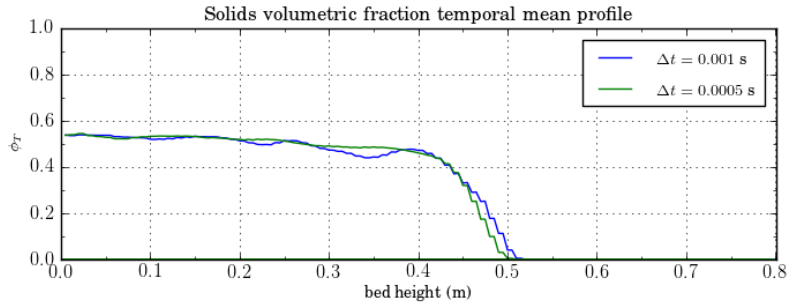

Figure 6.4: Time average of solid fraction volumetric profile for 2Ds1000 cases.

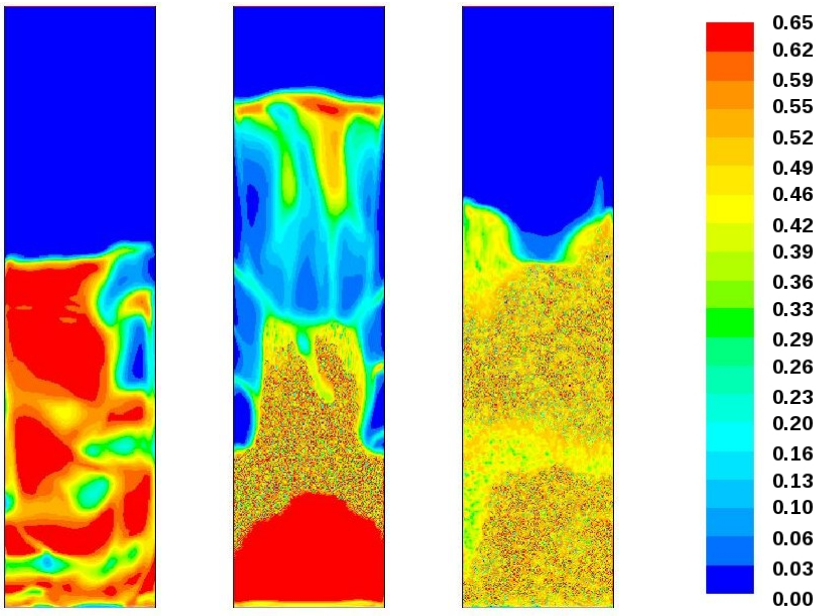

(a) s0150T050 (b) s0150T075 (c) s0150T100

Figure 6.5: Time step and grid refinement in simulation of a sand fluidized bed. Contourplots of volumetric fraction of solid phase at t=6.5 s for different cell sizes and time steps.

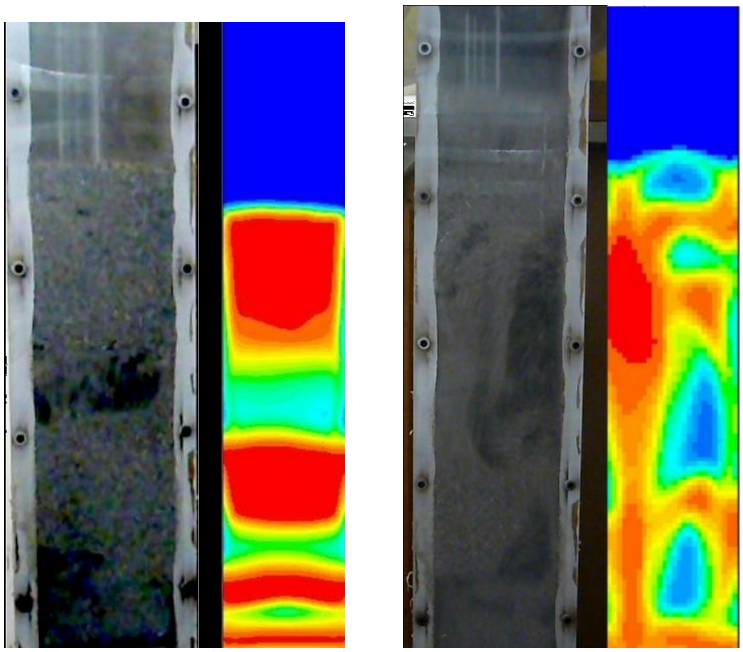

(a) - (b) -

Figure 6.6: Two similar situations found in a real fluidized (L13b) bed and its simulation.

As further information, Table 6.7 shows the number of hours of computational time required for simulating one second of fluidization.

Table 6.7: Simulation times for sand fluidised bed (h computational time/s actual simulated time).

Type	Grid Code	T050	T075	T100	Number of cells
2D	s0150	17.03	9.48	7.28	71556
	s0200	29.76	19.68	15.90	40000
	s0250	27.81	3.43	2.72	25600
	s0500	1.44	–	0.73	6400
	s1000	1.00	–	0.50	1600
3D	s0250	652.54	–	289.98	2048000
	s0500	68.13	–	34.10	256000

Among the possible situations found in an experimental fluidized bed, in Figure 6.6 two snapshots of fluidization of sand in the L13b fluidized bed and its corresponding simulation in a finer mesh (Figure 6.6(a)) and in a coarser mesh (Figure

6.6(b)) can be seen.

Time is not reported in the figures because of an obvious reason: situations taking place in a given instant of time in a experiment, will not necessary take place elapsed the same time in the next repetition. They can occur few seconds before, few seconds after, or even do not occur. For example, in the first repetition of an experiment, a big bubble might be formed after 3 seconds at 0.2 m from the bed bottom, whereas in the second repetition a big bubble can appear after 5 seconds, at the same bed height or slightly different, or even, only smaller bubbles at different bed height can be formed during the first 8 seconds of fluidization.

6.2.2 Effects of the refinement errors on heat transfer coefficients and temperature

Based on the results of the previously mentioned simulations, the effect of grid and time step refinement was evaluated for heat exchange in a three-phasic system. In this case, a binary mixture composed of semolina and potato was simulated, and material properties and potato to semolina proportion were taken from Donsì *et al.* (2003). However, the initial conditions for solid phases temperatures were set differently to the cited article in order to establish a greater temperature difference among all involved phases. These initial temperatures were: semolina, 264 K; potato, 255 K; and air, 273 K.

The Gunn's correlation was used for calculating the gas to solids phases heat exchange coefficient (Gunn, 1978).

Table 6.8 shows the time average of the main variables considered in the current test (which is, in fact, a case involving two solid phases with similar characteristics to an AFD case). In Figure 6.7 are presented the contour-plots of phase 2 (semolina) for different meshes and time steps.

In Figure 6.7(a) are clearly observed the presence of numerical discontinuities (previously described for sand cases) leading to dramatical differences in the velocities field and physical impossible values of pressure drop for these conditions. Nevertheless, comparing values of temperatures with the other presented cases, it can be seen that the effects on heat exchange is considerably small.

Comparing cases s0150T050SL and s0250T100SL, it is possible to note that the differences between time averaged volumetric means of velocities magnitudes, bed height, and pressure drop are sensibly small, and the effect of grid and time step refinement on heat exchange is negligible. Though, it can be seen that in relative terms solid phases velocities are the most influenced variables.

From the mathematical point of view, this reduced effect of grid and time step on heat exchange variables can be explained considering how heat exchange coefficients are calculated; since they are calculated considering the relative velocities between

gas and solid phases (slip velocities) whose effect of refinement is less than 0.1 %, and Reynolds number is elevated to a power of about 0.8, the possible numerical errors on heat coefficients are significantly reduced.

Table 6.8: Time averaged variable of cases with heat exchange with different grid and time steps.

	s0150T050SL (A)	s0150T100SL (B)	s0250T100SL (C)	C-A
$\langle\|\|\vec{v}_1\|\|\rangle$ (m/s)	0.304	1.191	0.304	-6.1×10^{-4}
$\langle\|\|\vec{v}_2\|\|\rangle$ (m/s)	0.051	0.876	0.060	9.2×10^{-3}
$\langle\|\|\vec{v}_3\|\|\rangle$ (m/s)	0.047	0.820	0.047	4.2×10^{-4}
$\langle\|\|\Delta\vec{v}_{21}\|\|\rangle$(m/s)	0.434	1.287	0.436	2.3×10^{-3}
$\langle\|\|\Delta\vec{v}_{31}\|\|\rangle$ (m/s)	0.419	1.358	0.422	3.3×10^{-3}
$\langle T_1\rangle$ (K)	263.98	264.00	263.99	1.1×10^{-2}
$\langle T_2\rangle$ (K)	264.00	264.00	264.00	-3.1×10^{-5}
$\langle T_3\rangle$ (K)	255.00	255.00	255.00	-2.3×10^{-5}
$\langle\alpha_1\rangle$	0.75	0.75	0.75	-1.8×10^{-4}
h_{bed} (m)	0.42	0.42	0.43	3.8×10^{-3}
ΔP (Pa)	2502	491	2483	-19

6.2.3 Summary

If a First Order method is applied for time as well as space discretization, a time step size of 0.5 ms and a cell side of 5 mm (squared cells) are enough for guaranteeing an accurate prediction of the velocity field and the pressure gradient in a fluidized bed, for cases similar to the ones evaluated.

Regarding to the heat exchange, it takes place at a greater temporal scale than changes in the velocity field. In addition, since the exchange coefficients are calculated using the slip velocity, a slightly affected variable by grid refinement, it is practically not affected by numerical errors derived from simulations using coarser grids. Therefore, heat exchange (and even mass transfer, if heat exchange analogies are used for transfer coefficient estimations) might be simulated in coarser grids, at least for coarse simulations or model testing.

Due to small differences between the 2D simulations and 3D ones, the former may be used for a first approach to the simulation of a fluidized bed. Moreover, as a *rule of thumb* for simulating fluidized bed with similar solids (density, diameter, velocities) once established the grid cell size, the time step size can be defined in function of $\Delta t/\Delta x = 0.4$ s/m.

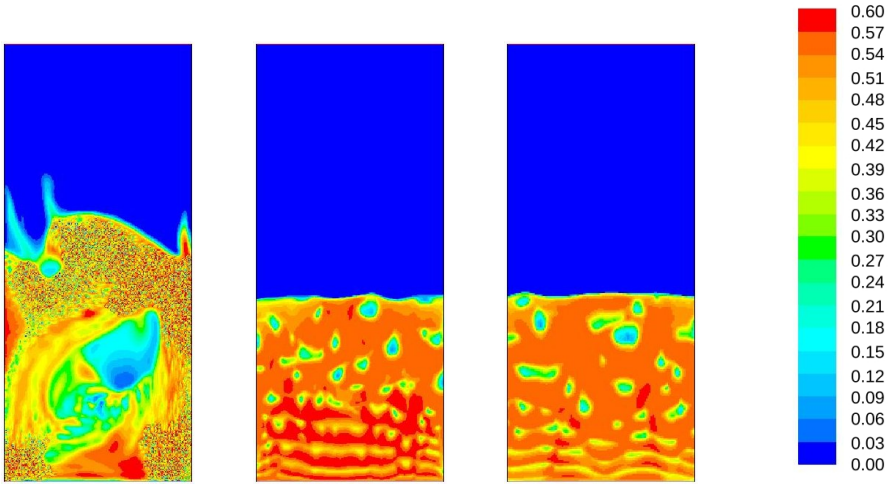

(a) s0150T100SL (b) s0150T050SL (c) s0250T100SL

Figure 6.7: Time step and grid refinement in simulation of a semolina-potato fluidized bed. Contourplots of volumetric fraction of semolina phase at t=5.0 s for different cell sizes and time steps.

6.3 Drag correlations

With the scope of identifying the most accurate drag model for the simulation of bran and other particles in a fluidized bed, three drag models were tested by means of measuring different powders minimum fluidization velocities through simulation. Experimental data about materials, their densities, particle diameters, and minimum fluidization was taken from *Donsí et. al. (2003)* (except information about wheat bran which was taken from the present work).

Simulations were carried out in a 2D grid of 0.15 m width by 0.30 m height. Based on the results presented in Section 6.2, 2.5 mm sided squared cells, and a time step of 0.5 ms were used. The simulated determination of minimum fluidization velocity was performed by simulating 0.15 m of material in the fluidized bed for 6 seconds of real time at different velocities. Then pressure drop and bed expansion versus velocity was plotted and the powder minimum fluidization velocity was determined.

Since the Gidaspow (GP) and Wen and Yu (WY) drag models are the most used in literature, and the Mazzei and Lettieri (ML) model is a novel drag formulation supposed to work in a wide range of fluidization regimes, they were chosen for the test. The minimum fluidization velocity measurement was done for each material and each drag model. Table 6.9 shows the employed materials, volume fraction, velocity ranges, and their experimental minimum fluidization velocity (experimental values from B to E were taken from Donsì *et al.* (2003), whereas values for U were

obtained in the present work).

Table 6.9: Utilized materials properties, and velocities used for simulated minimum fluidization velocity measurement.

Code	Material	$u_{mf.exp}$ (m/s)	α_i	Velocity range (m/s)	Velocity step (ms)
B	Semolina	0.12	0.59	0.04-0.20	0.04
C	Corn flour	0.20	0.51	0.04-0.28	0.04
S	Starch	0.0014	0.43	0.0002-0.0022	0.0004
Z	Zeolites	0.19	0.41	0.11-0.27	0.04
E	Bentonites	0.21	0.50	0.13-0.33	0.04
U	Wheat bran	0.17	0.212	0.09-0.27	0.04

6.4 Wheat bran-lyophilized carrot binary mixture simulation

Finally, simulations of the L35b fluidized bed with a bran-lyophilized carrot binary mixture were carried out in order to investigate the possibility of simulating this kind of mixtures, and reproduce the segregation pattern experimentally found. Thus, cases CAa0150R20, CAa0170R20 and CAa0260R20 were considered for simulation in a 2D grid with squared cells (2.5 mm sided), and time step of 2 ms. Since the aim of these simulations was not the study of heat exchange, energy balance was not activated.

Part III

Results and discussions

Chapter 7

Evaluation of drag correlations

Figure 7.1 shows the minimum fluidization velocities predicted by simulation using different drag models compared with their experimental values for several materials (from Table 6.9). In some cases (such as simulations performed using starch), it was not possible to predict accurately a minimum fluidization velocity by simulation, and their data-points were omitted. In these cases strange variations of pressure drop with fluidization velocity were obtained such as abrupt oscillations and/or a lack of stable values at any velocity. As an example, in Figure 7.2 curves are shown for two extreme cases with coherent and incoherent values (for further curves see Appendix A.4).

As it can be noted, points for starch are missing in the Figure 7.1. For this material, it was not possible to estimate the minimum fluidization velocity by means of simulation since the obtained pressure drop versus velocity curve was represented by a single line of constant pressure (equal to theoretical pressure drop) for all velocities. Due to its chemical characteristics (polymer of glucose) and its small particle size, starch presents very cohesive behaviour for fluidization with formation of channels because of the presence of interparticle forces. This characteristic seems to be the cause of the impossibility of predicting starch minimum fluidization velocity by means of CFD simulation, since all tested drag models do not take into account these forces.

Concerning predictions applying Mazzei and Lettieri's (ML) model, it can be seen that minimum fluidization velocity could be estimated only for three materials (bentonite, corn flour, and wheat bran), as they were the only materials presenting reasonable pressure drop versus velocity curves, from the point of view of curve shape. Turning to the cases where Gidaspow's model was applied, reasonable pressure drop versus air velocity curves were obtained leading to an accurate estimation of minimum fluidization velocity for almost all materials. Nonetheless, despite obtained incipient fluidization velocity values are quite close to experimental ones, for

bentonite there is a difference of about 36 %. Finally, results obtained by applying Wen and Yu (WY) model showed, in general, a reasonable agreement for the majority of materials.

Recalling theoretical basis for WY and ML correlations (Section 4.2.4), they consider expansed fluidized beds, without inter-particle interactions, and particles in hydrodynamic equilibrium between their effective weight (gravity force and buoyancy) and drag forces. This equilibrium means that particle settling velocity has been reached by the particle, or in other words, the slip velocity between the particle and the fluid is the fluid velocity affected by a function of the void fraction.

On the other hand, when the fluid has not reached the minimum fluidization velocity the drag force acting on each single particle is less than its effective weight, and and gravity acceleration would prevail. Though, since the particle is in a system of particles, two additional forces are exerted on its surface; a normal force reaction from the particles below, and the weight of particles above it. Consequently, the particle has not only zero acceleration, but also zero velocity. In other words, the equilibrium is maintained as the result of not only drag, weight and buoyancy, but also interaction with other particles. This can be the reason of the discrepancies found when trying to predict the pressure drop versus velocity by applying ML and WY correlations, since they are based on particle settling velocity, absence of interactions with other particles, and hydrodynamical equilibrium of an isolated particle.

As it was mentioned at the beginning of the present Section, one of the difficulties presented in predicting pressure drop versus velocity curves were odd shaped curves and their oscillations. In Figures 7.3 and 7.4 it can be observed that the WY curves show unexpected shapes like a parabola, where the ascendant pressure drop and the constant pressure drop parts are not clearly identified. Although a minimum fluidization velocity was anyway estimated their precision is not acceptable. Furthermore, it can be observed that the pressure drop oscillations (minimum and maximum values) considerably increase for simulations applying WY.

Regarding to the minimum fluidization velocity predicted for wheat bran, although a good agreement could be obtained using GP model for momentum exchange coefficient, a no physical bed contraction was presented by all simulations performed (even using WY and ML). Since the theoretical pressure drop was reached in all the curves applying the three tested drag models (Figure A.2 in Section A.4 of the Appendix), this behaviour can be attributed mainly to the lack of a specific model for pseudo-cohesive solids, beside the basis of each drag model.

Finally, unlike WY and ML models, Ergun's equation is based on the pressure drop across a packed bed. Consequently, the combination of this equation and WY model in the Gidaspow's model, allows a better estimation of pressure drop for packed beds as well as expanded beds. Therefore, more accurate estimations of minimum fluidization velocities by simulation could be obtained by applying GP

model for momentum exchange coefficient calculation.

Another question to be commented are minimum fluidization velocities calculated by means of direct application of Ergun's equation (modfied by Wen and Yu's constants). It can be noted that values calculated with this equation are in general considerably different from experimental ones. These differences might be attributed to the fact that the simplifications introduced by Wen and Yu do not consider the fluid volume fraction in particular form, but in generalized form combined with the shape factor. Anyway, the deviation from experimental values are in agreement with the error margin reported by those authors.

7.1 Summary

According to the results obtained in the present work and several results found in literature (evaluating drag correlations by different approaches), for the moment the best correlation for drag coefficient calculation in fluidized beds of solid and gas is the one proposed by Gidaspow. Even though other authors obtained better results with other correlations, the Gidaspow's equation seems to be the most accurate and safe to be applied.

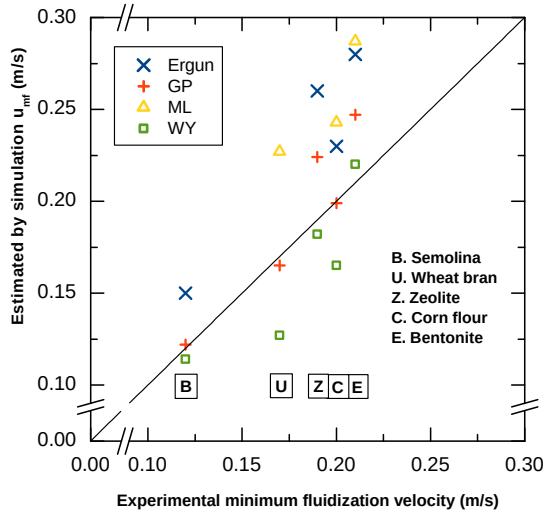

Figure 7.1: Minimum fluidization velocities for different adsorbents: estimated values versus experimental ones. (GP: Gidaspow's model, ML: Mazzei and Lettieri's model, WY: Wen and Yu's model)

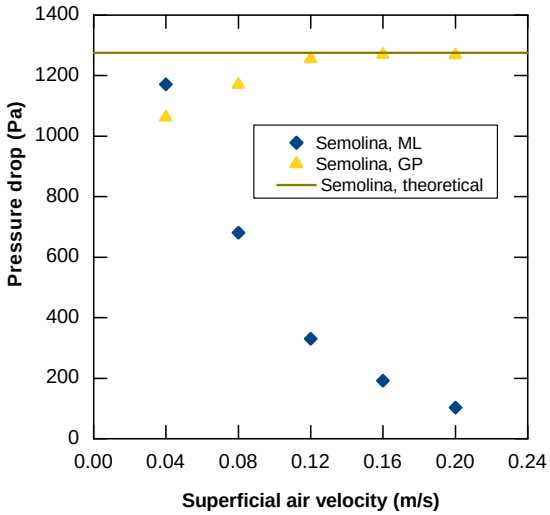

Figure 7.2: Two cases of simulated pressure drop versus velocity curves. Expected and incongruent curves for semolina, obtained applying GP and ML models, respectively.

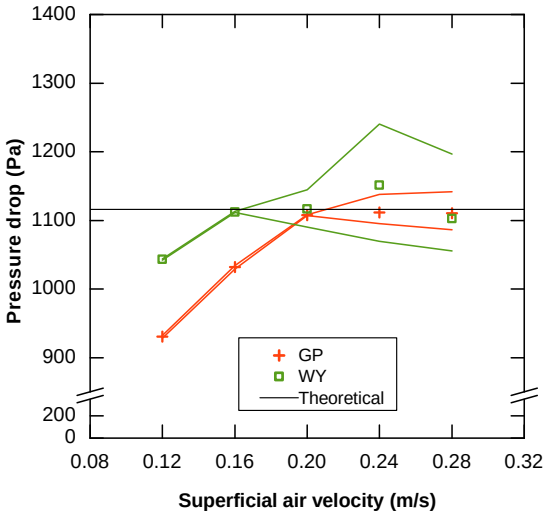

Figure 7.3: Simulated pressure drop versus velocity curves for corn flour (C) (GP: Gidaspow's model, WY: Wen and Yu's model). The solid lines represent the maximum and minumum values reached.

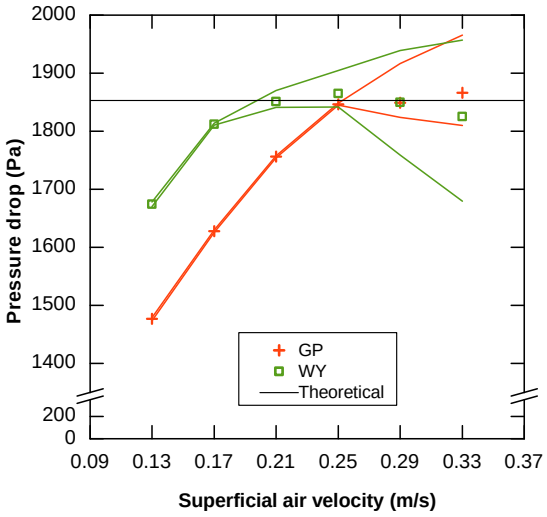

Figure 7.4: Simulated pressure drop versus velocity curves for bentonite (E) (GP: Gidaspow's model, WY: Wen and Yu's model). The solid lines represent the maximum and minumum values reached.

Chapter 8

Characterization of the adsorbent and food materials

8.1 Adsorbent

8.1.1 A qualitative description of bran particle

Bran is the hard outer layer of cereals consisting of combined aleurone and pericarp, produced as a by-product of milling in the production of refined grains. Hence, bran particles exhibit a very irregular plane shape (Figure 8.1), and rests of grain brush (Figure 8.1(b)) and broken pericarp on the surface might be present. These characteristics confer to the particle a rough surface and, as undesired consequence, the possibility of mechanical interaction during fluidization.

(a) Plane shape of bran particles.

(b) Grain brush and broken pericarp in the surface.

Figure 8.1: Bran particles.

8.1.2 Wheat bran density and maximum water content

Table 8.1 shows wheat bran densities and its maximum content of water, which is the maximum water content that can be reached by bran if water were not only adsorbed but also absorbed. This value does not give information about the adsorption, but only gives a reference for an extreme situation.

Table 8.1: Bran density, water weight fraction of wet bran, and absorbed water weight ratio.

	Value	CI	CI (%)
ρ_b (kg/m^3)	312	20	6
ρ_a(kg/m^3)	1469	0.1	≈ 0
C_w	2.05	0.03	1.4
w_w	0.73	0.01	1.3

8.1.3 Particle Size distribution

In the histograms of the wheat bran particle size distribution (PSD) presented in Figure 8.2, it can be noted that this material exhibits a negative skewed distribution. On the other hand, from results of photographic analysis it was obtained a particle thickness of 140 μm. Hence, as it can be seen in Table 8.2, Sauter's diameter and minimum fluidization velocity of each class could be obtained, and their Geldart type was established. Taking into account the results from figures previously mentioned, it can be observed that about a 90 % of particles population belongs to Geldart B group, whereas only approximately a 10 % is Geldart A. In other words, the presence of Geldart C (cohesive) particles is negligible.

8.1.4 Minimum fluidization velocity of wheat bran

In Figure 8.3 the pressure drops versus air velocity are plotted. As it is expected, the pressure drops increases linearly increasing air velocity up to a maximum value, and then, it slightly decreases to finally remain stable between 0.18 and 0.22 m/s. The linear part of the curve finishes at approximately 0.17 m/s, and after this point the mean pressure drop is about 800 Pa, which is quite near to its theoretical value, which is 858 Pa (at 0.115 m from bed bottom). Consequently, it is concluded that the global minimum fluidization velocity of wheat bran under tested conditions is 0.17 m/s.

Table 8.2: Bran equivalent diameters, shape factors, and minimum fluidization velocities.

d_i (μm-mesh)	d_{SV} (μm)	ψ	u_{mf} (m/s)	Geldart	d_V (μm)
32	46.5	0.41	0.006	A	114
69	100	0.52	0.018	A	193
100	143	0.58	0.029	A	247
188	257	0.69	0.066	B	375
375	474	0.80	0.156	B	595
750	818	0.87	0.330	B	945
1500	1286	0.86	0.570	B	1500
2250	1588	0.81	0.740	B	1966

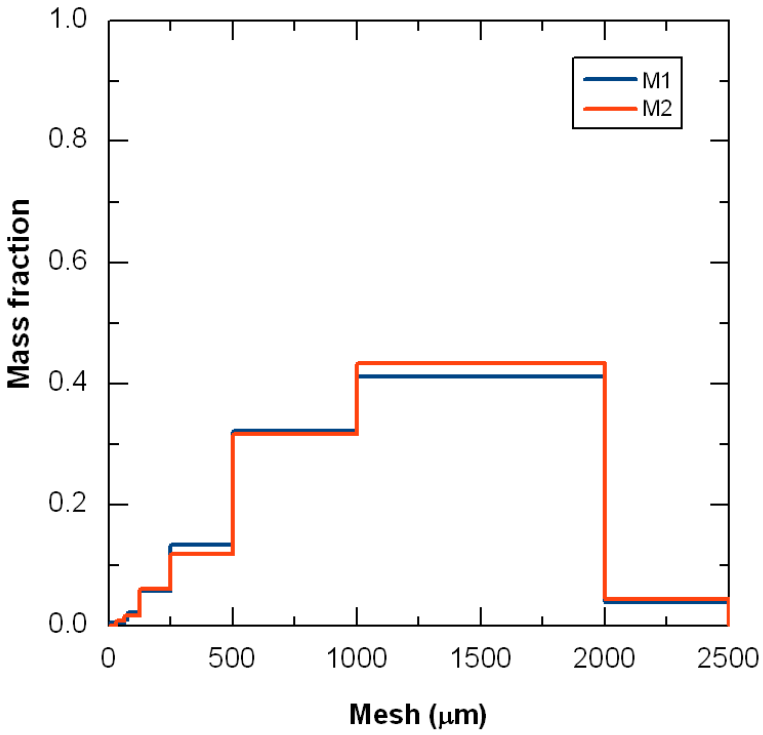

Figure 8.2: Bran particle size distribution (M1 and M2).

8.1.5 Equivalent diameter for fluidization (EDF)

Taking into account the obtained density by gas-picnometric techniques (1469 kg/m^3), from Equation 5.5 it can be calculated an EDF of 626.6 µm. Anyway, since this equation has an error of about 25 % for determining minimum fluidization velocity, the

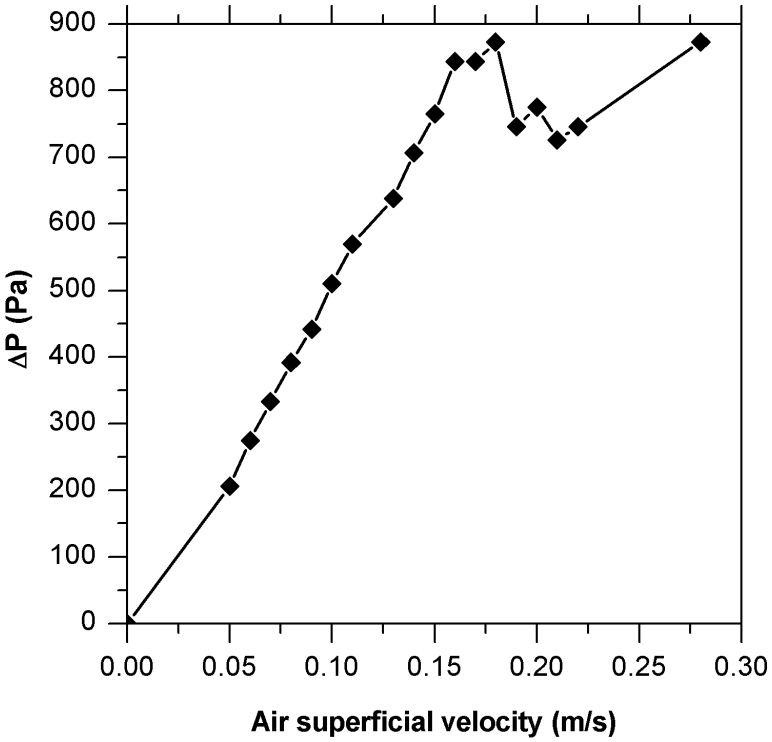

Figure 8.3: Pressure drop versus air velocity.

obtained value for EDF should be considered only as an approximation. Nonetheless, the EDF is an useful approximation which will be used for CFD simulations.. Moreover, according to this density and EDF values, Geldart's classification for bran would be B type.

8.2 Food materials

Density and particle dimensions were measured for carrot discs, potato slabs, and peas in fresh, lyophilized, and, for peas, partially lyophilized form (values showed in Tables 8.3 and 8.4). Furthermore, volume, surface and Sauter's equivalent diameters were estimated, and shape factor and specific surface were calculated. In general, it was seen that the particle shapes employed present roughly similar specific superficial area (about 640 m^2/m^3), and shape factors ranging between 0.48 and 1.00 (sphere).

Table 8.3: Geometric characteristics of food materials used for binary mixtures.

Code	Material	Particle shape	Dimensions (m)	S×10^3 (m^2)	V×10^6 (m^3)	a_P(m^2/m^3)
CAf	carrot	disc	l=0.005,d=0.035	2.47	4.81	514
CAa	lyophilized carrot	disc	l=0.005,d=0.018	0.792	1.27	622
CAb	lyophilized carrot	disc	l=0.005,d=0.021	1.03	1.75	590
CAd	carrot	cube	l=0.005	0.15	0.125	1200
POa	lyophilized potato	slab	l_1=l_2=0.0125,l_3=0.005	0.563	0.781	720
POb	potato1	cube	l=0.01	0.600	1.00	600
POc	potato2	slab	l_1=l_2=0.0125,l_3=0.005	0.563	0.781	720
POd	lyophilized potato	slab	l_1=l_2=0.04,l_3=0.005	4.00	8.00	500
PEa	liophilized pea	sphere	d=0.0088	0.243	0.357	682
PEb	partially-lyophilized pea	sphere	d=0.0088	0.243	0.357	682
PEc	liophilized pea	sphere	d=0.0088	0.243	0.357	682
PEf	pea	sphere	d=0.0088	0.244	0.358	683

Table 8.4: Equivalent diameters, shape factors, densities, and maximum packaging limits of food materials.

Code	d_V(m)	d_S(m)	d_{SV}(m)	ψ	ρ (kg/m^3)	α_{max}
CAf	0.0209	0.0281	0.0117	0.557	1050±55	n/c
CAa	0.0134	0.0159	0.0095	0.719	158±8	0.70±0.05
CAb	0.0149	0.0181	0.0102	0.681	112±6	n/c
CAd	0.0062	0.0069	0.0050	0.81	1050±55	n/c
POa	0.0114	0.0134	0.0083	0.729	176±11	n/c
POb	0.0124	0.0138	0.0100	0.806	1070±13	n/c
POc	0.0114	0.0134	0.0083	0.729	1070±13	n/c
POd	0.0248	0.0357	0.0120	0.484	198±8	n/c
PEa	0.0088	0.0088	0.0088	1.000	202±7	0.77±0.04
PEb	0.0088	0.0088	0.0088	1.000	401±14	n/c
PEc	0.0088	0.0088	0.0088	1.000	237±8	0.75±0.04
PEf	0.0088	0.0088	0.0088	1.000	1088±37	n/c

n/c: not calculated

Table 8.5: Lyophilized material, general results.

Material code	m_0 (g)	m_f (g)	m_f/m_0	$(m_f/m_0)_{stuff}$
601.53	90.7711	0.151	-	
737.22	137.3	0.186	-	
1696	624.5	0.368	-	
CAb	825.7	88.18	0.107	0.100
PEc	1024.32	223.6	0.218	0.213

8.3 Final remarks

Accurate characterization of food materials could be made, using those whose density before drying is greater than 1000 kg/m^3 and once dried ranges between 100 and 250 kg/m^3. Regarding to food particle shape, slabs, spheres, cubes, and discs were considered with shape factors ranging between 0.48 and 1.00.

Concerning to wheat bran, its salient characteristics will be treated in the next chapter together with its fluidization behaviour.

Chapter 9

Fluidization behaviour of non-food wheat bran

Unlike sand or other materials presenting formation of regular bubbles, wheat bran exhibits canalization or preferential air paths generation, without regular formation of bubbles (Figures 9.1). Thus, despite the material is completely fluidized and bed expands when air is injected (as in a bubbling fluidized bed occurs), this last parameter remains at around minimum fluidization value and air "in excess" escapes through channels without rising the bed. Only some oscillations might be present at high velocities due to channel generation and collapse, as it is described below.

Therefore, considering the physical characteristics of the bran particles such as rough surface and remains of grain brushes, and particle size distribution (see Section 8.1.3), this behaviour can be attributed principally to mechanical interactions rather than electrostatic forces as occurs in cohesive powders. Thus, this kind of powder might be called "pseudo-cohesive".

Furthermore, the existence of three zones along the bed was observed in tests with the L20b[1] fluidized bed: top, middle and bottom. In the middle zone, there are no channels and air simply percolates through it, whereas in top and bottom the generation and collapse of channels follows a quite regular cyclical behaviour. However, depending on air superficial velocity the height of the middle zone can be very short (even null), or extend practically along all the fluidized bed. Despite these zones were observed only in L20b fluidized bed, since its plexiglass window completely covered one of its sides, their presence may be assumed for L35b[2] fluidized bed as well. Accordingly, segregation experiments using potato slabs (POd) have demonstrated the existence of these three zones presenting damaged potato slabs in

[1]L20b: square base 20 cm sided fluidized bed (Section 5.3.3)

[2]L35b: square base 35 cm sided fluidized bed (Section 5.3.1)

the bed bottom due to the agitation in this part of the bed, and their impossibility of rising the bed (see Section 10.2 for further information).

Figure 9.1: From left to right, first figure: initial condition potato-bran binary mixture, second figure: at minimum fluidization velocity, from third to fifth: fluidization at higher velocities (respectively, 2.2 u_{mfA}, 2.5 u_{mfA}, and 2.8 u_{mfA} approximately). Red line indicates the bed height at minimum fluidization velocity.

9.1 Channels Generation and Collapse General Cycle

Depending on air superficial velocity, in the bed might be formed only one big channel, few middle channels, or very few small ones. In general terms, it can be observed a cyclical behaviour of channels generation and collapse. The number of channels and their shape depend on air superficial velocity as well as the location in the bed where they are formed. For example, by comparing the abscissas of Figures 9.2(a) and 9.2(b) it can be noted an increment on the oscillation frequency of bed height and channel generation and collapse as air superficial velocity is augmented. In addition, a reduction of the average number of channels with increasing the mentioned variable can be observed. Hence, it can be said that this channelling behaviour follows the general cycle showed in Figure 9.3 where two main stages are represented: I, generation, and II, collapse. Furthermore, from experimental observations, it can be said that the behaviour of the channels generated in the upper part of the bed are comparable with a spouted bed whose air velocity is varied.

Therefore, the different phases of the Channels Generation and Collapse General Cycle are described as follows:

• **Abrupt pressure release:** It may take place either near the bed surface, originating a path after a burst (Figure 9.4, t = 49.0 s, L35b fluidized bed), or

far from the bed surface generating an internal channel extending up to a roof of compacted material. In the former case, the channel behaves like a spouted bed where air velocity has overcome the minimum spouting air velocity and a fountain of material thrown appears over the spout. Pressure drop through the channel reaches a maximum and starts decreasing. Similarly occurs with air velocity inside the channel and fountain height reaching their maximum magnitudes. Inversely, bed height is minimum.

• **Phase I (Generation):** Pressure continues releasing, and new channels may appear as the result of the splitting of one single channel (Figure 9.4, from t = 54.2 s to t = 61.4 s). Simultaneously, material coming from other parts of the bed and/or collapsing channel walls starts blocking it until kinetic energy of coming out air is not enough to drag the falling bran (Figure 9.5(a)). If the channel is formed in the upper zone of the bed, a sudden decrement of fountain height can be seen. This situation is analogous to a spouted bed whose air velocity is progressively reduced after overcoming its minimum spouting velocity.

• **Phase II (Collapse):** Falling material blocks the channel orifice and air starts to be accumulated, increasing pressure below the material layer. When the pressure below the accumulated material is greater than the sum of the hydrostatic pressure caused by the plug and the forces embedding the material, a new abrupt air release takes place. In other words, the measured pressure drop continues reducing due to the increment of pressure inside the channel (unlike it would be expected in a spouted bed which pressure drop remains almost constant during air velocity reduction). In the cases of upper channels, at the end of this phase, pressure drop as well as fountain height reach a minimum.

Thus, the layers above channels obstructing them constitute "weak zones" where the adsorbent is less compacted than the material in the surroundings. Nevertheless, not only the descending material in channel orifices can originate a "weak zone", but also the presence of another solid such as food particle may induce it (Figure 9.5(b), from t = 91.8 s to t = 92.9 s, L20b fluidized bed). In Figure 9.6 it can be seen how a channel originated below bed surface, and extending up to a roof of more compacted material, induces a "weak zone" above (t=0.0 to 4.4 s), and after about one second, a new channel appears extending to the bed surface and bursting. Once the pressure is released the channel walls collapse blocking the channel again (from t=8.0 to 14.8 s).

More clear observations of the previously mentioned cycle were done with experiments performed in the L065b[3] bed (whose most representative results are exhibited in Figures 9.7 and 9.8). Aspects regarding to pressure variations inside the channels were particularly noted, and thereby a more approximate idea about this variable

[3]L065b: cylindrical 6.5 cm diameter fluidized bed (Section 5.4.2)

during the channelling was obtained.

Due to the geometric characteristics of the bed (small diameter, cylindrical, etc) and bran particularities (such as mechanical interactions between particles), only one channel was formed, allowing the measurement of pressure drop and height of thrown material of a single channel without possible interferences caused by other channels. Moreover, it is important to remark that the measured pressure drop in this case is simultaneously affected by two main components. Beside the pressure drop produced by air drag forces acting on bran particles, the air accumulation inside the channel during the collapse phase causes another pressure difference. If the manometric pressure drop is considered as $(P_{atm} - P_{bed})$, it is measured as a positive value. On the contrary, if the channel were completely blocked by the falling material and air could not percolate through bran, the measured pressure drop would be negative during the second part of the channelling cycle. Therefore, since actually air is continuously passing through the bran particles independently of the phase of the channel generation cycle, the magnitude of the energy losses caused by air interacting with bran particles is greater than the pressure difference due to the air accumulation and the measured pressure drop will be always positive.

As a consequence, the pressure drop oscillates during the fluidization and the second stage of the channelling cycle can be easily identified (as it can be seen in Figure 9.7). However, unlike in a bubbling fluidized bed where eventual pressure drop oscillations are principally caused by bubbles, in a channelling case these oscillations mainly obey to pressure variations inside the channel.

Naturally, as the fluidized material behaves quite chaotically, the previous description is a generalization of what was observed in the Channel Generation and Collapse Cycle from the point of view of pressure drop and pressure inside the channels. Therefore, the variations of the considered variables observed in Figure 9.7 do not exhibit perfect a sinusoidal behaviour as it would be expected.

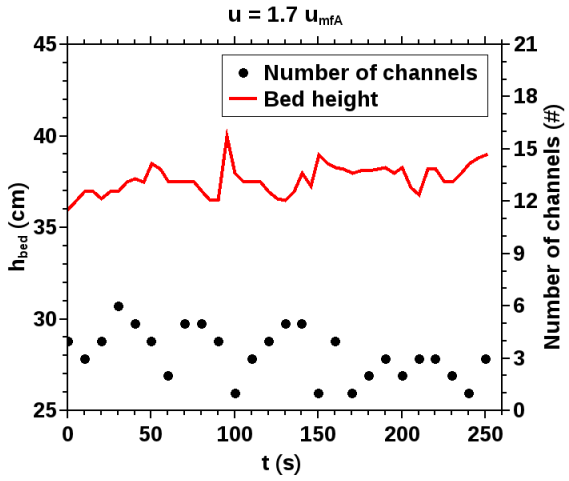

(a)

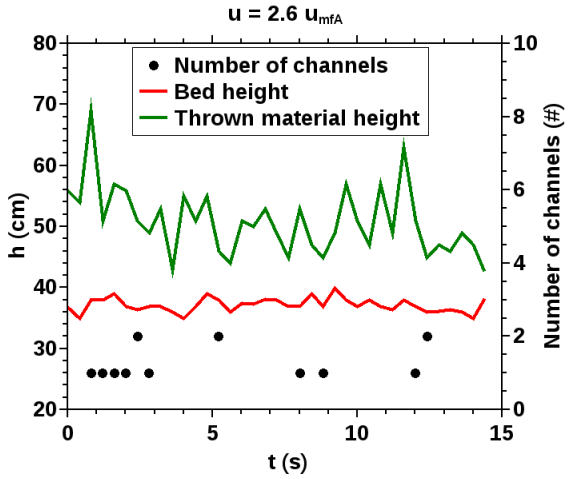

(b)

Figure 9.2: Number of channels and bed heights at different air superficial velocities (in L35b fluidized bed).

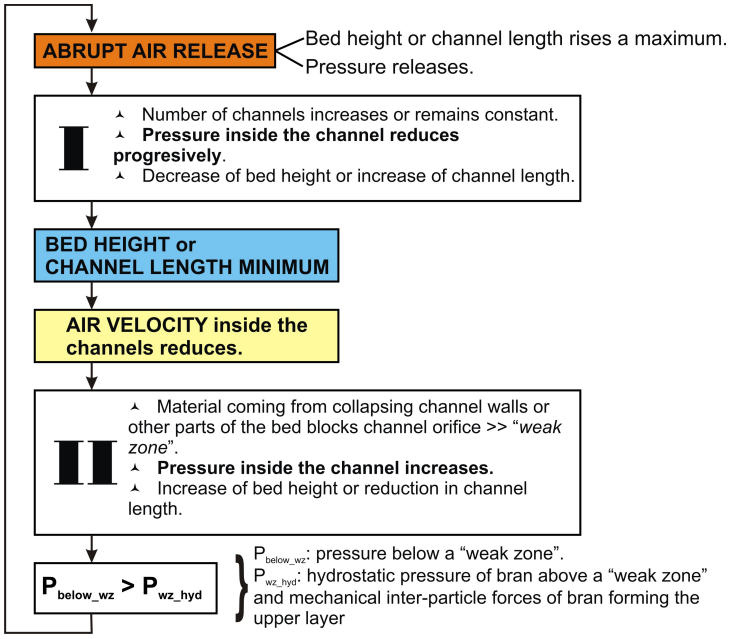

Figure 9.3: Channels generation general cycle.

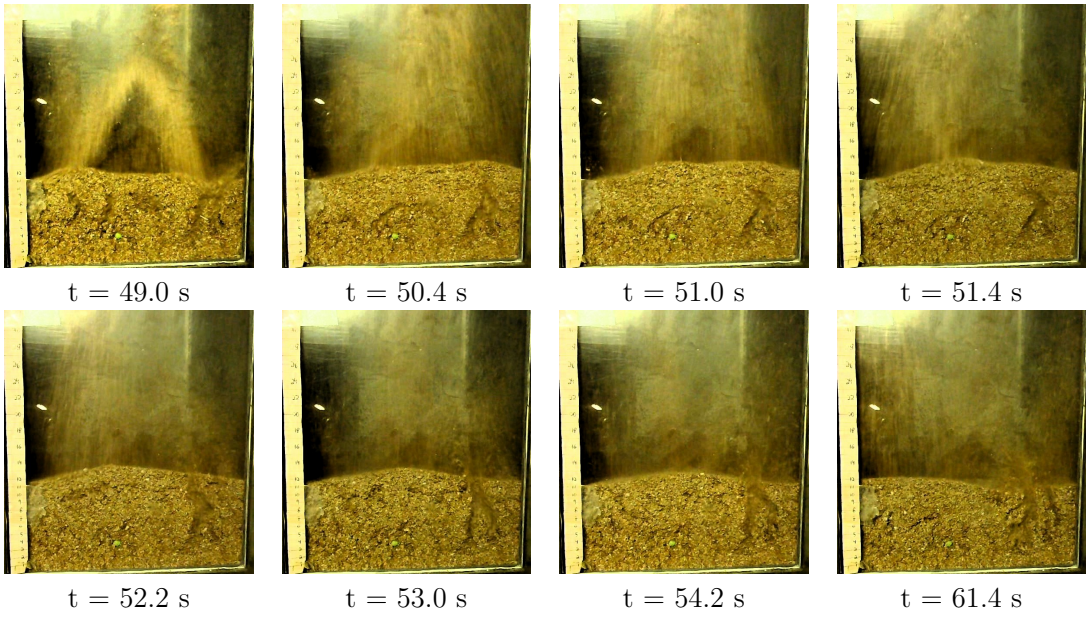

Figure 9.4: Generation, collapse, and generation of new channels (in L35b bed). On the right side of the fluidized bed, at a given t_0 (49.0 s), and after a succession of other channels bursting (not shown in the figure), a new channel is generated, whose orifice starts to be covered by bran particles coming from other zones of the bed. After about 2 seconds (t=51.0 s) the channel is blocked by bran particles creating a layer ("weak zone"). Under this layer pressure starts to increase, and a new burst is produced by the accumulated air, passing through a new path, augmenting its velocity, and carrying up the material that previously formed the "weak zone" (t=52.2 s). Thus, a new channel is generated, and since this explosion produces also the displacement and collapse of part of the adsorbent constituting the channel walls, the recently generated channel splits originating new channels (t=61.4 s).

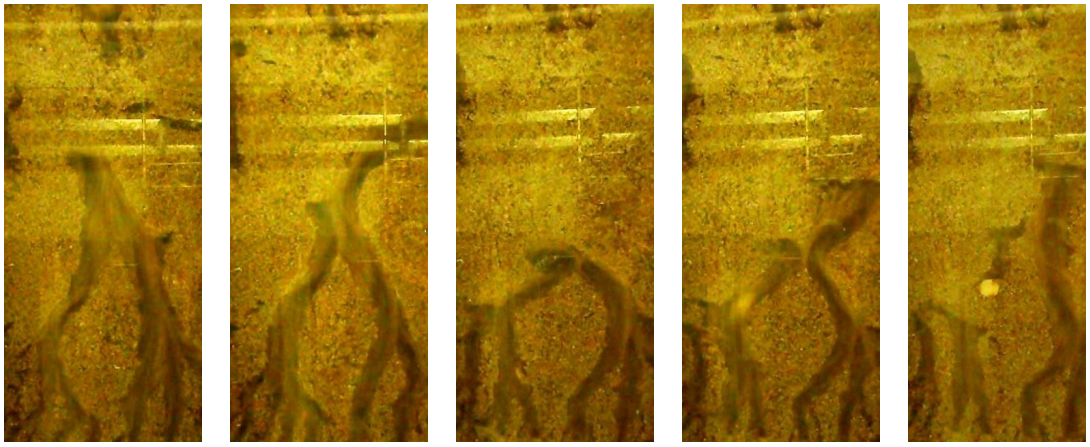

t = 0.0 s t = 3.2 s t = 6.6 s t = 7.08 s t = 7.96 s

(a) Generation and collapse of a channel, and active transport of a food particle.

t = 91.8 s t = 92.4 s t = 92.9 s t = 93.7 s t = 99.7 s

(b) Generation of a channel from a "weak zone" induced by the presence of a piece of food material (at 92.4 s "weak zone" break).

Figure 9.5: Channels generation and collapse in the bed bottom (L20b fluidized bed). At 0.0 s a previously formed channel starts to be blocked by descending material. After 6.6 seconds, the original channel is completely closed and pressure starts to rise in the remaining cavities for about 90 seconds. Then, air escapes by breaking an induced "weak zone" generating a new channel extending some centimetres above.

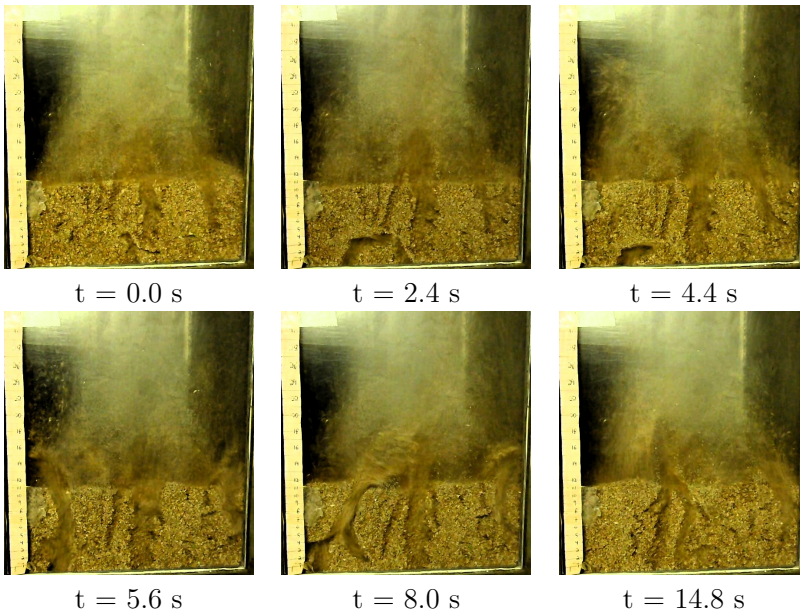

Figure 9.6: A channel originated below the bed surface induces a "weak zone" above (t=0.0 to 4.4 s), and after about one second, a new channel appears extending to the bed surface and bursting. Once the pressure is released the channel walls collapse blocking the channel again (from t=8.0 to 14.8 s).

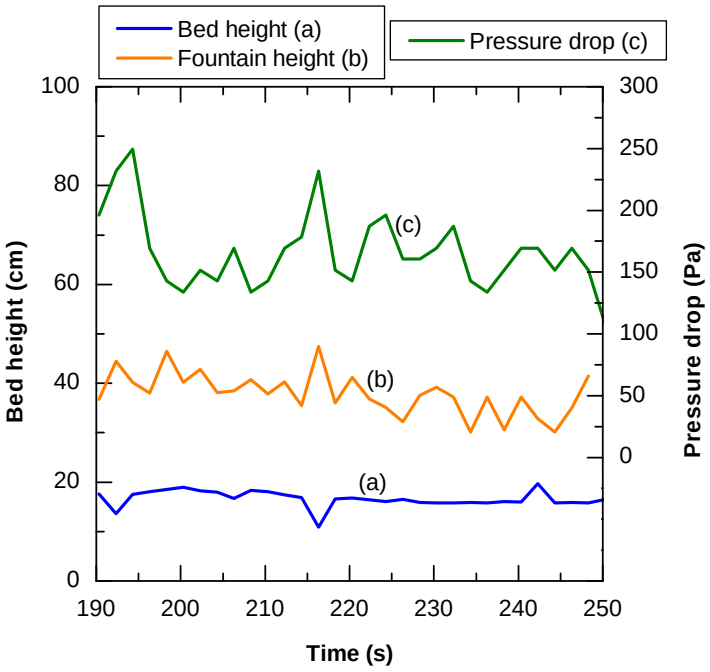

Figure 9.7: Oscillations of pressure drop, bed height, and height of thrown material (fountain) during bran fluidization in the L065b bed.

t = 210 s	t = 212 s	t = 214 s	t = 216 s	t = 218 s	t = 220 s
$\Delta P = 143$ Pa	$\Delta P = 169$ Pa	$\Delta P = 178$ Pa	$\Delta P = 232$ Pa	$\Delta P = 152$ Pa	$\Delta P = 143$ Pa

Figure 9.8: Frames corresponding to t between 210 and 220 seconds of Figure 9.7.

9.2 Final remarks

Despite the greatest part of wheat bran particles population belongs to Geldart B group, and the fact that the EDF belongs to that group as well, this material fluidizes like a Geldart C or A/C powder in a fluidized bed. Therefore, it is denominated "pseudo-cohesive". This behaviour depends principally on mechanical interactions rather than electrostatic forces, due to its physical characteristics (geometrical irregular shape, rests of grain brush, and surface roughness).

In a fluidized bed, bran presents three zones; top, middle, and bottom. Depending on air superficial velocity the middle zone may be present or not, characterized by more compacted material and absence of channels.

At the same time, the channel generation and collapse presents a cyclical behaviour whose repetition frequency and channelling characteristics (channel length, shape, number, etc) depends on air velocity.

Chapter 10

Mixing and segregation

10.1 Theoretical test of segregation indexes

Table 10.1 shows the most representative results of the theoretical tests described in Section 5.5.3. For further information, in Tables A.2, A.3, and A.4 of the Appendix A the complete results from all the tests are presented.

In Table 10.1 it can be seen that neither M nor "s" indexes are independent of the number of layers. Results obtained applying M present some differences when only the number of layers is varied for the same kind of segregation (e.g., for Full Central segregation, M is 0.5 for six layers, while it is 0.0 for 10 and 100 layers). Regarding to "s" index, unsatisfactory results were obtained as well; it not only does not recognise any difference between Full Central and Pure V segregations, but also its values for both cases are 0.0 (as perfectly mixed cases). In addition, "s" index values exhibited for Full Bottom segregation present a great dependence on the number of layers. In sum, from these results, it can be said that these indexes depend on the number of experimental vacuumed layers. In other words, beside they do not differentiate among the different kinds of segregation, they are affected by the experimental procedure leading to the impossibility of comparing results of experiments done with different number of layers. On the other hand, excepting the case with 2 layers, TTSIS present the expected values for each kind of segregation imposed, independently of the number of layers.

When a non-uniform solids bulk density distribution is considered (cases with $k_{co,max}{}^{1} \neq 1.000$ in Table 10.1.), M as well as "s" index show slight differences when cases with the same segregation patterns and different are compared, whereas none of the TTSIS indexes present any variation. Nonetheless, TTSIS exhibit differences with respect to its expected values when a change on a layer thickness is assumed, particularly when 6 vacuumed layers are supposed. Anyway, the deviations from the expectable values observed for M index are considerably greater than deviations

found for TTSIS. For example, for a Full Central segregation pattern, with 6 vacuumed layers, and a change of +40 % in the bottom, central, and top layers, M is 0.7 (which should be 0.0), whereas $\aleph_2$ of TTSIS gives a difference of at most -16 % (between 0.84 and 0.93) against its expected value for this pattern (1.00).

In general, in all tested indexes, the found deviations from the expected values for a given segregation pattern and their dependence on the number of layers, solids bulk density distribution, and layer thickness, may be attributed mainly to their mathematical definition. In particular, the dependence on the number of layers presented by M index for a Full Central segregation type obeys to the interpolation used for calculating the product concentration in the "upper" part of the bed; in the case with six layers, part of the central layers lie in the upper 40 % of the bed whereas when ten layers are considered, the central ones are situated just below this upper 40 %. Even though as "upper" part of the layer it was considered the 40 % of the bed, similar situations will be found taking a different bed fraction. On the other hand, the dependence on the number of layers for Full Bottom segregation cases shown by "s" index is caused by a the reduction of the denominator of Equation 3.3 ($\langle h_{large} \rangle$) as the number of layers is increased. Since in this kind of segregation it was considered that all the product is in the lowest layer, increasing n_{lyr} the height from the distributor to the bottom layer center (h_i, in Equation 5.49) reduces and the product $m_{Pi}h_i$ is lower. Moreover, the numerator of Equation 3.3 remains practically constant due to the great quantity of adsorbent considered, and the theoretical maximum segregation estimated by Equation 3.4 does not depend on the number of layers. Consequently, the value given by "s" index augments.

Summarizing, M and "s" indexes present many difficulties if the comparison among experiments done in different fluidized beds and/or different number of layers is intended. In addition, they do not allow to distinguish different segregation patterns leading to some mistakes when the segregation patterns are near to the extreme cases (such as Pure V, Full Central, or Full Bottom). On the opposite, since TTSIS considers only the distribution of a product of interest along the bed dividing the bed in three parts, it does not present great problems when the number of layers is varied from one experiment to another. Nevertheless, beside its main disadvantage mentioned in Section 5.5.1, it may exhibit some erroneous results when the layer thickness is not the same for every layers. Anyway, since during the segregation experiments performed in the present work the layer thickness was maintained as regular as possible, and the volume fraction of the material of interest (food material) was by far less than one third, TTSIS was adopted for the description and analysis of the results.

[1] $k_{co,max}$: k_{co} factor imposed maximum value, used for establishing a non-uniform bulk density distribution along the bed (more information in Section 5.5.3)

Table 10.1: Most representative results of the mathematical test of M, "s" index, and TTSIS.

Segr. type imposed	n_{lyr}	$k_{co.max}$	Varied layer and %	M	"s" index	TTSIS			
						p_I	p_M	p_S	$\aleph_2$
Full Top	2	1.000	–	2.00	-0.333	0.000	0.330	0.670	0.670
Full Top	6	1.000	–	2.50	-0.454	0.000	0.000	1.000	1.000
Full Top	10	1.000	–	2.50	-0.473	0.000	0.000	1.000	1.000
Full Top	100	1.000	–	2.50	-0.497	0.000	0.000	1.000	1.000
Full Bottom	2	1.000	–	0.00	1.000	0.670	0.330	0.000	0.670
Full Bottom	6	1.000	–	0.00	5.000	1.000	0.000	0.000	1.000
Full Bottom	10	1.000	–	0.00	9.000	1.000	0.000	0.000	1.000
Full Bottom	100	1.000	–	0.00	99.000	1.000	0.000	0.000	1.000
Full Central	6	1.000	–	0.50	0.000	0.000	1.000	0.000	1.000
Full Central	10	1.000	–	0.00	0.000	0.000	1.000	0.000	1.000
Full Central	100	1.000	–	0.00	0.000	0.000	1.000	0.000	1.000
Pure V	6	1.000	–	1.25	0.000	0.500	0.000	0.500	0.500
Pure V	10	1.000	–	1.25	0.000	0.500	0.000	0.500	0.500
Pure V	100	1.000	–	1.25	0.000	0.500	0.000	0.500	0.500
Pure Uniform	2	1.000	–	1.00	0.000	0.330	0.330	0.330	0.000
Pure Uniform	6	1.000	–	1.00	0.000	0.330	0.330	0.330	0.000
Pure Uniform	10	1.000	–	1.00	0.000	0.330	0.330	0.330	0.000
Pure Uniform	100	1.000	–	1.00	0.000	0.330	0.330	0.330	0.000
Full Top	6	1.025	–	2.50	-0.453	0.000	0.000	1.000	1.000
Full Top	10	1.025	–	2.51	-0.473	0.000	0.000	1.000	1.000
Full Top	100	1.025	–	2.51	-0.497	0.000	0.000	1.000	1.000
Pure Uniform	10	1.050	–	1.01	0.002	0.330	0.330	0.330	0.000
Pure Uniform	100	1.050	–	1.01	0.000	0.330	0.330	0.330	0.000
Full Central	6	1.000	Top +40	0.20	0.067	0.070	0.930	0.000	0.930
Full Central	6	1.000	Central +40	0.70	-0.030	0.050	0.890	0.070	0.840
Full Central	6	1.000	Bottom +40	0.70	-0.058	0.000	0.930	0.070	0.930
Full Central	6	1.025	Central -40	0.30	0.039	0.000	1.000	0.000	1.000
Full Central	6	1.025	Bottom -40	0.30	0.077	0.130	0.870	0.000	0.870

10.2 Segregation of binary mixtures

Figure 10.1(a) shows the segregation level as a function of the air superficial velocity to bran minimum fluidization velocity ratio for mixtures with partially and completely lyophilized material, whereas in Figure 10.1(b) the segregation level as a function of the equivalent fresh product to adsorbent mass ratio is represented. In addition, Table in 10.2 the other TTSIS indices of these experiments are summarized.

Results corresponding to experiments in the L35b with mixtures containing fresh food product are not presented neither in the figures nor the tables since they exhibited Full Bottom segregation independently of air superficial velocity, product volume fraction, or food particle shape.

As it can be seen in Figure 10.1(a), for dried carrot discs (CAa/CAb cases) and dried potato slabs (POd cases) the segregation level increases with air superficial velocity until a peak is reached (which can be assumed between 1.7 and $\approx$ 2.4 u_{mfA}, depending on food material), and then it reduces to relatively low values at 2.6 u_{mfA}. Similarly, in Figure 10.1(b) carrot (CAa) cases show the maximum segregation level at 1.7 u_{mfA} (CAa0170) independently of product concentration. Nevertheless, lyophilized peas (PEa cases) present a completely different behaviour; for these kind of binary mixtures the segregation level is reduced almost linearly as air velocity augments.

About partially lyophilized peas, they have to be maintained in frozen state in order to conserve their structure. This fact makes this material difficult to handle. Anyway, two experimental points were acquired, and it was observed that very high segregation levels where obtained for these experiments. Although the segregation level was reduced with increasing air velocity, it was considered better to stop experimentation with this material, as mixing would not improve significantly.

Besides, it is interesting to remark that segregation levels obtained using binary mixtures containing potato slabs (POd) are considerably greater than values obtained employing mixtures with carrot discs (CAa/CAb), and values presented by mixtures containing peas (PEa/PEc) are notably lower than the other two binary mixtures. Therefore, since the difference in shape factor between carrot discs and peas is about 30 %, and between potato slabs and peas is about 50 %, it can be said that product sphericity plays a very important role on the mixing of these kind of binary mixtures. What is more interesting to note is that, in experiments carried out using POd, holey potato particles were found in the bed bottom (Figure 10.3), meaning that they descended but they could not ascend again due their planar and wide shape. Consequently, potato pieces hit over the bed distributor screw causing their perforation.

Concerning to segregation profiles, as it can be seen in Tables 10.2 and 10.3, in

general experiments at low and middle velocities (1.5-1.9 u_{mfA}) exhibited intermediate cases of Bottom segregation type (Bottom, Bottom Central, Central Bottom, and V-Bottom). At high velocity (2.6 u_{mfA}) nearly Uniform profiles were obtained. In some cases at high velocity according to the classification criteria for segregation type, they are not uniform. However, not only the segregation type should be taken into account for evaluating the mixing, but also the segregation level: despite the segregation profile was not Uniform type, if the segregation level is low (approximately 0.15 or less), the result can be considered uniform to some extent.

As mixtures containing partially lyophilized peas (PEb) concerns, a predominant Bottom segregation and great segregation levels were found. Anyway, air velocity affects this last variable in the same way that in the other cases, reducing it.

Another experiment series where velocity effect was also highlighted was in lyophilized potato slabs (POa) overcoming an induced Top segregation at high air superficial velocity. For these cases, the effect of product weight fraction on segregation is similar to CAa cases.

Regarding to the effect of fluidization time, in Figure 10.2(a) it can be noted that as the time goes on the segregation profile changes from Central Top to Bottom at 1.5 u_{mfA}, and from Central Bottom to Bottom Central at 1.7 u_{mfA}, whereas at 2.6 u_{mfA} the segregation type is Uniform independently of elapsed time. Considering the TTSIS of tracer particles in the figure, at 1.5 u_{mfA} it can be observed that particles initially in bed bottom remained there, while food particles initially in the bed upper third moved toward bed bottom. A similar but less pronounced situation can be noted for cases at 1.7 u_{mfA}. On the contrary, tracer particles at 2.6 u_{mfA} are distributed more uniformly. Thus, two main conclusions can be drawn: first, product particles displacement toward bed bottom prevails at low velocities, and second, the peaks observed in the segregation level at intermediate velocities discussed in previous paragraphs may be only transient situations, prevailing the Bottom segregation trend if fluidization time is increased.

For example, in case CAb0190R20t20 (Table 10.5) it can be seen that while the most part of the bottom tracers remained in the bed bottom, a great part of the top tracers descended to the bed middle and bottom thirds. A more pronounced situation can be noted for POd0150R20t20 and POd0170R20t20 cases, where practically all the bottom tracer remained in the bed bottom, and the greatest part of the top tracer particles were found in the lowest third of the bed.

On the other hand, a different distribution of the tracer particles can be observed for PEc cases being more uniformly distributed than tracers of CAb and POd. That would mean that the V-type of segregation profiles presented by mixtures containing this material might be also a transient stage. Thus, it might be asseverated that they may evolve to Uniform profiles as time goes on.

Unlike other cases where a binary mixture is fluidized in a bubbling fluidized bed and bubbles are the main mixing agent, in channelling fluidized bed the mixing

might be attributed to the shaking of the bed, and channels generation and collapse. Thus, three main types of product particle movement mechanisms can be individuated: passive transport (downward), active transport (upward), and movement blocking. Moreover, the presence and frequency of these mechanisms depends upon air superficial velocity, and they often occur simultaneously in different parts of the bed.

In passive transport, adsorbent material below food particles is dragged by air through channel orifices and deposited on bed surface. Consequently, a downward direction motion of foodstuff takes place as a result of the collapse of the generated void under it. On the opposite, a food particle is actively transported when it is dragged by air and other bran particles through the channels in upward direction.

Additionally, as a result of interaction between adsorbent particles, two main effects causing particle blocking may be identified: floor effect and roof effect. The former is caused by agglomerates of embedded bran particles or more compacted zones avoiding the fall of product particles. The compaction level decreases augmenting air superficial velocity mainly because of a greater motion in the fluidized bed. The latter blocking effect occurs when the path of a food particle is obstructed due to the collapse of a channel wall.

At high velocities (2.3-2.6 u_{mfA}, 0.39-0.44 m/s) pressure release takes place through only one channel of large diameter and bran is thrown high with each explosion, reaching fountain heights of about twice the bed height (as it was presented in Figure 9.2). The Channel Generation and Collapse Cycle repeats at elevated frequencies, and food particles are actively transported by air and moving bran particles. At the same time, due to bed agitation floor effect is practically absent allowing passive transport during channels collapse. Consequently, the lyophilized material uniformly distributes along the bed.

Since at middle velocities (1.7-1.9 u_{mfA}, 0.29-0.32 m/s) about 80 % of bran particle population is experiencing an air superficial velocity greater than its minimum fluidization velocity, the number of channels often increases after a burst by splitting the original one. Though, air velocity inside them seems to be not enough for continuously dragging food material. Furthermore, due to the vibration of bran particles the floor effect is quite reduced and food particles sink. Moreover, during the second stage of the cycle, pressure has been completely released and the number of channels reduces due to collapse of their walls and material depositing over them. Thus, even if a channel were generated at bed bottom, food particles could not ascend due to roof effect. In particular, as it was previously said, in POd cases perforated potato particles were found in the bed bottom. More specifically, case POd0170R40 presented the maximum quantity of damaged food particles (about 44 %) among all experiments using POd. From its segregation profile (TTSIS) and the distribution of the tracer particles, a foodstuff displacement toward bed bottom is observed. Furthermore, perforated particles in the bed bottom prove that there is

a considerable agitation in this part of the bed, but due to roof effects they can not ascend. Therefore, they are damaged hitting with the distributor screw.

At low velocity (1.5 u_{mfA}, 0.25 m/s) one or two small diameter channels are detected. A completely absence of channels in the second stage of the Channel Generation and Collapse Cycle is also possible. As a consequence of this practically lack of shaking, floor and roof effects are notably high avoiding food particles sinking and eventual ascendant movements. Therefore, passive transport prevails causing the foodstuff movement towards bed bottom. Furthermore, the effect of particle shape and size is highlighted at low air superficial velocity. In fact, wide and planar shaped particles (like POd) descend by passive transport, but they can not ascend again in part because of roof effect, and in part due to the fact that particles are not able to enter in channels of small diameter. On the other hand, discs or spherical particles can be eventually actively transported when a channel is generated. Anyway, as it was demonstrated in experiments with 40 minutes of fluidization time (t40 cases), the downward movement prevails as time goes on.

With regard to the effect of food volumetric fraction, no general regular pattern can be observed for all the analysed cases. In CAa and POa, a decrement of the segregation level is manifested with increasing food product volumetric fraction, while in PEa that parameter increases with food material concentration. At high velocity a possible explanation might be formulated taking into account the number of "weak zones" induced by the bigger solid and its shape. In the case of discs, for example, augmenting foodstuff concentration the number of "weak zones" increases resulting in a greater number of channels. In addition, the planar shape and relatively small size might lead to a lower compaction of the material, and thus, passive transport globally compensates active transport resulting in an uniform mixing. On the opposite, spherical particles are actively transported easier than planar ones causing lower segregation levels than discs (as shown in Figure 10.1(b)). Then, the greater concentration, the bigger number of "weak zones", and more quantity of foodstuff particles are actively transported inside the channels.

Finally, Figure 10.2(b) shows a comparison between the L35b (fluidized bed) and the L20spjet (spout-fluid bed). It can be noted that whereas in the L35b the binary mixture is completely segregated for fresh product, the segregation level obtained in experiments performed in the L20spjet are considerably low (below 0.15) for all tested food materials. Moreover, TTSIS results of experiments carried out in the L20spjet (Table 10.4) exhibit a quite uniform distribution. Furthermore, in Table 10.5 it is possible to see that in L20spjet experiments tracer particles (both initially bottom and initially top tracers) exhibit uniform distributions in all the considered cases. These results mean that food material is continuously distributed all along the bed during the fluidization.

From the point of view of the previously mentioned transport mechanisms, the outcomes of experiments in the spout-fluid bed can be explained as follows. In

the L20spjet only a central channel generated by the bed main injector is present, and its walls are constituted by compacted bran deposited by the fountain. Thus, food particles and adsorbent are transported actively in the central channel to bed surface, and passively in downward direction by bran in the annulus. Lateral air injectors avoid product concentration in bed bottom pushing it to the central channel, allowing an accurate mixing of the binary mixture.

Table 10.2: Results in terms of TTSIS for segregation experiments in the L35b and 20 minutes of fluidization time.

Experiment	p_I	p_M	p_S	$\aleph_2$	Segregation type	
POd0260R40t20	0.335	0.186	0.479	0.293	VT	V-Top
POd0170R40t20	0.899	0.101	0.000	0.899	B	Bottom
POd0150R40t20	0.724	0.221	0.055	0.668	B	Bottom
POa0170R80t10	0.185	0.180	0.635	0.455	T	Top
POa0170R40t10	0.253	0.371	0.375	0.122	TC	Top Central
POa0150R80t10	0.000	0.011	0.989	0.989	FT	Full Top
POa0150R40t10	0.000	0.118	0.882	0.882	T	Top
PEb0260R20t20	0.715	0.155	0.129	0.586	B	Bottom
PEb0170R80t20	0.758	0.202	0.040	0.717	B	Bottom
PEa0260R80t20	0.322	0.339	0.339	0.017	U	Uniform
PEa0260R20t20	0.273	0.354	0.372	0.099	TC	Top Central
PEc0230R20t20	0.399	0.274	0.328	0.125	VB	V-Bottom
PEc0190R20t20	0.411	0.255	0.334	0.156	VB	V-Bottom
PEa0150R80t20	0.240	0.371	0.389	0.149	TC	Top Central
PEa0150R20t20	0.274	0.436	0.291	0.162	CT	Central Top
CAa0260R80t20	0.242	0.351	0.407	0.165	TC	Top Central
CAa0260R40t20	0.292	0.336	0.372	0.080	TC	Top Central
CAa0260R20t20	0.305	0.357	0.338	0.053	U	Uniform
CAb0190R20t20	0.544	0.265	0.191	0.354	BC	Bottom Central
CAa0170R80t20	0.612	0.289	0.099	0.513	B	Bottom
CAa0170R40t20	0.567	0.272	0.161	0.407	B	Bottom
CAa0170R20t20	0.299	0.475	0.226	0.249	CB	Central Bottom
CAa0150R80t20	0.091	0.496	0.413	0.405	CT	Central Top
CAa0150R40t20	0.206	0.377	0.417	0.212	TC	Top Central
CAa0150R20t20	0.240	0.430	0.330	0.190	CT	Central Top

Table 10.3: Results in terms of TTSIS for segregation experiments in the L35b and 40 minutes of fluidization time.

Experiment	p_I	p_M	p_S	$\aleph_2$	Segregation type	
CAb0150R20t40	0.682	0.228	0.090	0.591	B	Bottom
CAb0170R20t40	0.521	0.331	0.147	0.374	BC	Bottom Central
CAb0260R20t40	0.313	0.340	0.346	0.033	U	Uniform

Table 10.4: Results in terms of TTSIS for segregation experiments in the L20spjet and 20 minutes of fluidization time.

Experiment	p_I	p_M	p_S	$\aleph_2$	Segregation type	
PEcv1R20L20spjet	0.265	0.330	0.405	0.140	TC	Top Central
PEfv1R20L20spjet	0.292	0.373	0.334	0.081	CT	Central Top
CAdv1R20L20spjet	0.272	0.339	0.389	0.117	TC	Top Central
CAbv1R20L20spjet	0.403	0.298	0.299	0.105	VB	V-Bottom

Table 10.5: Results in terms of TTSIS of tracer particles of segregation experiments presented in Tables 10.2, 10.3, and 10.4.

Experiment	Bottom tracers			Top tracers		
	p_{IB}	p_{MB}	p_{SB}	p_{IT}	p_{MT}	p_{ST}
CAb0190R20t20	0.822	0.072	0.106	0.221	0.464	0.315
POd0150R40t20	0.838	0.157	0.005			
POd0170R40t20	0.937	0.063	0.000	0.829	0.171	0.000
POd0260R40t20	0.402	0.176	0.422	0.079	0.209	0.712
PEc0190R20t20	0.000	0.000	1.000	0.393	0.324	0.283
PEc0230R20t20	0.518	0.204	0.278	0.240	0.292	0.467
CAb0150R20t40	0.950	0.050	0.000	0.609	0.238	0.152
CAb0170R20t40	0.852	0.074	0.074	0.448	0.320	0.232
CAb0260R20t40	0.488	0.315	0.196	0.118	0.444	0.438
PEcv1R20L20spjet	0.326	0.268	0.407	0.211	0.347	0.442
PEfv1R20L20spjet	0.339	0.393	0.268	0.263	0.362	0.375
CAdv1R20L20spjet	0.267	0.327	0.407	0.323	0.359	0.319
CAbv1R20L20spjet	0.564	0.228	0.208	0.309	0.311	0.379

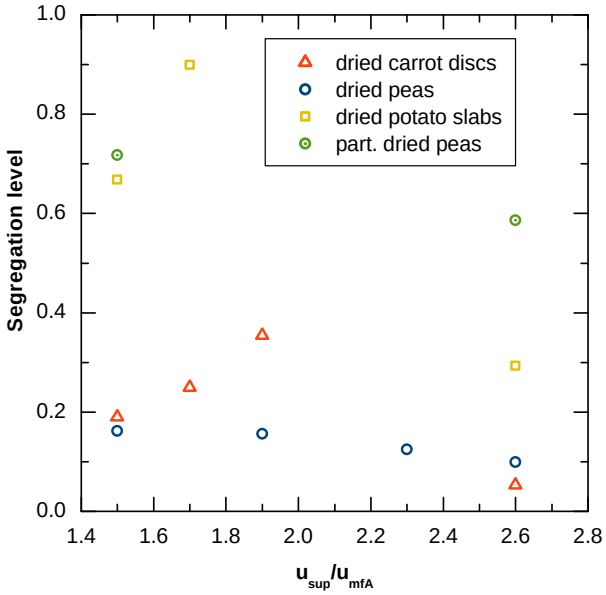

(a) Segregation level as function of air superficial velocity relative to bran mininum fluidization velocity. *20 minutes of fluidization time. Food materials: carrot discs, CAa/CAb; dired peas, PEa/PEc; dried potato slabs, POd; partially dried peas, PEb. Concentrations: R40 for POd-bran mixtures, R20 for the other mixtures*

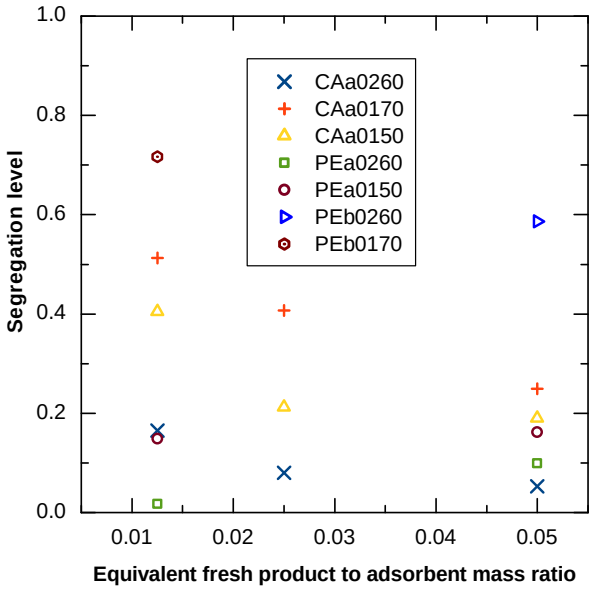

(b) Segregation level in terms of equivalent fresh product to adsorbent mass ratio. *20 minutes of fluidization time.*

Figure 10.1: Effects of air superficial velocity and concentration on segregation in the L35b fluidized bed.

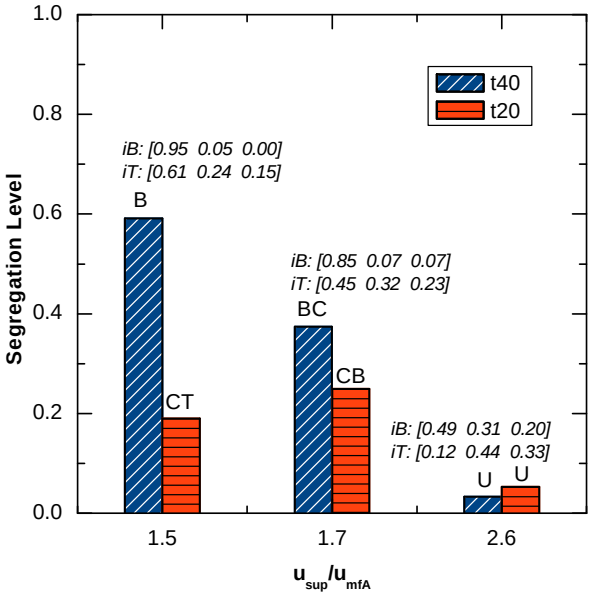

(a) Effect of fluidization time on segregation as a funtion of relative air superficial velocity. *Food materials: lyophilized carrot discs (CAa/CAb). TTSIS for tracer particles correspond to t40 experiments.*

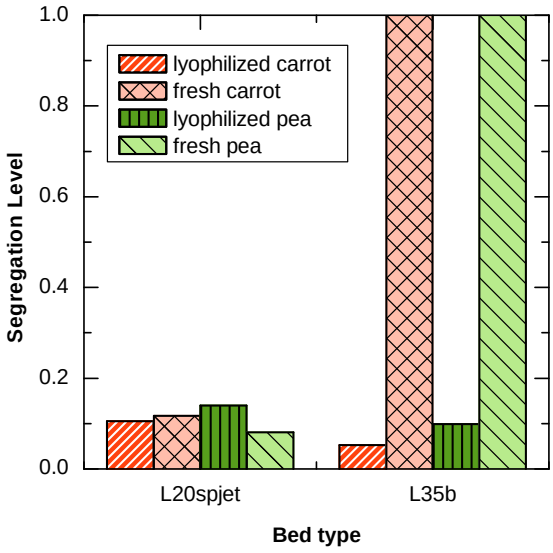

(b) Performance of the fluidized bed (L35b) and the spouted-jet bed (L20spjet) for dried and fresh foodstuff. *20 minutes of fluidization time. Concentration: R20. Air superficial velocity in the L35b: 2.6* u_{mfA}.

Figure 10.2: Fluidization time and performance of two different beds.

Figure 10.3: Holey potato pieces found in bed bottom.

Discussion from the point of view of drag forces

Due to adsorbent characteristics, its particular behaviour for fluidization exhibiting a channel generation and collapse cycle, the segregation phenomena cannot be described at global level by means of a simple force or momentum balance around all the fluidized bed, but a general equation for a single food particle might be formulated. In this equation, the following forces are present:
- Particle weight, due to gravity (ρ_P g).
- Buoyancy force (ρ_{ai} g).
- Drag force (F_D), subdivided in air-FoodProduct drag forces and adsorbent-FoodProduct drag forces (or interaction forces).
- Floor Effect forces whose effect would be similar to the normal force on a surface.
- Hydrostatic pressure of the bed above the particle.

The last three forces are time dependent varying according to what is happening in the surroundings, that is, they depend on the phase of the Channels Generation and Collapse Cycle, air velocity and bran particles moving around the food particle, the depositing adsorbent above, the loosing bran below, etc. From the forces balance of a product particle it can be determined its acceleration and velocity, and from the mean velocity among all product particles the segregation trend can be known.

Thus, a general equation for the food particle can be proposed as follows:

$$\rho_P \frac{d\overrightarrow{u}}{dt} = \rho_P \overrightarrow{g} + \rho_{ai} \overrightarrow{g} + \overrightarrow{F}_{D,ai-P} + \overrightarrow{F}_{D,A-P} + \overrightarrow{N} f_{FE} + a_{Pa} \Delta h \rho_S \overrightarrow{g} \qquad (10.1)$$

if $\overrightarrow{N} = -\rho_P \overrightarrow{g}$ is the normal force and f_{FE} is an "effective surface" factor, the axial components of the preceding equation are:

$$\rho_P \frac{du_z}{dt} = \overbrace{F_{D,ai-P} + F_{D,A-P} + \rho_P g f_{FE} + \rho_{ai} g}^{A} - \overbrace{(\rho_P + a_{Pa}\rho_s \Delta h) g}^{B} \tag{10.2}$$

Therefore, if terms grouped in A are greater than those grouped in B, the food particle will tend to float. Otherwise, it will tend to sink.

10.3 CFD simulations

Figure 10.4 shows the results of CFD simulation of case CAa0260R20, evidencing that neither channels nor its derived effects can be simulated without a specific model for cohesive solids. However, preferential paths for solids circulation can be observed. Moreover, at 2.6 u_{mfA} TTSIS from simulated results is $[0.34\ 0.32\ 0.35]_{0.03}$ which is quite similar to experimental results. Nonetheless, at 1.5 u_{mfA} and 1.7 u_{mfA} TTSIS are, respectively, $[0.34\ 0.32\ 0.35]_{0.03}$ and $[0.31\ 0.32\ 0.38]_{0.07}$, far from experimental results. This discrepancy can be attributed to the fact that blocking effects derived from the pseudo-cohesiveness of the solid are practically absent at high velocities, whereas at lower velocities they should be contemplated by the model.

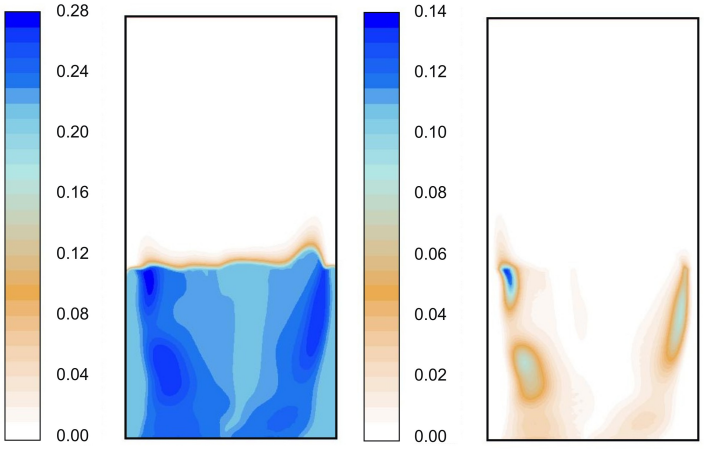

Figure 10.4: Contourplots of volumetric fraction of bran phase (left) and carrot phase (right), simulated case: CAa0260R20

10.4 Summary

Despite some disadvantages, TTSIS was found the best tool for quantifying the segregation phenomenon and classifying the segregation patterns. This set of indexes also minimizes possible experimental errors or the discrepancies caused by applying different experimental procedures. Moreover, it allows the comparison between results obtained utilizing different experimental apparatus. In contrast, M and "s" indexes demonstrated to be affected when experimental procedure is varied although the same segregation case is analysed.

As it was expected from the theory, it was evidenced that, even for a binary mixture composed by a pseudo-cohesive powder and a solid whose particles are considerably greater than the powder ones, the air superficial velocity plays a very important role in mixing. Particularly, at high air flows (2.6 u_{mfA} for the analysed cases) uniform distribution of the material of interest are reached when dried foodstuff is used. Nonetheless, product density plays a fundamental role, since disuniform segregation profiles were obtained when fresh or partially lyophilized food material was used.

Similarly to the segregation mechanisms described by Rowe *et al.* (1972b) for bubbling fluidized beds, two food particle transport mechanisms (passive and active) and two movement blocking effects (floor and roof effects) were proposed. This, together with the Channel Generation and Collapse Cycle described in Chapter 9, permitted to explain the segregation phenomenon in channelling fluidized beds and the mixing process in spout-fluid beds (jet-spouted beds).

Uniform mixing profiles were reached in the spout-fluid bed with a good circulation of the food particles along the bed during the fluidization. These results shown to be independent of the product density. Thus, this kind of bed should be used if an uniform mixing between adsorbent and food product is desired.

Regarding to CFD simulations, relatively reasonable results were obtained from the hydrodynamic point of view only at high air superficial velocity. However, specific models for cohesive or pseudo-cohesive powders are required if an accurate simulation of this kind of solids or binary mixtures integrated by them is intended.

Part IV

General conclusions

Chapter 11

Conlusions

Considering the potential use of non-food wheat bran as adsorbent in the AFD LIAM process, its properties were determined, such as minimum fluidization velocity, population size distribution, or equivalent diameters. Moreover, various food materials were characterized, determining their densities (before and after drying), equivalent diameters, etc. In addition, the fluidization behaviour of the adsorbent was evaluated, classifying it as *pseudo-cohesive*, and conceptually described in the Channels Generation and Collapse General Cycle.

Fluidization of binary mixtures wheat bran-food materials was studied from the point of view of their segregation. For this scope, a new segregation index, the TTSIS, was proposed, allowing the comparison of several binary mixtures under different experimental conditions, and using two experimental apparatus (a fluidized bed, and a spout-fluid bed).

From the results of the experiments mentioned in the previous paragraph, emerged that the fresh product completely segregates toward the bed bottom in fluidized bed when mixtures containing food material without drying were used. Thus, a good contact between the material to be dried and the adsorbent (desirable for utilizing the adsorption heat for ice sublimation) would be not possible for AFD LIAM in fluidized bed applications.

In contrast with the results obtained during the present work, in many cases reported in literature where AFD by immersion in an adsorbent medium in fluidized bed was studied, no segregation was mentioned. However, it should be remarked that in these cases no cohesive solids were generally used as adsorbent, small fluidized beds were employed, and food product was cut in very small pieces when, for example, potato or carrot were utilized.

Using a spout-fluid bed maintains a very good mixing even if disc food particles are used. Thus, beside the already known applications of this kind of beds for catalytic processes, its utilization for AFD LIAM seems to be an interesting and novel option for this process.

Concerning to CFD simulation, from the grid refinement the maximum cell and time step sizes were established for simulations of air fluidized bed of a powder, and a *rule of thumb* relating these properties was determined for further simulations. Additionally, the Gidaspow correlation was found as the optimum model for drag coefficient calculation in systems containing a solid phase and a gaseous phase, and the Gunn's correlation was found accurate for heat exchange. Nevertheless, CFD simulation might be performed only for non-cohesive powders since the simulation of pseudo-cohesive materials fluidization is currently limited because of the lack of hydrodynamic models for this kind of solids.

Another apparent limitation of the CFD simulation is its large computational times, due to the fine grids and time steps required. Thus, long time periods in the order of months may be required for a reasonable simulation of the entire process. However, this situation can be solved by multi-grid or multi-scale simulations combining the CFD results with other models, which consider, for example, the heat and mass exchange of a single food particle.

As future work mainly remains the complete CFD simulation of the Atmospheric Freeze Drying by immersion in an adsorbent medium, in a fluidized bed and in a spout-fluid bed. For accomplishing this scope, intermediate stages of simulation should be passed such as trying to CFD simulate of known cases of AFD LIAM FB (for example, Di Matteo (2002)), and a multi-grid or multi-scale simulation should be considered. Also, from the experimental point of view, the freeze drying of food using non-food wheat bran as adsorbent in the spout-fluid bed should be tried and compared with other AFD techniques.

A possibility for CFD modelling and simulating the process may be by means of the following steps:

I. Considering cases from Di Matteo (2002) and using two solid phases (food product and adsorbent), and one gaseous phase (air):
    1. Considering the Eulerian-Eulerian approach, implement the URIF model for the food product phase and the sorption isotherms for the adsorbent phase. These implementations can be done by means of user customized functions (UDF, for the case of ANSYS Fluent), and the mass and heat exchange derived from the particle and adsorbent models might be hooked into the solver as source terms.
    2. Test the models with coarse simulations.
    3. Investigate the possibility of using multi-grid simulation, applying a fine grid for the velocity field and a coarser grid for the mass and heat exchange simulations.

II. Modelling and simulation of a pseudo-cohesive solid.
    1. Develop a mathematical model for simulating a pseudo-cohesive solid (the approach may be similar to van Wachem and Sasic (2008)).

2. After simulating the spout-fluid bed for known cases (non-cohesive materials), implement the model for pseudo-cohesive solids.
3. Combine the models developed in I. with the pseudo-cohesive model in the spout-fluid bed.

Nomenclature

Upper-case Roman

A	area	m^2
A_{pu}	particle projected area on a plane normal to the motion direction	m^2
Ar_P	Archimedes number of a sphere	
Ar_V	Archimedes number of a sphere having the same volume of a particle	
C_D	drag coefficient for a particle in a suspension	
C_{Ds}	drag coefficient for a particle falling in an infinite fluid	
C_w	maximum water content	kg_w/kg_s
D_{eff}	effective diffusivity	m^2 / s
D_w	vapor diffusivity in the dry layer	m^2 /s
F_D	drag force	N
F_E	buoyancy force of a fluid acting on a particle	N
F_q	accumulated mass of material of interest q from the bottom	
GCI_{21}	Grid Convergence Index between two grids	[considered variable]
$\hat{H}$	specific enthalpy	J/kg
L	bed height	m
M	mixing index based on *jetsam* fractions defined in Section 3.5.1	
M_i	molar mass of phase i	kg/mol
P	pressure	Pa

$\vec{P}_{dis}$	mass distribution vector	-
P_w	water partial pressure	Pa
R	universal gas constant	J/(mol K)
Re	Reynolds number. Subscripts explained in Section 4.2.2	
S_i	source term in mass conservation equation	kg/m^3
S_P	particle surface	m^2
V_{beaker}	beaker volume	m^3
V_{cell}	cell volume	m^3
V_P	particle volume	m^3
X	moisture content in dry basis	kg$_w$/kg$_{dry}$
X^*	moisture content in dry basis at the 7th hour	kg$_w$/kg$_{dry}$
X_J	jetsam fraction in upper part of the bed	
Z	moisture content	%
Z_{eq}	equilibrium moisture content (at $t = \infty$)	%

Lower-case Roman

d_{eq}	equivalent diameter for fluidization (EDF)	m
d_S	diameter of a sphere having the same surface than the particle	m
d_{SV}	Sauter's diameter	m
d_V	diameter of a sphere having the same volume than the particle	m
e_s	dry layer thickness	m
f_1, f_2	value of the variable for the finer and the coarser grids	[considered variable]
g	gravity acceleration	m/s^2
h_{bed}	total bed height in settled state	m
$\vec{h}_{dis}$	thickness distribution vector	
h_{ex}	external heat transfer coefficient	W/(m^2 K)

$\hat{i}$	specific internal energy	J/kg
k_1, k_2	coefficients of the viscous and energy term, respectively (equation 4.23)	
k_{co}	solids bulk density variation factor	
k_s	dry layer thermal conductivity	W/(m K)
m_A	mass of adsorbent	kg
m_{A+w}	mass of adsorbent and water	kg
m_{ij}	mass exchange between phases i and j	kg/m^3
m_P	mass of product	kg
m_{P0},m_{P1}	mass of product before and after lyophilization, respectively	kg
m_{Pw0}	initial mass of water in the product	kg
m_{si}	total mass of solids in layer i	kg
m_{sT}	total mass of solids in all the bed	kg
$\check{n}$	unitary vector normal to a surface	
n	Richardson and Zaki exponent	
n_{lyr}	number of layers	#
n_P	number of particles per unit of total volume	particles/m^3
p	in GCI estimation, formal order of accuracy of the algorithm	-
p_I	Bottom Third Indicator, in TTSIS	-
p_M	Middle Third Indicator, in TTSIS	-
p_S	Top Third Indicator, in TTSIS	-
r_{21}	refinement factor between coarse and fine grid	-
s	segregation index defined in Section 3.5.1	
u_{sup}	fluid superficial velocity magnitude	m/s
$\vec{u}_i$	phase i velocity	m/s
u_t	magnitude of particle terminal velocity	m/s

$\vec{v}_i$	phase i velocity	m/s
w_w	water weight fraction	-
x_w^*	remaining fraction of initial mass of water in product	

Upper-case Greek

Γ	generic diffusivity of property ϕ	
Δh_i	layer i thickness	m
$\Delta \hat{H}_{sv}$	latent heat of sublimation	J/kg
ΔP	pressure drop	Pa
$\Delta \vec{v}_{ij}$	slip velocity between phases i and j, $\Delta \vec{v}_{ij} = \vec{v}_i - \vec{v}_j$	m/s
Φ	component of total flow vector in the direction normal to a surface	

Lower-case Greek

$\alpha_{A,max}$	maximum packaging limit of adsorbent	-
α_i	volumetric fraction of phase i	-
β_{ex}	external mass transfer coefficient	m/s
γ_s	safety factor in GCI	-
μ	fluid viscosity	Pa.s
ρ_{abs}	absolute density	kg/m^3
ρ_b	bulk density	kg/m^3
ρ_i	density of phase i	kg/m^3
$\rho_{P_{lyo}}$,$\rho_{P_{fresh}}$	density of lyophilized and fresh product, respectively	kg/m^3
ϕ	generic transported fluid property	
ϕ_{ML}	Mazzei and Lettieri's drag force corrective factor	

Others

$\aleph_2$	segregation level	-

Subscripts

$_A$	adsorbent	-
$_{ai}$	air	-
$_{cc}$	cell center	
$_F$	face F of a control volume (CV)	
$_f$	fluid property	-
$_{fr}$	ice front	
$_P$	food product	-
$_p$	disperse phase (or particle when only a single particle is involved)	-
$_{sup}$	superficial (used for defining Reynolds number using u_{sup})	-
$_T$	total	-

Special operators

$\langle\ \rangle$	volumetric mean
$\|\|\ \|\|$	vector modulus

Bibliography

Alves-Filho O. (2010), "Sweep numerical method and mass transport analysis in atmospheric freeze drying of protein particles." *Heat Mass Transfer*, **46**, 923–928.

Alves-Filho O. and Goncharova-Alves S. (2012), "Modeling heat pump drying: from pilot scale to commercial plant." In *18th International Drying Symposium (IDS2012),* Xiamen, China, 11-15 November 2012.

ANSYS (2010), *ANSYS Fluent 13 Theory Guide.* ANSYS, Inc. Southpointe, Canonsburg (PA) USA.

Asegehegn T., Schreiber M. and Krautz H. J. (2012), "Influence of two- and three-dimensional simulations on bubble behavior in gas-solid." *Powder Technology*, **219**, 9–19.

Bantle M. and Eikevik T. M. (2011), "Parametric study of high-intensity ultrasound in the atmospheric freeze drying of peas." *Drying Technology*, **29**, 1230–1239.

Barresi A., Pagliolico S. and Pipino M. (1996), "Mixing of slurries in a static mixer: Evaluation of a lower energy alternative to simultaneous comminution and mixing for production of composite ceramic materials." In *Fifth International Conference of Multiphase Flow in Industrial Plants,* Amalfi (Italy), 26-27 September 1996 (ANIP, ed.), 302–313.

Bi H. T. (2007), "A critical review of the complex pressure fluctuation phenomenon in gas–solids fluidized beds." *Chemical Engineering Science*, **62(13)**, 3473–3493.

Boeh-Ocansey O. (1985), "Some factors influencing the freeze drying of carrot discs in vacua and at atmospheric pressure." *Journal of Food Engineering*, **4**, 229–243.

Bubnovich V., Reyes A., Quijada E. and Mahn A. (2012), "Numerical simulation of lyophilization of carrot slices at atmospheric pressure in a fluidized bed." *Journal of Food Engineering*, **109**, 659–667.

Bustos R., Vásquez M., Vega R., Reyes A., Bubnovich V. and Scheuermann E. (2010), "Comparative study of different process conditions of freeze drying of 'murtilla' berry." *Drying Technology*, **28**, 1416–1425.

Chew J. and Hrenya C. (2011), "Link between bubbling and segregation patterns in gas-fluidized beds with continuous size distributions." *AIChE Journal*, **57**, 3003–3011.

Claussen I., Ansressen T., Eikevik T. and Strømmen I. (2007a), "Atmospheric freeze drying - Modeling and simulation of a tunnel dryer." *Drying Technology*, **25**, 1959–1965.

Claussen I., Ustad T., Strømmen I. and Walde P. (2007b), "Atmospheric Freeze Drying - A Review." *Drying Technology*, **25:6**, 947–957.

Cooke M. and Bridgewater J. (1977), "A distribution index and its applications to static powder mixers." In *Second European Conference on Mixing,* 30th March-1st April 1977, St. John's College, Cambridge, England (B. F. Engineering, ed.), D3.27–D3.35.

Di Matteo P. (2002), *Sviluppo di un processo per la liofilizzazione a pressione atmosferica di sostanze alimentari*. Ph.D. thesis, Università degli Studi di Salerno.

Donsì G., Di Matteo P. and Ferrari G. (2003), "The role of heat and mass transfer phenomena in atmospheric freeze-drying of foods in a fluidised bed." *Journal of Food Engineering*, **59**, 267–275.

Donsì G., Ferrari G. and Di Matteo P. (2001), "Utilization of combined processes in freeze-drying of shrimps." *Transactions of the Institution of Chemical Engineers*, **79**, 152–159.

Eikevik T. M., Alves-Filho O. and Bantle M. (2012), "Microwave-assisted atmospheric freeze drying of green peas: A case of study." *Drying Technology*, **30**, 1592–1599.

Ergun S. (1952), "Fluid flow through packed colums." *Chemical Engineering Progress*, **48(2)**, 89–94.

Esmaili E. and Mahinpey N. (2011), "Adjustment of drag coefficient correlations in three dimensional CFD simulation of gas-solid bubbling fluidized bed." *Advances in Engineering Software*, **42**, 375–386.

Fan L., Chen S. and Watson C. (1970), "Solids mixing." *Industrial and Engineering Chemistry*, **62**, 53–69.

Ferziger J. H. and Perić M. (2002), *Computational Methods for Fluid Dynamics*, third rev. edition. Springer-Verlag, Germany.

Geldart D. (1973), "Types of Gas Fluidization." *Powder Technology*, **7**, 285–292.

Geldart D., Harnby N. and Wong A. (1984), "Fluidization of cohesive powders." *Powder Technology*, **31(1)**, 25–37.

Gibilaro L. and Rowe P. (1974), "A model fo a segregationg gas fluidised bed." *Chemical Engineering Science*, **29**, 1403–1412.

Gidaspow D. (1986), "Hydrodinamics of fluidization and heat transfer: Supercomputer modeling." *Applied mechanics review*, **39(1)**, 1–23.

Gidaspow D. (1994), *Multiphase flow and fluidization: Continuum and kinetic theory descriptions*, first edition. Academic Press, Inc., San Diego CA, USA.

Gidaspow D., Jung J. and Singh R. (2004), "Hydrodynamics of fluidizarion using kinetic theory: an emerging paradigm: 2002 Flour-Daniel lecture." *Powder Technology*, **148**, 123–141.

Gunn D. (1978), "Transfer of heat or mass to particle in fixed and fluidized beds." *International Journal of Heat and Mass Transfer*, **21**, 467–476.

Jiradilok V., Gidaspow D., Damrongled S., Koves W. and Mostofi R. (2006), "Kinetic theory based CFD simulation of turbulent fluidization of FCC particles in a riser." *Chemical Engineering Science*, **61**, 5544–5559.

Jung J., Gidaspow D. and Gamwo I. K. (2006), "Bubble computation, granular temperatures, and Reynolds stresses." *Chemical Engineering Communications*, **8**, 946–975.

Kolsaker K., Bantle M. and Eikevik T. (2011), "Modification of the Weibull distribution for modeling atmospheric freeze-drying of food." *Drying Technology*, **29**, 1161–1169.

Kunii D. and Levenspiel O. (1991), *Fluidization Engineering*, second edition. Butterworth-Heinmann, Newton MA, USA.

Link J., Cuypers L., Deen N. and Kuipers J. (2005), "Flow regimes in a spout–fluid bed: A combined experimental and simulation study." *Chemical Engineering Science*, **60(13)**, 3425–3442.

Loha C., Chattopadhyay H. and Chatterjee P. K. (2012), "Assessment of drag models in simulating bubbling fluidized bed hydrodynamics." *Chemical Engineering Science*, **75**, 400–407.

Lombraña J. and Villarán M. (1997), "The influence of pressure and temperature on freeze-drying in an adsorbent medium and establishment of drying strategies." *Food Research International*, **30(3/4)**, 213–222.

Malek M., Benjamin C. and Lu Y. (1965), "Pressure drop and spoutable bed height in spouted beds." *I&EC Process Desing and Development*, **4**, 123–128.

Mazzei L. and Lettieri P. (2007), "A drag force clousure for uniformly dispersed fluidized suspensions." *Chemical Engineering Science*, **62**, 6129–6142.

Mellema S., Kuipers J., Link J. and Goldschmidt M. (2003), "Digital image analysis measurements of bed expansion and segregation dynamics in dense gas-fluidised beds." *Powder Technology*, **138**, 135–159.

Menshutina N., Korneeva A. and Leuenberger H. (2005), "Modeling of atmospheric freeze drying in a spouted bed." *Theoretical Foundations of Chemical Engineering*, **39**, 594–598.

Nam J. and Song C. (2007), "Numerical simulation of conjugate heat and mass transfer during multi-dimensional freeze drying of slab-shaped food products." *International Journal of Heat and Mass transfer*, **50**, 4891–4900.

Patiño-Palacios G., Rocha-Uribe J. and Flores-Prent L. A. (2010), "Gas and particles flow in a fluidized bed using computational fluids dynamics. Application to catalytic cracking." *Tecnología, Ciencia, Educación*, **1**, 44–52.

Pérez N., Reyes A. and Mahn A. (2011), "Theoretical and experimental study of freeze-drying of "loco" (Concholepas concholepas)." *Drying Technology*, **29(12)**, 1386–1395.

Petrila T. and Trif D. (2005), *Basics of fluid mechanics and introduction to computational fluid dynamics*, first edition. Springer, USA.

Poux M., Fayolle P., Berttrand J., Bridoux D. and Bousquet J. (1991), "Powder mixing: some practical rules applied to agitated systems." *Powder Technology*, **68**, 213–234.

Qiaoquna S., Huilina L., Wentiea L., Yuronga H., Lidana Y. and Gidaspow D. (2005), "Simulation and experiment of segregating/mixing of rice husk-sand mixture in a bubbling fluidized bed." *Fuel*, **84**, 1739–1748.

Quijada E., Bubnovich V. and Reyes A. (2009), "Computer simulation of atmospheric freeze drying of carrot slices in a fluidized bed." *Numerical Heat Transfer, Part A*, **56**, 170–191.

Rasetto V., Marchisio D. L., Fissore D. and Barresi A. A. (2010), "On the use of a dual-scale model to improve understanding of a pharmaceutical freeze-drying process." *Journal of Pharmaceutical Sciences*, **99**, 4337–4350.

Ratti C. (2001), "Hot air and freeze-drying of hight-value foods: a review." *Journal of Food Engineering*, **49**, 311–319.

Reyes A., Mahn A. and Huenulaf P. (2011), "Drying of apple slices in atmospheric and vacuum freeze dryer." *Drying Technology*, **29**, 1076–1089.

Richardson J. and Zaki W. (1954), "Sedimentation and fluidisation: Part I." *Transactions of the Institution of Chemical Engineers*, **32**, 35–53.

Roache P. (1997), "Quantification of uncertainty in computational fluid dynamics." *Annual Review of Fluid Mechanics*, **29**, 123–160.

Rowe P., Nienow A. and Agbim A. (1972a), "A preliminary quantitative study of particle segregation in gas fluidised beds - binary sustems of near spherical particles." *Transactions of the Institution of Chemical Engineers*, **50**, 324–333.

Rowe P., Nienow A. and Agbim A. (1972b), "The mechanisms by which particles segregate in gas fluidised beds - binary systems of near-spherical particles." *Transactions of the Institution of Chemical Engineers*, **50**, 310–323.

Sahoo P. and Sahoo A. (2013), "Fluidization and spouting of fine particles: A comparison." *Advances in Materials Science and Engineering*, **2013**, 1–7. Article ID 369380.

Stawczyk J., Li S. and Zbicinski I. (2007), "CFD Model of apple atmospheric freeze drying at low temperature." *Drying Technology*, **25**, 1331–1339.

Strømmen I., Alves-Filho O. and Eikevik T. (2005), "Atmospheric freeze drying with heat pumps - A new alternative for high quality dried food products." *3rd Nordic Drying Conference, June 15th to 17th, 2005, Karlstad, Sweden.*

Sundaresan S. (2003), "Instabilities in fluidized beds." *Annual Review of Fluid Mechanics*, **35**, 63–88.

Sutanto W. (1981), *Hydrodynamics of spout fluid beds.* Ph.D. thesis, University of British Columbia.

van Wachem B. and Sasic S. (2008), "Derivation, simulation and validation of a cohesive particle flow CFD model." *AIChe Journal*, **54**, 9–19.

Vejahati F., Mahinpey N., Ellis N., Nikoo M. B. *et al.* (2009), "CFD simulation of gas-solid bubbling fluidized bed: A new method for adjusting drag law." *Canadian Journal of Chemical Engineering*, **87**, 19–30.

Versteeg H. and Malalasekera W. (1995), *An introduction to computational fluid dynamics - The finite volume method*, first edition. Longman Scientific & Technical, Burnt Mill, Harlow, England.

Visser J. (1989), "Van der Waals and other cohesive forces affecting powder fluidization." *Powder Technology*, **1**, 1–10.

Wang S., Zhao L., Wang C., Liu Y., Gao J., Liu Y. and Cheng Q. (2014), "Numerical simulation of gas–solid flow with two fluid model in a spouted-fluid bed." *Particuology*, **14**, 109–116.

Wen C. and Yu Y. (1966), "Mechanics of Fluidization." *Chemical Engineering Progress Symposium Series*, **62**, 100–111.

Witrowa-Rajchert D., Stawczyk J., Li S. and Fabisiak A. (2007), "Kinetics of atmospheric freeze-drying of apple." *Transport Porous Media*, **66**, 159–172.

Wolff E. and Gibert H. (1990), "Atmospheric freeze-drying part 2: modeling drying kinetics using adsorption isotherms." *Drying Technology*, **2**, 405–428.

Wu S. and Baeyens J. (1998), "Segregation by size difference in gas fluidized beds." *Powder Technology*, 139–150.

Zhang J. and Tang F. (2006), "Prediction of flow regimes in spout-fluidized beds." *China Particuology*, **4**, 189–193.

Zhong W., Chen X. and Zhang M. (2006a), "Hydrodynamic characteristics of spout-fluid bed: Pressure drop and minimum spouting/spout-fluidizing velocity." *Chemical Engineering Journal*, **118**, 37–46.

Zhong W., Zhang M., JIN B. and Yuan Z. (2006b), "Three-dimensional simulation of gas/solid flow in spout-fluid beds with kinetic theory of granular flow." *Chinese Journal of Chemical Engineering*, **14**, 611–617.

Appendices

Appendix A

Further tables and figures

A.1 TTSIS - Bands for the classification of segregation patterns

Table A.1: Adopted criteria for the segregation patterns classification.

	p_I	p_M	p_S	*and* (other conditions)	*then,* Segregation type is:	
if	0.33	0.33	0.33	-	U	Pure Uniform
else if	0.33 ± 0.03	0.33 ± 0.03	0.33 ± 0.03	-	U	Uniform
else if	≥ 0.98	-	-	-	FB	Full Bottom
else if	$0.55 \leq p_I < 0.98$	-	-	$p_S - p_M < 0.14$	B	Bottom
else if	-	≥ 0.98	-	-	FC	Full Central
else if	-	$0.55 \leq p_M < 0.98$	-	-	C	Central
else if	-	-	≥ 0.98	-	FT	Full Top
else if	-	-	$0.55 \leq p_S < 0.98$	$p_I - p_M < 0.14$	T	Top
else if	$0.47 \leq p_I < 0.54$	-	$0.47 \leq p_S < 0.54$	-	V	Pure V
else if	$> p_M$	-	$> p_M$ and $> p_I$	-	VT	V-Top
else if	$> p_M$ and $> p_S$	-	$> p_M$	-	VB	V-Bottom
else if	-	$p_I < p_M < p_S$	-	-	TC	Top Central
else if	-	$p_I > p_M > p_S$	-	-	BC	Bottom Central
else if	-	-	$p_M > p_S > pI$	-	CT	Cental Top
else if	$p_M > p_I > p_S$	-	-	-	CB	Central Bottom

This criteria was implemented by means of a computational code in Python. The bands adopted for the classification of the different segregation types were arbitrary fixed on the basis of several experimental experiences. Therefore, if a rapid idea about the distribution of the product of interest along the bed and the segregation degree is wanted, knowing the Segregation Level ($\aleph_2$) and the Segregation Type is enough.

A.2 Theoretical test of segregation indexes: Complete results

Table A.2: Mathematical test of segregation indexes. Results for cases where only the number of vacuumed layers was varied.

Segr. type imposed	n_{lyr}	M	"s" index	TTSIS			
				p_I	p_M	p_S	$\aleph_2$
Full Top	2	2.00	-0.333	0.000	0.330	0.670	0.670
Full Top	6	2.50	-0.454	0.000	0.000	1.000	1.000
Full Top	10	2.50	-0.473	0.000	0.000	1.000	1.000
Full Top	100	2.50	-0.497	0.000	0.000	1.000	1.000
Full Bottom	2	0.00	1.000	0.670	0.330	0.000	0.670
Full Bottom	6	0.00	5.000	1.000	0.000	0.000	1.000
Full Bottom	10	0.00	9.000	1.000	0.000	0.000	1.000
Full Bottom	100	0.00	99.000	1.000	0.000	0.000	1.000
Full Central	6	0.50	0.000	0.000	1.000	0.000	1.000
Full Central	10	0.00	0.000	0.000	1.000	0.000	1.000
Full Central	100	0.00	0.000	0.000	1.000	0.000	1.000
Pure V	6	1.25	0.000	0.500	0.000	0.500	0.500
Pure V	10	1.25	0.000	0.500	0.000	0.500	0.500
Pure V	100	1.25	0.000	0.500	0.000	0.500	0.500
Pure Uniform	2	1.00	0.000	0.330	0.330	0.330	0.000
Pure Uniform	6	1.00	0.000	0.330	0.330	0.330	0.000
Pure Uniform	10	1.00	0.000	0.330	0.330	0.330	0.000
Pure Uniform	100	1.00	0.000	0.330	0.330	0.330	0.000

Table A.3: Mathematical test of segregation indexes. Results varying the number of layers and/or layers solids bulk density.

Segr. type imposed	n_{lyr}	$k_{co,max}$	M	"s" index	TTSIS			
					p_I	p_M	p_S	$\aleph_2$
Full Top	6	1.025	2.50	-0.453	0.000	0.000	1.000	1.000
Full Top	10	1.025	2.51	-0.473	0.000	0.000	1.000	1.000
Full Top	100	1.025	2.51	-0.497	0.000	0.000	1.000	1.000
Full Bottom	6	1.025	0.00	5.011	1.000	0.000	0.000	1.000
Full Bottom	10	1.025	0.00	9.010	1.000	0.000	0.000	1.000
Full Bottom	100	1.025	0.00	99.008	1.000	0.000	0.000	1.000
Full Central	6	1.025	0.50	0.002	0.000	1.000	0.000	1.000
Full Central	10	1.025	0.00	0.001	0.000	1.000	0.000	1.000
Full Central	100	1.025	0.00	0.000	0.000	1.000	0.000	1.000
Pure Uniform	6	1.025	1.00	0.002	0.330	0.330	0.330	0.000
Pure Uniform	10	1.025	1.00	0.001	0.330	0.330	0.330	0.000
Pure Uniform	100	1.025	1.00	0.000	0.330	0.330	0.330	0.000
Pure Uniform	6	1.050	1.00	0.003	0.330	0.330	0.330	0.000
Pure Uniform	10	1.050	1.01	0.002	0.330	0.330	0.330	0.000
Pure Uniform	100	1.050	1.01	0.000	0.330	0.330	0.330	0.000
Full Bottom	6	1.050	0.00	5.020	1.000	0.000	0.000	1.000
Full Bottom	10	1.050	0.00	9.018	1.000	0.000	0.000	1.000
Full Bottom	100	1.050	0.00	99.016	1.000	0.000	0.000	1.000

Table A.4: Mathematical test of segregation indexes. Results varying layers thickness, and/or number of layers, and/or layers solids bulk density.

Segr. type imposed	n_{lyr}	$k_{co.max}$	Varied layer and %	M	"s" index	TTSIS			
						p_I	p_M	p_S	$\aleph_2$
Full Top	6	1.000	Top +40	2.50	-0.438	0.000	0.000	1.000	1.000
Full Top	6	1.000	Central +40	2.50	-0.457	0.000	0.000	1.000	1.000
Full Top	6	1.000	Bottom +40	2.50	-0.457	0.000	0.000	1.000	1.000
Full Top	10	1.000	Top +40	2.50	-0.463	0.000	0.000	1.000	1.000
Full Top	10	1.000	Central +40	2.50	-0.474	0.000	0.000	1.000	1.000
Full Top	10	1.000	Bottom +40	2.50	-0.474	0.000	0.000	1.000	1.000
Full Bottom	6	1.000	Top +40	0.00	5.400	1.000	0.000	0.000	1.000
Full Bottom	6	1.000	Central +40	0.00	5.400	1.000	0.000	0.000	1.000
Full Bottom	6	1.000	Bottom +40	0.00	3.571	1.000	0.000	0.000	1.000
Full Bottom	10	1.000	Top +40	0.00	9.400	1.000	0.000	0.000	1.000
Full Bottom	10	1.000	Central +40	0.00	9.400	1.000	0.000	0.000	1.000
Full Bottom	10	1.000	Bottom +40	0.00	6.429	1.000	0.000	0.000	1.000
Full Central	6	1.000	Top +40	0.20	0.067	0.070	0.930	0.000	0.930
Full Central	6	1.000	Central +40	0.70	-0.030	0.050	0.890	0.070	0.840
Full Central	6	1.000	Bottom +40	0.70	-0.058	0.000	0.930	0.070	0.930
Full Central	10	1.000	Top +40	0.00	0.040	0.000	1.000	0.000	1.000
Full Central	10	1.000	Central +40	0.20	-0.018	0.000	1.000	0.000	1.000
Full Central	10	1.000	Bottom +40	0.20	-0.037	0.000	1.000	0.000	1.000
Full Central	6	1.000	Top -40	0.80	-0.066	0.000	0.870	0.130	0.870
Full Central	6	1.000	Central -40	0.30	0.037	0.000	1.000	0.000	1.000
Full Central	6	1.000	Bottom -40	0.30	0.077	0.130	0.870	0.000	0.870
Full Central	6	1.025	Central -40	0.30	0.039	0.000	1.000	0.000	1.000
Full Central	6	1.025	Bottom -40	0.30	0.077	0.130	0.870	0.000	0.870

A.3 Comparison between M mixing index and TTSIS for experimental cases

In Table A.5 are presented the M index calculated for the experimental cases exposed in Chapter 10, recalling also their Segregation Levels ($\aleph_2$) and segregation types from their TTSIS results. In general terms, it can be seen that as $\aleph_2$ increases, the value of M distances from the unity. Moreover, values greater than 1 for M index in cases with top segregating tendency (FT, T, TC, and CT) can be noted. This situation can be easily explained from the point of view of the index definition (Section 3.5.1): it was defined assuming concentrations of the so-called *jetsam* in the bed top zones lower than the overall *jetsam* concentration. In this case, since this mixing index was used for measuring the mixing level of a particular component of interest (no matter if it tends to float or sink), the foodstuff concentration in the bed upper part is greater than the total concentration of product in all the bed for top-like segregation patterns.

All these results of M index may lead to think that by comparing it with TTSIS for experimental results, a correlation between both might be established and the segregation profiles might be identified also with the M index. Nevertheless, beside the cons found in the mathematical test of indexes (Section 10.1) for the M index (such as it is not able for identifying V-Segregation profile), other inconsistencies can be observed when the mixing of foodstuff and non-food wheat bran binary mixtures are analyzed. For example, considering cases PEa0150R20t20 and CAb0260R20t40, their segregation level and profiles are, respectively, 0.162-CT and 0.033-U, whereas the M index values are 1.01 and 1.09. According with M index definition, the case PEa0150R20t20 should be better mixed than case CAb0260R20t40, which is clearly not true.

Table A.5: M mixing index and resumed TTSIS ($\aleph_2$ and segregation type).

	M	TTSIS	
		$\aleph_2$	Type
POd0260R40t20	1.32	0.293	VT
POd0170R40t20	0.02	0.899	B
POd0150R40t20	0.17	0.668	B
POa0170R80t10	1.72	0.455	T
POa0170R40t10	1.12	0.122	TC
POa0150R80t10	2.49	0.989	FT
POa0150R40t10	2.34	0.882	T
PEb0260R20t20	0.39	0.586	B
PEb0170R80t20	0.18	0.717	B
PEa0260R80t20	1.00	0.017	U
PEa0260R20t20	1.10	0.099	TC
PEc0230R20t20	0.96	0.125	VB
PEc0190R20t20	0.97	0.156	VB
PEa0150R80t20	1.21	0.149	TC
PEa0150R20t20	1.01	0.162	CT
CAa0260R80t20	1.21	0.165	TC
CAa0260R40t20	1.09	0.080	TC
CAa0260R20t20	1.02	0.053	U
CAb0190R20t20	0.63	0.354	BC
CAa0170R80t20	0.36	0.513	B
CAa0170R40t20	0.57	0.407	B
CAa0170R20t20	0.90	0.249	CB
CAa0150R80t20	1.36	0.405	CT
CAa0150R40t20	1.21	0.212	TC
CAa0150R20t20	1.12	0.190	CT
CAb0260R20t40	1.09	0.033	U
CAb0170R20t40	0.54	0.374	BC
CAb0150R20t40	0.34	0.591	B
PEcv1R20L20spjet	1.18	0.140	TC
PEfv1R20L20spjet	1.03	0.081	CT
CAdv1R20L20spjet	1.15	0.117	TC
CAbv1R20L20spjet	0.89	0.105	VB

A.4 Pressure drop versus velocity simulated curves

The following figures represent the simulated results of pressure drop versus velocity used for the estimation of the minimum fluidization velocity by means of simulation (described in Section 6.3 and discussed in Chapter 7).

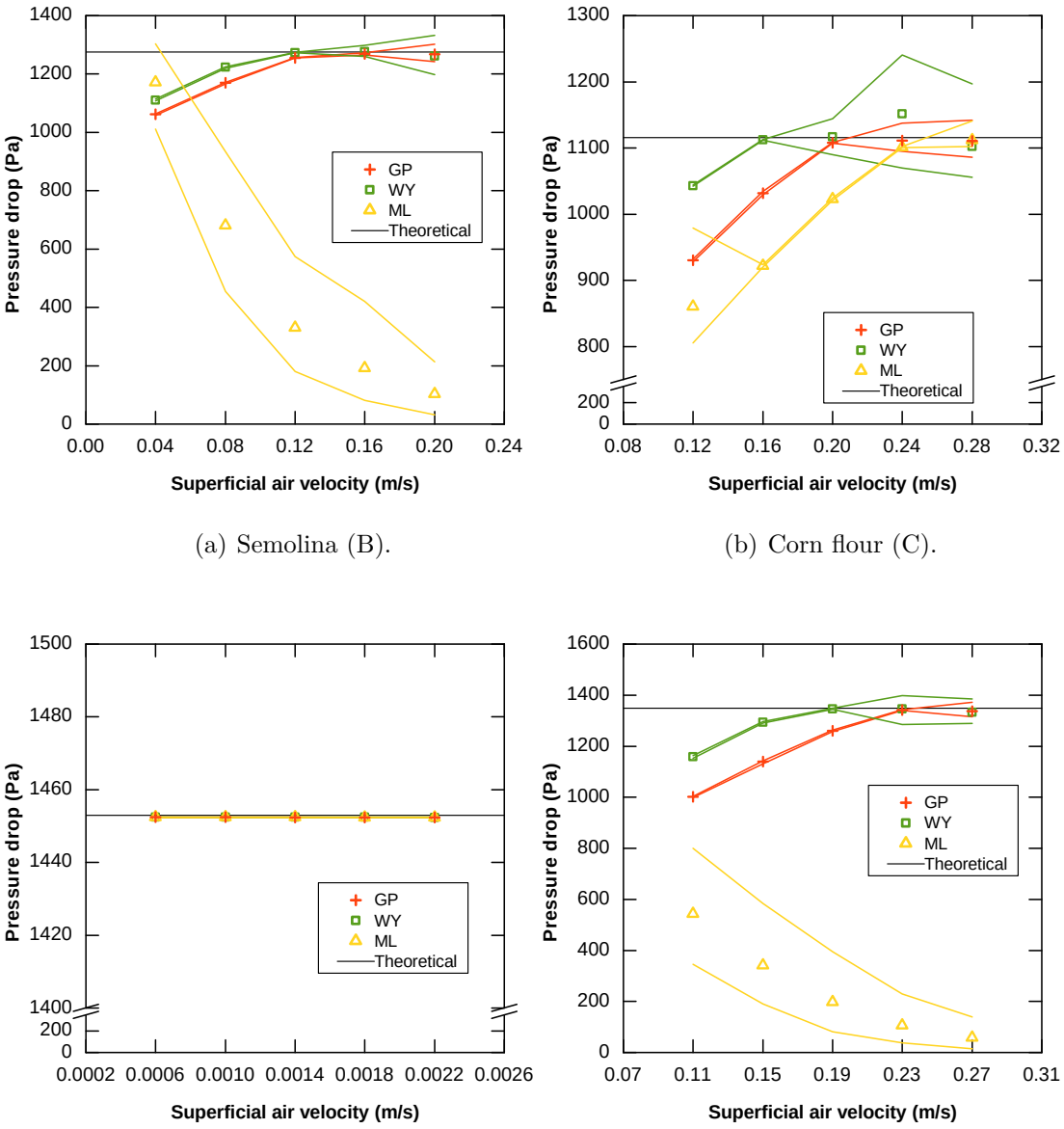

(a) Semolina (B).

(b) Corn flour (C).

(c) Starch (S).

(d) Zeolites (Z).

Figure A.1: Simulated pressure drop versus velocity curves. (GP: Gidaspow's model, WY: Wen and Yu's model, ML: Mazzei and Lettieri's model). The solid lines represent the maximum and minumum values reached.

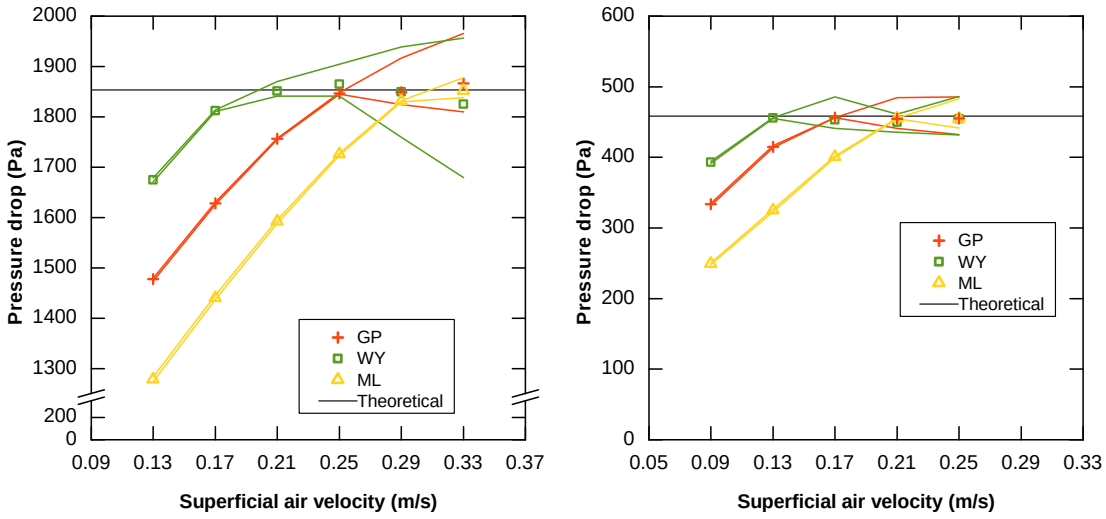

(a) Bentonite (E).

(b) Wheat bran (U)

Figure A.2: Simulated pressure drop versus velocity curves. (GP: Gidaspow's model, WY: Wen and Yu's model, ML: Mazzei and Lettieri's model). The solid lines represent the maximum and minumum values reached.

Acknowledgements

Agradecimientos

Durante los años de doctorado, he compartido momentos, recibido ayuda y aprendido en distintos aspectos de mucha gente, y no querría dejar fuera de estos agradecimientos a ninguno. Tampoco me decido en qué lengua agradecer, si hacerlo en español, mi lengua madre, en italiano, mi segunda lengua, o en inglés, el cual uso como útil instrumento para comunicarme con aquellos no hablan ninguna de ellas.

En primer lugar querría agradecer a mis directores de doctorado, Antonello Barresi y Daniele Marchisio, por sus consejos, ayuda profesional, enseñanzas, y correcciones a los distintos textos escritos durante estos años. También querría extender mi gratificación al Politecnico di Torino (Italia) y la Universidad Nacional del Sur (Argentina), por haberme dado la maravillosa oportunidad de hacer el doctorado en Italia, y a quienes han participado en la gestión y organización del Proyecto EUROTANGO (en especial a Silvia Carosso, del Departamento de Asuntos Internacionales del POLITO, por su gran predisposición y celeridad para resolver las distintas situaciones que se han presentado; a Laura Benedetti, SSRI UNS, y a María Begoña Lluzar Julian, Coordinadora del EUROTANGO UPV, por su permanente soporte).

Agradezco también a Giorgio Rovero y Massimo Curti por su ayuda y consejos técnicos en el Laboratorio de Fluidodinámica, a Luca Marmo por facilitarme el uso del equipo de tamizado, a Davide Fissore por su paciencia y explicaciones, a Antonio Buffo por su ayuda en CFD y programación, y a todos aquellos que de algún modo han aportado su granito de arena en enseñarme a usar algún equipo, facilitarme instalaciones de un laboratorio, o darme algún consejo para mi trabajo.

También me encuentro inmensamente agradecido con quienes tanto desde la distancia como en Torino, han aportado lo suyo desde el punto de vista humano. En primer lugar, mis padres, familia, amigos, y Vanesa (a quien nuevamente la Vida puso en mi camino justo en uno de los momentos más complicados de mi estadía en Italia), quienes han estado siempre presentes para motivarme, darme ánimos, aconsejarme, y escucharme. No puedo dejar de mencionar a toda esas maravillosas personas, argentinos, italianos, y de otras nacionalidades, que he conocido durante mi

estadía, con quienes he compartido salidas, el departamento, el laboratorio, viajes, largas charlas, "gite in montagna", y bagna caudas. Todas esas personas de quienes he aprendido mucho a nivel humano, y que han embellecido mis días transcurridos en tierras europeas, haciendo que mi vivencia sea mucho más que únicamente un doctorado.

Ringraziamenti

Durante gli anni di dottorato, ho condiviso dei momenti, ho ricevuto aiuto, e ho imparato in diversi aspetti da molta gente, e vorrei ringraziare tutti senza dimenticarmi di nessuno. Sono anche indeciso sulla lingua da usare per farlo: in spagnolo, la mia lingua madre; in italiano, la mia seconda lingua, oppure in inglese, lingua che uso come utile strumento per comunicarmi con coloro che non parlano né spagnolo né italiano.

Prima di tutto, vorrei ringraziare i miei relatori di dottorato, Antonello Barresi e Daniele Marchisio, per i loro consigli, aiuto professionale, insegnamenti, e correzioni dei diversi testi che ho scritto durante questi anni. Inoltre, vorrei estendere la mia gratitudine al Politecnico di Torino (Italia) e all'Universidad Nacional del Sur (Argentina), per darmi la meravigliosa opportunità di fare il dottorato in Italia, ed a tutti quelli che hanno partecipato alla gestione ed organizzazione del Progetto EUROTANGO (soprattutto a Silvia Carosso, del Dipartimento per gli Affari Internazionale del POLITO, per la sua grande disponibilità ed efficacia a risolvere le varie situazioni che sono emerse; Laura Benedetti, SSRI UNS, e María Begoña Lluzar Julian, Coordinatore EUROTANGO UPV, per il loro continuo supporto).

Ringrazio anche Giorgio Rovero e Massimo Curti per il loro aiuto e consigli tecnici nel Laboratorio di Fluidodinamica, a Luca Marmo per avermi lasciato usare il set di setacci, a Davide Fissore per la sua pazienza e spiegazioni, ad Antonio Buffo per il suo aiuto in CFD e programmazione, e a tutti coloro che in qualche modo mi hanno aiutato insegnandomi come utilizzare delle apparecchiature, lasciandomi usare un laboratorio, o dandomi dei consigli per il mio lavoro.

Inoltre, sono immensamente riconoscente con coloro che tanto dalla distanza come a Torino, sono stati presenti dal punto di vista umano. In primo posto, i miei genitori, la mia famiglia, i miei amici, e Vanesa (che è rientrata nella mia vita nei momenti più difficili del mio soggiorno in Italia); tutti loro, che sono stati sempre presenti per motivarmi, incoraggiarmi, consigliarmi, e ascoltarmi. Non posso lasciar fuori tutte quelle meravigliose persone, argentini, italiani, e di altre nazionalità, che ho conosciuto durante il mio soggiorno lì, con i quali ho condiviso uscite, l'appartamento, il laboratorio, viaggi, lunghe conversazioni, gite in montagna, e Bagna Caöda. Tutte quelle persone che non solo hanno fatto belli i miei giorni vissuti in terre europee, facendo della mia vita in italia molto di più che un dottorato,

ma anche mi hanno insegnato molto a livello umano.

Acknowledgements

During the elapsed years of my PhD, I shared moments, received help, and learned a lot of things from so many people that I would not like leave out of these acknowledgements. What is more, I am not sure about the language for writing these words; it can be either in Spanish, my mother tongue, or Italian, my second tongue, or even English, which I utilize as useful tool for communicating with people who do not speak neither Spanish nor Italian.

In first place, I would like to thank to my PhD advisers, Antonello Barresi and Daniele Marchisio, for their advices, professional help, teachings, and corrections to the different texts I wrote during these years. I would also like to extend my grateful to the Politecnico di Torino (Italia) and the Universidad Nacional del Sur (Argentina) for the wonderful opportunity of doing my PhD in Italy, and to all the staff of the EUROTANGO Project (especially to Silvia Carosso, from the Department of International Affairs at POLITO, for her great helpfulness and effectiveness for solving the different situations that have arisen; to Laura Benedetti, SSRI UNS, and María Begoña Lluzar Julian, EUROTANGO Coordinator UPV, for their permanent support).

I also want to thank to Giorgio Rovero and Massimo Curi for their technical support and advices in the Laboratory of Fluid-dynamics, to Luca Marmo for allowing me to use the sieving equipment, to Davide Fissore for his patience and explanations, to Antonio Buffo for his help in CFD and programming, and to every people who helped me in some way, allowing me the use of a laboratory, teaching me how to use an equipment, or giving me a suggestion for my work.

I am greatly thanked to those people, who from the distance or from Torino, have been present from the human point of view. In first place, mi parents, family, friends, and Vanesa (who came again into my life just during one of the most complicated periods of my life in Italy), all of them, who have been present for motivating, encouraging, suggesting, and hearing me. I can not forget to mention to all those wonderful people, Argentinians, Italians, and form other nationalities, who I met during my life in Italy, and I shared travels, the apartment, the laboratory, long conversations, "gite in montagna", and bagna caudas. All these people that not only have beautified my days in Europe, becoming them much more than a doctorate, but also taught me many things from the human point of view.